



Technische Universität München

Fakultät für Elektrotechnik und Informationstechnik

Lehrstuhl für Biologische Bildgebung

Multi-scale thermoacoustic imaging methods of biological tissues

Murad Ahmad Omar

Vollständiger Abdruck der von der Fakultät für Elektrotechnik und Informationstechnik der Technischen Universität München zur Erlangung des akademischen Grades eines

Doktor-Ingenieurs

genehmigten Dissertation.

Vorsitzender: Univ.-Prof. Dr. Gerhard Kramer

Prüfer der Dissertation:

1. Univ.-Prof. Dr. Vasilis Ntziachristos
2. Univ.-Prof. Dr. Jörg Conradt
3. Univ.-Prof. Dr. Thomas Misgeld

Die Dissertation wurde am 19.11.2014 bei der Technischen Universität München eingereicht und durch die Fakultät für Elektrotechnik und Informationstechnik am 24.08.2015 angenommen.

Contents

Acknowledgements	xiii
Abstract	xvii
1 Introduction	1
1.1 Biomedical imaging	1
1.2 Thermoacoustic imaging	3
1.3 Goals and objectives	5
1.4 Structure of dissertation and outline	5
2 Signal generation and image reconstruction	7
2.1 Governing equations	7
2.2 Sources of thermoacoustic signals	10
2.2.1 Thermoacoustic waves generated from RF energy	10
2.2.2 Thermoacoustic waves generated from laser radiation	12
2.3 Propagation of ultrasonic waves	14
2.4 Image reconstruction	16
2.4.1 Tomographic case	17
2.4.2 Raster scanning	18
2.4.3 Resolution, and scanning steps	20
2.4.4 Static vs. moving illumination	25
2.5 Multifrequency reconstruction	27
2.6 Filtering in raster-scan optoacoustic mesoscopy	32

2.6.1	Temporal filtering	33
2.6.2	Spatial filtering	33
2.7	Discussion	35
3	Technology	37
3.1	Ultrasonic detectors	37
3.1.1	Methods for the detection of ultrasound	38
3.1.2	Low frequency detectors	40
3.1.3	High frequency detectors	41
3.2	Lasers	42
3.3	Motorized stages	43
3.4	Data acquisition	44
3.5	Parallel processing	46
3.6	Outlook and conclusions	47
4	Near-field Radio-frequency Thermoacoustics (NRT)	49
4.1	Earlier work	49
4.2	System description	50
4.2.1	Equipment and characteristics	50
4.2.2	RF interference and system isolation	51
4.3	Impulse generator	52
4.3.1	Basics of impulse generation	52
4.3.2	Capacitive impulse generators	53
4.3.3	Pulse forming lines (PFL)	54
4.3.4	Other methods	56
4.3.5	Improving the switching times	57
4.4	Results and imaging	57
4.4.1	Choice of imaging parameters	57
4.4.2	Imaging of phantoms	59
4.4.3	<i>Ex-vivo</i> imaging of small animals	60

4.5	Other modes of RF excitation	61
4.6	Discussion and outlook	63
5	Raster-scan Optoacoustic Mesoscopy	65
5.1	Introduction	65
5.2	Design of a high-resolution system	67
5.2.1	Ultrasonic detection	67
5.2.2	Laser source	67
5.2.3	Data acquisition	68
5.2.4	Scanning	68
5.2.5	Synchronization and control of the system	68
5.3	System characterization and calibration	70
5.3.1	Bandwidth characterization	70
5.3.2	Resolution and penetration depth characterization	71
5.3.3	Calibration of the system	73
5.4	Reflection-mode RSOM	74
5.4.1	System design	74
5.4.2	Performance comparison of 100 MHz and 50 MHz systems	75
5.5	Tomographic RSOM	78
5.5.1	What are the limitations of RSOM?	78
5.5.2	Design of a tomographic RSOM	79
5.5.3	MO-RSOM calibration and reconstruction	80
5.5.4	Characterization of MO-RSOM	81
5.5.5	Examples of MO-RSOM imaging	83
5.6	Combination with optical microscopy techniques	84
5.6.1	Non-linear optical microscopy techniques	84
5.6.2	Optoacoustic microscopy	86
5.6.3	Hybrid multiphoton optoacoustic microscopy	87
5.6.4	Combination with RSOM	89
5.7	Discussion and outlook	90

6 Applications of raster-scan optoacoustic mesoscopy	93
6.1 Imaging of model organisms	93
6.1.1 Handling of samples	94
6.1.2 Imaging of <i>drosophila melanogaster</i>	95
6.1.3 Imaging of zebrafish	97
6.1.4 Imaging of <i>Xenopus</i>	100
6.2 Imaging of the vascular network in a mouse ear	101
6.3 Imaging of Cells	103
6.3.1 Imaging of melanin cells	103
6.4 Imaging of tumor development and growth	104
6.5 Imaging of skin	107
6.6 Summary, and discussion	109
7 Future and outlook	111
A List of publications	115

List of Figures

1.1	Imaging pyramid, showing the competing quantities while imaging.	2
1.2	Example of the diffusion of light: (a) the medium is slightly diffusing, to show the light penetrating it, (b,c) diffusion increases, (d) totally diffusive medium, light completely loses its directivity after the first millimeter.	3
2.1	Comparison of the losses inside muscles, which happen due to electric conductivity, and relaxation of electric dipoles, the parameters are taken from Gabriel et al.: [1]	11
2.2	Extinction coefficient of different biological material.	13
2.3	A graphical representation of Snell's law.	15
2.4	Different measurement geometries: (a) A single detector is scanned around the object, (b) an array of detectors is surrounding the object, (c) a single element detector is scanned above the object.	17
2.5	(a) Definition of the geometry used, (b) an example from a real detector, showing the angular acceptance of the detector.	20
2.6	Example of aliasing when choosing the wrong z-discretization. (a) Discretization is $2.5 \mu m$, (b) discretization is $5 \mu m$, and (c) discretization is $10 \mu m$	24
2.7	Comparison of a two illumination schemes, once with the radius of illumination smaller than R_{BF} (a), and once the radius of illumination is larger than R_{BF} (b).	26
2.8	Thermoacoustic signal generated from a small sphere with different radii, (a) time domain signals, and (b) their frequency contents.	27

2.9	Representation of the wavelet decomposition of the detection bandwidth, into detail coefficients (DC), and approximation coefficients (AC), this procedure could be repeated again on the AC coefficients.	30
2.10	(a) Full detection bandwidth, (b) division into sub-bands with equal bandwidths, (c) division into sub-bands with equal relative bandwidths, and (d) division into sub-bands where every sub-band has double the bandwidth of the previous one.	31
2.11	A comparison of the reconstruction achieved when: (a) reconstructing all the frequencies together, (b) performing multifrequency reconstruction. Adapted from Omar et al. [2].	32
2.12	(a) Bouncing of the thermoacoustic signal between the active element, and the interface of glass and water, (b) appearance of the reflections on the b-scans.	34
2.13	(a) MIP xy before filtering, (b) MIP xy after filtering, (c) MIP xz before filtering, (d) MIP xz after filtering.	35
3.1	Different kinds of detectors: (a) unfocused detector, (b) spherically shaped detector for focusing, (c) focused detector using an acoustic lens.	38
3.2	Optoacoustic signal generated from a 10 μm sphere: (a) time signals, (b) Fourier transform of the time signals.	42
3.3	Trigger options: (a) single mode, where after every trigger event the data is transferred to the PC, (b) multi-record mode, the data acquisition system acquires a certain number of trigger events, then transfers them all together to the PC.	45
4.1	(a) Energy is steadily stored into an energy storing element, (b) the release of the energy happens very fast, (c) schematic of the pulse generation. . . .	52
4.2	Schematic of the capacitive impulse generation circuit.	53
4.3	Comparison between the length of the transmission line and the width of the pulse.	55

4.4	Schematic of the pulse forming line circuit, showing the charging circuit and the coupling circuit.	56
4.5	Schematic of the setup, both the excitation and the acquisition are shown.	58
4.6	Comparison of the signals generated from saline tubes (blue circles), and tubes filled with de-ionized water (violet circles).	59
4.7	Tomographic thermoacoustic images of a mouse from the thorax region: (a&b) thermoacoustic images, (c&d) corresponding cryoslices; (M) muscles, (S) spinal cord, (L) lungs, (H) heart, (Li) limbs.	60
4.8	Schematic, and comparison between the signals generated using the pulsed mode and the quasi CW mode of excitations.	62
5.1	(a) Normal operation and synchronization, (b) synchronization based on pulses from the stage.	69
5.2	Comparison in the form of the old detector (a), and the new detector (b).	75
5.3	Comparison of the performance of RSOM50 and RSOM100. (a) angular coverage of RSOM50 vs. RSOM100, (b) FWHM of a 10 μm sphere imaged with RSOM50, (c) FWHM of a 3 μm sphere imaged with RSOM100.	77
5.4	Schematic of Multi-Orientation RSOM	80
5.5	An example of combining the different views in MOR SOM, different measurements taken at different angles, with steps of 20° are combined into a single image, with improved resolution and <i>SNR</i>	81
5.6	A figure showing the measurement, as well as the measured angular coverage of the 50 MHz detector.	82
5.7	Profiles through a 10 μm sphere measured with MOR SOM.	82
5.8	A fish measured with MOR SOM, as well as a comparison of the cross sections, generated using RSOM (a, b), versus MOR SOM (c, d).	83
5.9	Schematic of the multiphoton, optoacoustic microscopy system (MPOM).	88
5.10	An example of a fish measured with MPOM. (a) An overlay of SHG and optoacoustic microscopy, (b) bright field image. The image of the fish is a courtesy of Google.	89

5.11 (a) Fish imaged in RSOM, (b) zoom in using optoacoustic microscopy, (c) bright field microscopy, (d) second harmonic generation showing the muscle fibers, (e) third harmonic generation microscopy showing the spaces between the muscles, (f) combination of (b), (d), and (e). Scale-bar (a) 0.5 mm, (b)-(f)100 μm	90
6.1 Optoacoustic image of a genetically modified fly, the inset shows a photo of the fly(a), and pupae (b, c), photographic image of the pupae. The scale bars are 500 μm	96
6.2 Optoacoustic image of a zebrafish (a), zoom-in on the front part of part a (b), same region reconstructed using only the frequencies 20-100 MHz (c), 100-180 MHz (d), an overlay of parts b and d (e). The scale bars are 500 μm in (a), and 250 μm in the rest.	98
6.3 Optoacoustic image of a <i>Xenopus</i> : control (a), with 2.5% AF546 injected. . .	101
6.4 Optoacoustic image of an excised mouse ear: (a) all frequencies, (b) low frequencies, (c) high frequencies, (d) overlay of a and c. Scale bar: 500 μm	102
6.5 Sample with melanin expressing cells (a), control (b).	104
6.6 Optoacoustic images of tumor growth using RSOM50: The top images show a followup of the tumors growth through days 2, 4, 7, and 9. In these images a MIP from a certain depth. Additionally, the lower row shows a zoom in on the same region, near the tumor, showing an increase in the number of micro-vessels as the tumor grows in size. Green represents the high frequencies, and the red represents the low frequencies. Scalebar: 1 mm for the upper 4 images, and 500 μm for the lowest row.	105
6.7 Comparison of a tumor image using (a) RSOM100, and (b) RSOM50. Cyan hot represents the high frequencies, and orange hot represents the low frequencies. Scalebar: 1 mm	107

- 6.8 Different layers of human skin. a) Cross section through human skin. (b-e) show maximum amplitude projections along the depth direction within the regions marked in (a). b) epidermis (0-150 μm), c) dermal papillae (150-300 μm), d) sub-papillary plexus (300-555 μm), e) deep vessels of the sub-papillary plexus or the intermediate venous plexus of the dermis (555-975 μm). In (b-e) a zoom in into the region marked by the white dashed box is shown. The FWHM of the line-like or point-like structures marked by the white arrows in each sub-figure were calculated to be: 27.5 μm (b), 35 μm (c), 55 μm (d), and 87.5 μm (e). In (d,e) the original image (white) is with an image filtered for vessels in green. The SNR of the vessel marked by the red arrow with respect to the background marked by the red box in (e) in the unfiltered image is 12 dB. The scale bars are a) 500 μm , b,c) 1 mm, and 100 μm in the insets, d,e) 1 mm, and 250 μm in the insets 108

List of Tables

3.1 Lasers used for imaging in RSOM	43
3.2 Comparison between the different data acquisition systems used throughout the dissertation.	44
5.1 Comparison between the characteristics of the 100 MHz detector, and the 50 MHz detector.	76

Acknowledgements

I would like to thank Prof. Dr. Vasilis Ntziachristos, my Ph.D. advisor for giving me the opportunity to work in this new, and exciting field. From him I learned not only the excitement of working on problems that matter, but also how to apply my previous knowledge into practical problems. I learned from him, that working in the field of biomedical engineering is more about solving problems than it is in any other field. I would like to thank him as well for his supervision, and for the discussions that we had. His door was always open for me. From him I learned not only science, but also leadership skills, and self-dependence.

I would like also to thank Prof. Dr. George Sergiadis, who helped me a lot in my first year, and in building my first setup, without him what took a year would have taken 2 years. He was always there for me, and he was always ready and eager to go with me to the lab, and help in solving any problems, or to share a moment of joy when things start working.

I would like also to thank Dr. Stephan Kellnberger who took care of me in my first months in the group, from whom I gathered my first knowledge in thermoacoustics, and with whom I shared many productive hours inside the lab, Stephan helped a lot, and was always eager to see new things working. Stephan was always there for me. Outside the lab we also had a good friendship.

At this moment I would like to thank Prof. Dr. Daniel Razansky, with whom I had many discussions, and who helped me get started at IBMI. Both scientifically, and administratively.

I would like to thank Dr. Jerome Gateau as well, Dr. Gateau helped me understand ultrasound propagation, ultrasound detectors, and imaging, he also helped me a lot in developing Raster-Scan Optoacoustic Mesoscopy. Again, what took a year could have taken two years without the help of Dr. Gateau. With him we had many discussions, and he is still

ready all the time to support me, and to help me when help is needed. With him we shared a good friendship.

Additionally, I would like to thank Dr. Amir Rosenthal, Dr. Amir helped me in understanding and grasping some difficult ideas and concepts in signal processing, as well as in ultrasound detection, and optoacoustics. From him I learned to always ask the right questions, with him we shared many late night experiments, two trips to Las Vegas, a road trip through the American west, as well as a good friendship.

I would like also to thank the contribution of Dominik Soliman, who helped me a lot with designing the second generation of RSOM, he also helped in improving the reconstruction code for RSOM. With Dominik I also shared many good moments, and a good friendship with him.

I would like also to thank Dr. George Tserevelakis, who helped me a lot in understanding optical non-linear microscopy, with him I shared not only nice moments in the lab, but also a good friendship outside of the lab.

Mathias Schwarz has helped a lot as well in developing RSOM for experiments with animals, as well as for experiments with humans. He also helped in developing the reconstruction code, and improving it.

I would like to thank Andrei Chekkoury, and Amy Lin, with whom we spent many hours in side the lab working on the first experiments for the hybrid SPIM-Optoacoustics measurements. With Andrei we also developed a good friendship.

I would like to thank Panagiotis Symvoulides for help with data visualization, and cryoslicing of the mice.

I would like also to thank my students, who helped a lot, and who managed to do beautiful work in very short periods of time, Juan Osorio, for the help in the design of the amplifier bank, and building it. Johannes Rebling, for the help in designing and building the Tomographic RSOM, or Multi-orientation RSOM (MORSOM). And Demosthenes Koulikas for his work on designing better filters, and better filtering schemes, for multifrequency reconstruction.

I would like also to thank Dr. Xose Luis Dean Ben for his help and support, he always

encouraged me, and he always shared his thoughts and ideas with me. With him I shared a good friendship as well.

Other people I would like to thank are: Dr. Karin Radrich, and Dr. Angelique Ale, with whom I shared an office for more than a year. Daniel Quirous, with whom I share an office now, Dr. Nicolas Beziere who helps me when it comes to biology, and who has a nice cat. Dr. Vladimir Ermolayev, who helped in getting the thermoacoustic protocol running. Stratis Tzoumas with whom I had nice discussions, and nice poker nights, as well as a trip to Vegas. I would like also to thank Dr. Ara Ghazaryan, Dr. Miguel Caballero, Dr. Adrian Taruttis, and Dr. Andreas Oancea.

Additionally I would like to thank Dr. Frank Dietrich, my supervisor during my masters degree who advised me to apply to IBMI. I thank also PD Dr. Timo Mappes, who helped me with supervising Johannes Rebling, and who helped with the design of MORSOM as well. Additionally, I thank Dr. Tobias Schmitt-Manderbach for help with MORSOM as well, and for the fruitful discussions. From our collaborators I would like to thank Dr. Hernan Lopez-Schier, and Prof. Dr. Gil Westmeyer.

I would like also to thanks Susanne Stern, Silvia Weinzierl, Zsuzsanna Öszi, Dr. Christiane Ogorek, Dr. Julia Niefnecker, Dr. Karin Schaeffer, Dr. Andreas Brandstaetter, Dr. Doris Bengel, Dr. Andreas Murr, Dr. Christoph Hinzen, and Prof. Dr. Karl-Hans Englmeier for their support with all administrative issues. As well I would like to thank Sarah Glasl, Uwe Klemm, and Florian Jurgeleit with their help when it came to animal handling.

Last but not least I would like to thank my family, and friends for their continuous support, and their believe in me, among most I miss my father who supported me in my choice in continuing my education.

Abstract

English version

Since its introduction thermoacoustic imaging, both based on radio-frequency (RF) and optical excitations, has seen a tremendous growth in terms of technology, and applications, especially optical thermoacoustics, more commonly known as optoacoustics. Thermoacoustics is based on the use of ultrasound detection, to detect RF, or optical absorption in biological tissues. This way RF, or optical absorption could be generated deep inside the biological tissue. In the past decade the method was used to image small animals in vivo, and showed great potential for further applications, although the current systems deliver great performance, to answer the next generation of biological questions there is need for higher resolution, at depths beyond what optical microscopy techniques can offer. In this work we present research and methods for increased resolutions in thermoacoustic imaging, we present them at both the tomographic and at the mesoscopic scales, hence multi-scale imaging. First we show this improvement on the tomographic scale, where we use a new design of an RF-pulse generator to improve the resolution in RF-thermoacoustics, which we here call near-field radio-frequency thermoacoustics (NRT), using the developed method we were able to decouple the pulse width, necessary for higher resolutions, from the pulse energy, needed for higher signal to noise ratio. Besides the developed system we showcase the application of the new design on tissue mimicking phantoms, and biological samples ex vivo. Then we introduce raster scan optoacoustic mesoscopy (RSOM), which is based on optical excitation, using pulsed ns-lasers, during this work we investigated a new design based on high frequency spherically focused ultrasound detectors, in the fre-

quency range of 100 MHz, and tomographic out-of-focus reconstruction. We show both planar scanning geometries, either in trans-illumination mode, or in reflection mode, and tomographic mode which overcomes some of the major limitations of planar geometries, but limited to small samples. At the end we showcase some samples that were imaged using RSOM. This includes imaging of model organisms, such as the zebrafish, *Drosophila Melanogaster* pupae (fruit fly), or *Xenopus*. As well as imaging of cells, and tumor development in mice.

German version

Thermoakustische Bildgebung ist ein neues Verfahren, welches auf der Detektion von elektrischer und optischer Absorption in Gewebe mittels Ultraschall basiert. Obwohl die thermoakustische Bildgebung bereits vielseitige Anwendungen in biomedizinischen Bereich gefunden hat, sind zur Beantwortung künftiger biologischer Fragen vor allem eine Kombination von hoher Auflösung mit gleichzeitig hoher Eindringtiefe entscheidend. Im Rahmen dieser Dissertation haben wir verschiedene Methoden untersucht, um biologische Informationen tief im Gewebe mit hoher Auflösung darzustellen. Diese Arbeit umfasst hierbei ein neues Konzept zur ultrakurzen Anregung von Gewebe mit Radiofrequenz-Pulsen im Nanosekunden Bereich, welches hochauflösende Bilder von biologischem Gewebe erzeugt, sowie der Einsatz von Hochfrequenz Ultraschall Detektoren für die Optoakustische Mesoskopie. Zusätzlich haben wir in Rahmen dieser Arbeit neue tomographische Rekonstruktionsverfahren entwickelt, welche eine genaue Rekonstruktion von thermoakustischen Bildern ermöglicht. In dieser Dissertation beschreiben wir diese Verfahren, analysieren die Ergebnisse und zeigen anhand von Beispielen die Anwendung der thermoakustischen Bildgebung im biomedizinischen Bereich.

Chapter 1

Introduction

1.1 Biomedical imaging

Biomedical imaging is an important field of modern research; it is an essential tool for studying biology, to discover drugs, to diagnose patients, and to research and study different diseases such as cancer. It is correct to say that the advancement of biology and medicine is dependent on the advancement of the biomedical imaging technology.

Essentially any biomedical imaging system consists of a certain physical phenomena, such as the attenuation of X-rays. Data processing is performed on the raw data; this processing includes filtering and reconstruction. In such a way, raw signals are transformed into a useful image. Finally, image processing could be used to improve the quality of the image. In biomedical imaging, there is always a quest to optimize several competing parameters at the same time. Those parameters include spatial resolution, time resolution, penetration depth, and toxicity. Although the first three are self-explanatory, toxicity here, means the amount of energy that doesn't harm the sample. Generally speaking, optimizing for one quantity means sacrificing the other ones, if temporal resolution is important then one might need to sacrifice spatial resolution, and use higher energies, which are more harmful than lower ones. To schematically represent this please look at figure 1.1.

The electromagnetic spectrum offers a rich contrast for biomedical imaging, in the radio frequency (RF) and microwave region different tissue has different conductivities and different

permittivities. The optical region also has a rich contrast, where different kinds of tissues has different absorption, and different scattering properties. These make the electromagnetic spectrum very interesting, and useful for biomedical imaging. Unfortunately, pure RF or microwave imaging suffer from ill-posedness, and it achieves low resolution [3–5]. Optical imaging can achieve high resolution but only at low depths of penetration, or for thin samples [6–9]. Although optical methods are available which could be used to image deeper than microscopy, such as diffuse optical tomography [10], and fluorescence molecular tomography [11, 12]. Nonetheless these methods suffer from low resolution due to diffusion [13], see figure 1.2.

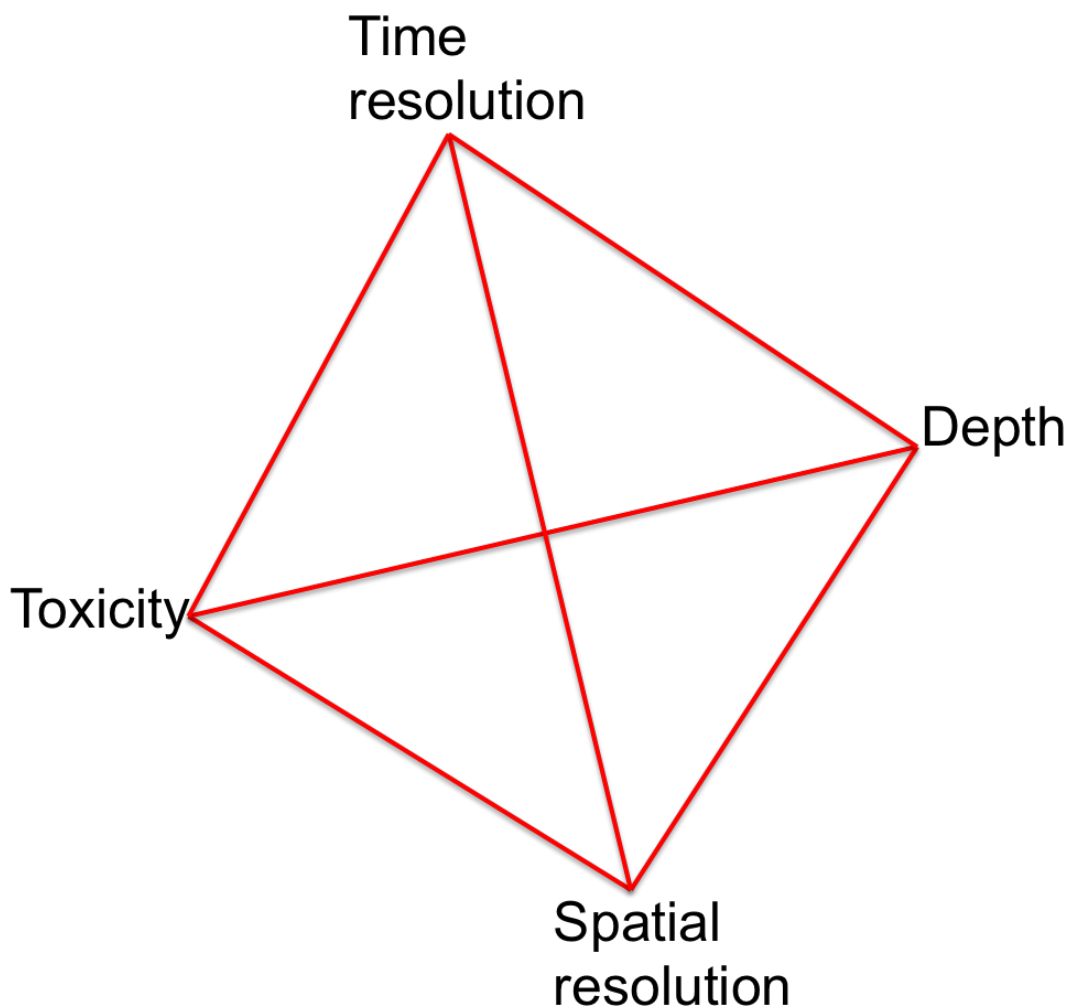


Figure 1.1: Imaging pyramid, showing the competing quantities while imaging.

A solution to these problems, which can enable high resolution imaging of the electromagnetic properties of biological tissue, has been gaining a lot of focus in the last two

decades. This solution is called the thermoacoustic effect, which passively measures the electromagnetic properties of the tissue using ultrasonic detection.

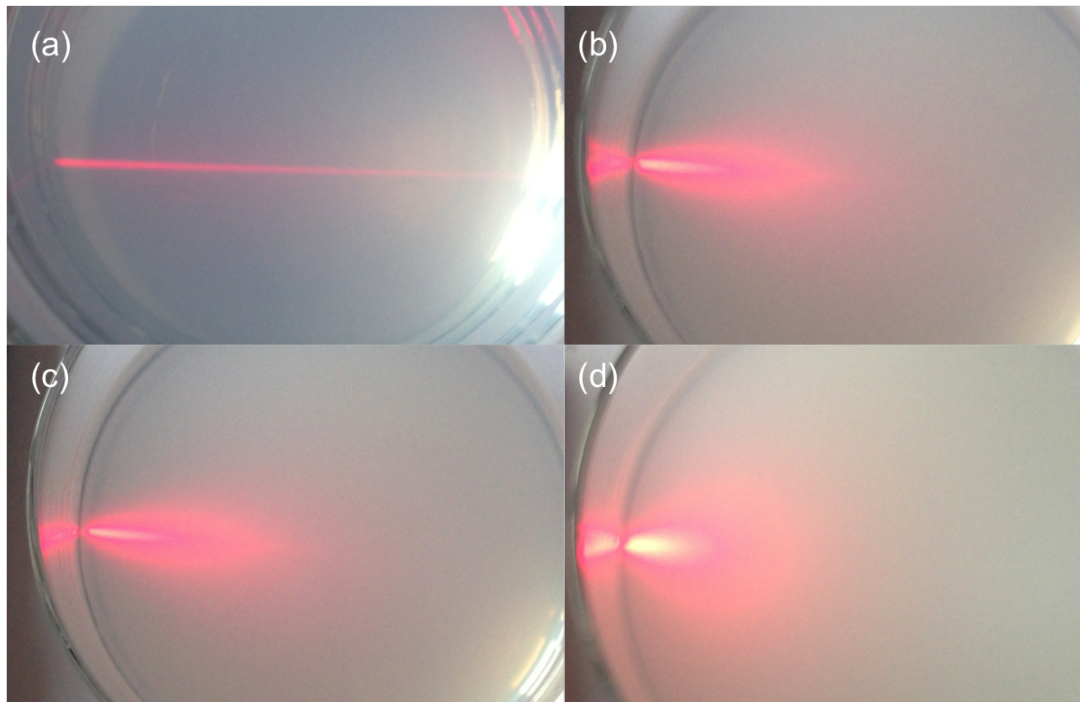


Figure 1.2: Example of the diffusion of light: (a) the medium is slightly diffusing, to show the light penetrating it, (b,c) diffusion increases, (d) totally diffusive medium, light completely loses its directivity after the first millimeter.

1.2 Thermoacoustic imaging

The thermoacoustic effect, more commonly known as the photoacoustic, or the optoacoustic effect, describes the generation of ultrasound waves in response to the rapid heating of a sample using a varying electromagnetic field. As the molecules absorb the electromagnetic energy, they undergo a thermoelastic expansion, which results in the generation of ultrasonic waves. This thermoacoustic effect is common between all parts of the electromagnetic spectrum and could be observed when exciting the sample with any source of electromagnetic radiation.

Although Alexander Graham Bell discovered the thermoacoustic effect in 1883, it was only until 1981 that its use for biomedical applications was proposed. In that year, Theodore Bowen suggested the use of high energy pulses of microwave radiation to image bones [14]. Though this proposal was the first hint at using the thermoacoustic effect for imag-

ing of biological samples, the first systems for imaging were only built later in the 1990's. Those systems were used to generate the first thermoacoustic images, where Alexander Oraevsky, Robert Kruger, and Lihong V. Wang [15–17].

The attraction of thermoacoustic imaging comes from decoupling of the mechanisms of resolution, and contrast, where in most systems resolution and contrast are defined by the same waves. In thermoacoustic imaging, resolution is usually stated by ultrasonic detection, while contrast comes from the excitation source. This way optical contrast, for example, could be measured deep inside the tissue, at depths beyond the transport mean free path, with a satisfying resolution of tens of microns. Or radio waves and microwaves could be used as the excitation source, and images with a resolution much finer than the excitation wavelength could be achieved inside biological tissue. This way we can overcome the limitations of pure microwave imaging, the limitations of pure optical imaging, and the limitations of ultrasonic imaging. Where in the case of excitation with radio-frequency waves resolutions as high as $45\ \mu\text{m}$ are achieved [18]. In the case of thermoacoustic imaging with optical excitation, using laser pulses, the use of ultrasound detection allows deeper imaging of biological tissues than what optical microscopy can offer. Resolutions as fine as $18\ \mu\text{m}$ have been achieved at depths of several millimeters during this dissertation [2].

Due to advancement in ultrasonic detection, in the acquisition electronics, as well as in the generation of high energy ns-laser pulses the field of optical thermoacoustic imaging has seen a tremendous growth in the last decade. This growth is seen in the number of yearly publications, several new contrast agents are being developed in the labs, and its role in many applications is growing at a rapid pace; these applications include tumor imaging, imaging of inflammation, imaging of cardiovascular diseases, imaging of model organisms, and many more. Additionally the use of tunable lasers allows for multispectral imaging, increases the sensitivity for specific targets, and enables functional and molecular imaging.

1.3 Goals and objectives

The goals of this dissertation are to push the boundaries of thermoacoustic imaging, both RF thermoacoustics, and laser thermoacoustics. Such new capabilities would help in drug discoveries, in early diagnosis of diseases, in studying the development of model organisms, and understand the development of certain diseases like cancer. Those new capabilities would enable high resolution imaging of RF absorption within biological tissue. As for laser thermoacoustics, those new capabilities will bridge the gap between optical microscopy techniques, and tomographic techniques, which we call the mesoscopy gap. This gap is essentially the region where microscopic techniques cannot penetrate beyond, and the tomographic techniques don't have the resolution to image mesoscopic structures efficiently.

1.4 Structure of dissertation and outline

In chapter 2 we will discuss how thermoacoustic signals are generated. Where does the contrast in thermoacoustic imaging comes from. What makes thermoacoustic imaging so attractive. What affects the frequency content of the generated signals. How it is possible to generate an image from raw signals. What defines the resolution in thermoacoustic images and multi-bandwidth reconstruction, where the detection bandwidth is divided into several sub-bands.

In chapter 3 we will discuss which technologies enable thermoacoustic imaging, from ultrasonic detection to excitation, to acquisition, and finally processing of the signal. These capabilities are important, since without such technologies thermoacoustics would not have reached its current status within the biomedical imaging community.

In chapter 4, we will discuss the generation of RF thermoacoustic signals. We will start with a discussion about the previous work. What was done until now. What are the limitations of the current systems, and subsequently we will introduce our method, show how it improves the resolution compared to previous methods, and showcase some results. At the end of the chapter, we will discuss some directions for future work and the current problems.

In chapter 5 we will be discussing high resolution optical thermoacoustic imaging, more commonly known as optoacoustics or photoacoustics. We call the system which we developed raster-scan optoacoustic mesoscopy (RSOM). We developed this system with the help of a high frequency, spherically focused ultrasound detectors, raster scanning the sample, and out of focus reconstruction. The chapter starts with an introduction of the method, both variations of the method, trans-illumination, and epi-illumination. Subsequently we will discuss the system characteristics, as well as some ongoing work to improve the resolution, and the detection capabilities of the system. The chapter concludes with a discussion of the combination of the system with optical microscopy techniques, such as multiphoton microscopy, optoacoustic microscopy, and selective plane illumination microscopy .

We will discuss the applications of RSOM in chapter 6. As mesoscopy refers to the gap between what microscopy can efficiently image, and where tomography becomes relevant, such applications include imaging of model organisms, imaging of tumor development, and imaging of skin diseases. The chapter concludes with a discussion of these applications and a future outlook, as well as what needs to be done to make RSOM infiltrate the clinics, and other research institutions.

We conclude this dissertation with a short discussion, and a short outlook in chapter 7.

Chapter 2

Signal generation and image reconstruction

As mentioned in chapter 1, thermoacoustics is the generations of ultrasonic waves, which follows absorption of electromagnetic energy by the sample. As we will see in this chapter, the generated thermoacoustics signals are dependent on the rate of change of the absorbed energy. Because of this dependence a DC source cannot generate any thermoacoustic waves, on the other hand, a short pulse, or a sine wave will generate one. The first case is sometimes called time-domain thermoacoustics [19–21], while the second one is called frequency-domain thermoacoustics [22–24]. As all the methods discussed in this dissertation are time-domain methods, frequency-domain thermoacoustics will not be mentioned anymore.

2.1 Governing equations

The basic two equations that govern the thermoacoustic wave generation and propagation are: the thermal expansion equation (the generalized Hooke's law equation), and the linear inviscid force equation (the equation of motion) [20,21,25]. The thermal expansion equation could be written as:

$$\nabla \cdot \boldsymbol{\xi}(\mathbf{r}, t) = -\kappa p(\mathbf{r}, t) + \beta T(\mathbf{r}, t), \quad (2.1)$$

and the linear inviscid force equation could be written as:

$$\rho \frac{\partial^2}{\partial t^2} \boldsymbol{\xi}(\mathbf{r}, t) = -\nabla p(\mathbf{r}, t), \quad (2.2)$$

where $\boldsymbol{\xi}(\mathbf{r}, t)$ denotes the medium displacement at location \mathbf{r} , and time t , $p(\mathbf{r}, t)$ is the pressure, $T(\mathbf{r}, t)$ is the temperature, κ is the isothermal compressibility, ρ is the medium density, and β is the thermal coefficient of volume expansion.

Taking the divergence of (2.2):

$$\rho \frac{\partial^2}{\partial t^2} (\nabla \cdot \boldsymbol{\xi}(\mathbf{r}, t)) = -\nabla^2 p(\mathbf{r}, t), \quad (2.3)$$

and substituting (2.1) into (2.3) we get the thermoacoustic wave equation:

$$\left(\nabla^2 - \frac{1}{v_s^2} \frac{\partial^2}{\partial t^2} \right) p(\mathbf{r}, t) = -\frac{\beta}{\kappa v_s^2} \frac{\partial^2 T(\mathbf{r}, t)}{\partial t^2}, \quad (2.4)$$

where $v_s = 1/\sqrt{\rho\kappa}$ is the speed of sound. To solve (2.4) we use Green's function [26], this is done by replacing the right hand side of (2.4) with a delta function in space and time $\delta(\mathbf{r} - \mathbf{r}', t - t')$, where the primed coordinates represent the coordinates of the source, and the unprimed coordinates represent the coordinates of the observation point. In the space where no boundaries exist the solution takes the following form:

$$G(\mathbf{r}, t; \mathbf{r}', t') = \frac{\delta(\mathbf{r} - \mathbf{r}', t - t')}{4\pi|\mathbf{r} - \mathbf{r}'|}. \quad (2.5)$$

From system's engineering point's of view, the Green's function in (2.5) could be interpreted as the impulse response of the thermoacoustic system. This impulse response is due to a point acoustic source at position \mathbf{r}' , and to a ramp temperature rise starting at time t' . From the properties of Green's function, the pressure $p(\mathbf{r}, t)$ is simply the convolution of the Green's function with the right hand side of (2.4), and could be written in the following

form [25–27]:

$$p(\mathbf{r}, t) = \frac{\beta}{\kappa v_s^2} \int_{\mathbf{r}'} \int_{t'} G(\mathbf{r}, t; \mathbf{r}', t') \frac{\partial^2 T(\mathbf{r}', t')}{\partial t'^2} dt' d\mathbf{r}', \quad (2.6)$$

substituting (2.5) into (2.6) we get:

$$p(\mathbf{r}, t) = \frac{\beta}{4\pi\kappa v_s^2} \int_{\mathbf{r}'} \int_{t'} \frac{\delta(\mathbf{r} - \mathbf{r}', t - t')}{|\mathbf{r} - \mathbf{r}'|} \frac{\partial^2 T(\mathbf{r}', t')}{\partial t'^2} dt' d\mathbf{r}'. \quad (2.7)$$

This result is a very important, it allows us to simulate the pressure generated due to a change in temperature. Whether it is due to a fast pulse of energy or due to slow changes in temperature. Finally, we need to link the generated pressure with the thermoacoustic source $H(\mathbf{r}, t)$, which is called the heating function. The heating function could be any kind of source that produces a rise in temperature upon interaction with the sample; it could be RF energy, optical energy, or any other kind of EM energy. To express the temperature in terms of the heating function $H(\mathbf{r}, t)$ we use the heat equation [28]:

$$\frac{\partial T(\mathbf{r}, t)}{\partial t} - \alpha \nabla^2 T(\mathbf{r}, t) = \frac{1}{\rho C_V} H(\mathbf{r}, t), \quad (2.8)$$

where: α is the thermal diffusivity, and C_V is the heat capacity of the medium. For a fast pulsed source in an aqueous medium, or soft tissue (2.8) could be further simplified; for such a medium the thermal diffusivity is on the order of 10^{-7} . Thus, for a fast pulse of energy, the spatial variation of T is much smaller than the temporal variation:

$$\alpha \nabla^2 T(\mathbf{r}, t) \ll \frac{\partial T(\mathbf{r}, t)}{\partial t}, \quad (2.9)$$

this condition is called the thermal confinement condition, and could be represented mathematically as:

$$\tau_{pulse} \leq \frac{d^2}{\alpha}, \quad (2.10)$$

where d is the diameter of the sample. Another important condition is the stress confinement condition, which defines the time required for the acoustic wave to propagate a certain

distance, and it could be represented mathematically as:

$$\tau_{pulse} \leq \frac{d}{v_s}, \quad (2.11)$$

if both the temperature confinement, and the stress confinement conditions are satisfied, then the excitation is assumed to be delta pulse like: $\delta(t)$. Thus, (2.8) could be simplified to:

$$\frac{\partial T(\mathbf{r}, t)}{\partial t} = \frac{1}{\rho C_V} H(\mathbf{r}, t), \quad (2.12)$$

substituting (2.12) into (2.7) we get the following expression for the pressure:

$$p(\mathbf{r}, t) = \frac{\beta}{4\pi C_V} \int_{\mathbf{r}'} \int_{t'} \frac{\delta(\mathbf{r} - \mathbf{r}', t - t')}{|\mathbf{r} - \mathbf{r}'|} \frac{\partial H(\mathbf{r}', t')}{\partial t'} dt' d\mathbf{r}'. \quad (2.13)$$

2.2 Sources of thermoacoustic signals

2.2.1 Thermoacoustic waves generated from RF energy

Radio-frequency (RF) waves, deposit energy into the tissue using three basic mechanisms; electric conductivity, electric dipole relaxation, and magnetic dipole relaxation. These could be summarized mathematically using Poynting's theorem:

$$P_{loss} = \sigma(\mathbf{r}) |\mathbf{E}(\mathbf{r}, t)|^2 + \frac{\epsilon''(\mathbf{r})}{2} |\mathbf{E}(\mathbf{r}, t)|^2 + \frac{\mu''(\mathbf{r})}{2} |\mathbf{H}(\mathbf{r}, t)|^2, \quad (2.14)$$

where, P_{loss} is the energy loss or energy deposition per unit volume, \mathbf{E} is the electric field strength, \mathbf{H} is the magnetic field strength, σ is the electric conductivity, ϵ'' is the imaginary part of the electric permittivity, and μ'' is the imaginary part of the magnetic permeability. These quantities are the sources of radio-frequency, and microwave losses found in normal matter. As normal tissue don't exhibit magnetic losses, (2.14) becomes:

$$P_{loss} = \sigma(\mathbf{r}) |\mathbf{E}(\mathbf{r}, t)|^2 + \frac{\epsilon''(\mathbf{r})}{2} |\mathbf{E}(\mathbf{r}, t)|^2, \quad (2.15)$$

additionally, considering the Debye equation:

$$\epsilon(\omega) = \epsilon_{\infty} + \frac{\Delta\epsilon}{1 + j\omega\tau}, \quad (2.16)$$

where, ϵ_{∞} is the permittivity at the high frequency, $\Delta\epsilon = \epsilon_s - \epsilon_{\infty}$, ϵ_s is the static permittivity, ω is the radial frequency, and τ is the characteristic relaxation time. In (2.15) ϵ'' is the imaginary part of (2.16):

$$\epsilon = \epsilon' - j\epsilon''. \quad (2.17)$$

For most biological tissues, such as muscles and fat, and for frequencies below 100 MHz, the conductivity losses are much higher than electric relaxation losses [1,29,30], thus (2.15) could be simplified to:

$$P_{loss} = \sigma(\mathbf{r})|\mathbf{E}(\mathbf{r}, t)|^2. \quad (2.18)$$

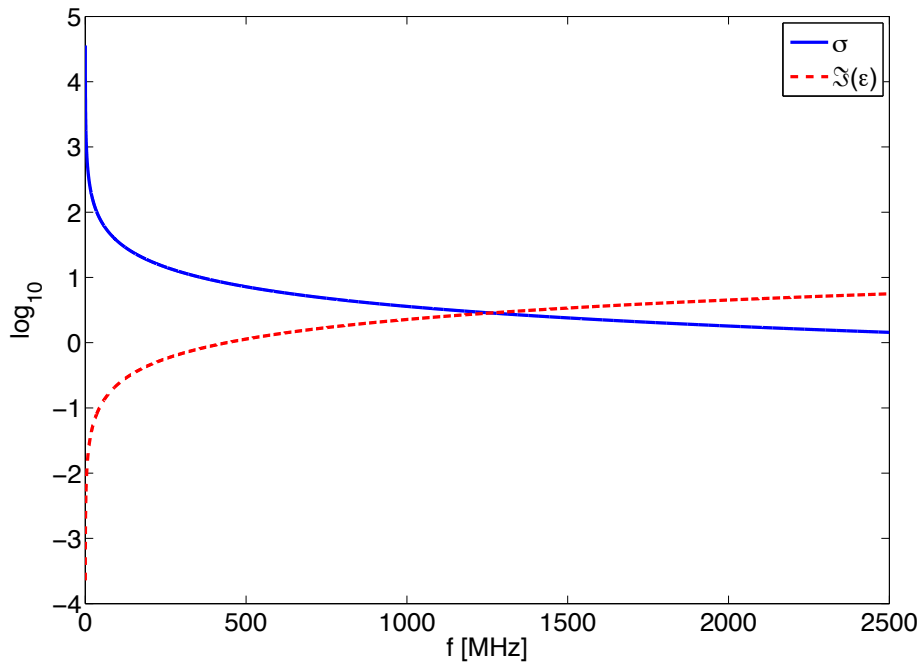


Figure 2.1: Comparison of the losses inside muscles, which happen due to electric conductivity, and relaxation of electric dipoles, the parameters are taken from Gabriel et al.: [1]

This could be observed in figure 2.1, which compares the RF losses generated in muscles, due to conductivity, and due to electric dipole relaxations. As observed in figure 2.1,

within the first 100 MHz, the conductivity losses are dominating.

Because of the large wavelength of electromagnetic radiation, λ , the electromagnetic energy is homogeneously distributed within the biological tissue, for example at 100 MHz the wavelength is 3 m in free space, and at 10 MHz the wavelength is 30 m, thus (2.18) could be simplified to:

$$P_{loss} = \sigma(\mathbf{r})|\mathbf{E}(t)|^2, \quad (2.19)$$

this equation suggests that the spatial distribution of the losses depends only on the local conductivity of the material.

In all the cases, it is simpler to deal with the propagation and the reconstruction in the case of a very short pulse of radiation, ideally a delta pulse: $\delta(t)$. In practice, most of the reconstruction algorithms are based on the fact that the excitation is a delta pulse or a delta pulse like.

2.2.2 Thermoacoustic waves generated from laser radiation

Although both optical waves and radio waves are electromagnetic waves, because of the difference in the wavelength they interact differently with materials. Thus, their properties vary. Unlike radio wave, optical waves interact with materials through two basic mechanisms, scattering defined by: μ_s , and absorption defined by: μ_a .

When a photon of light meets a particle, it either gets scattered by that particle (changes direction) or gets absorbed by that particle, meaning the energy is transferred from the photon to the particle. Both scattering and absorption are wavelength dependent, and these spectral characteristics change from one material to another, for example DNA strongly absorbs light in the ultraviolet (UV) band. While oxygenated and deoxygenated haemoglobin strongly absorb light at 532 nm, this absorption then drops several orders of magnitude down in the near infrared. While the absorption of water increases dramatically in the mid-infrared, in comparison to the near-infrared and the visible, see figure 2.2.

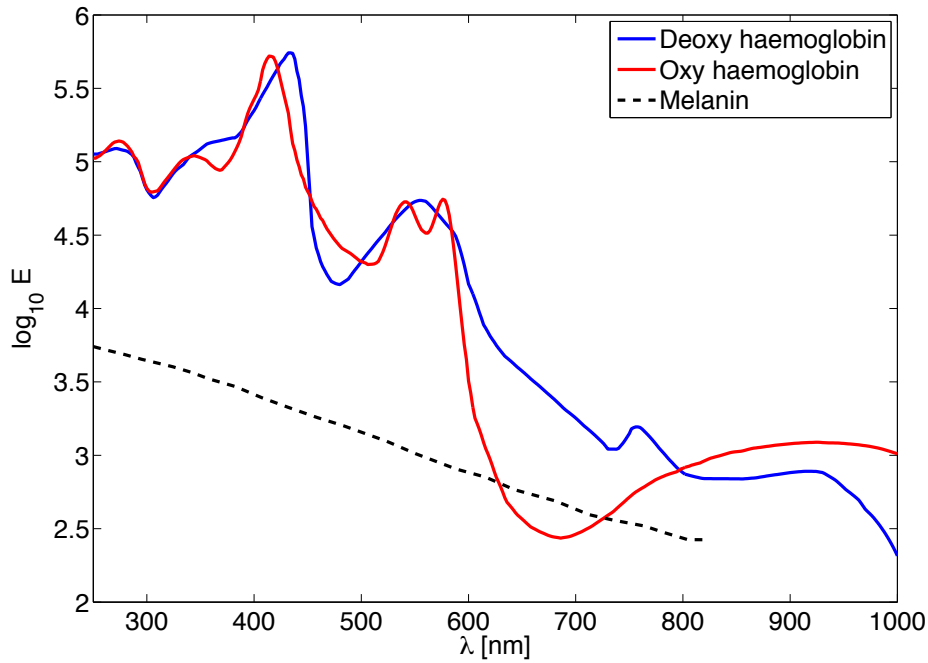


Figure 2.2: Extinction coefficient of different biological material.

Because of the smaller wavelength of light, compared to the wavelength of radio waves, as well as the higher scattering of light within biological tissues. Because of this dependence, it is not correct to assume a homogeneous distribution of energy inside the tissue. Rather this absorption is weighted by the light fluence $\Phi(\mathbf{r})$, which is the distribution of light energy inside the tissue. In this case, the power deposition inside the tissue $P_{loss}(\mathbf{r})$, is determined by both the light fluence, and by the absorption coefficient at this coefficient [20,21]:

$$P_{loss}(\mathbf{r}) \propto \mu_a(\mathbf{r})\Phi(\mathbf{r}). \quad (2.20)$$

Although there are several methods to distinguish between the absorption and the optical fluence parts in (2.20). It is not an easy problem, and it requires knowledge about some optical properties of the tissue, as well as measuring the sample at different optical wavelengths.

2.3 Propagation of ultrasonic waves

Ultrasonic waves or ultrasound, are diffracting mechanical waves that need a medium for propagation, in comparison to EM waves that can propagate in free space. Ultrasonic waves exist in many forms, such as longitudinal waves, and shear waves. Longitudinal waves are a major component used in ultrasound imaging, and in thermoacoustic imaging as well. They are called like that because the displacement of the waves is in the same direction, or in the opposite direction to the direction of propagation of the wave while EM waves are transversal waves. Finally, ultrasonic waves are scalar waves, in comparison to electromagnetic waves, which are vectorial waves.

Aside from these differences, a similar equation governs the propagation of ultrasonic waves, the scalar Helmholtz equation, or the scalar wave equation:

$$\nabla^2 p(\mathbf{r}, t) - \frac{1}{v_s^2} \frac{\partial^2 p(\mathbf{r}, t)}{\partial t^2} = 0, \quad (2.21)$$

(2.21) is similar to (2.4), except for the term on the right side of the equation. Thus it is called the homogeneous wave equation while (2.4) is called an inhomogeneous wave equation. In the further discussions, we will be referring to (2.4) when discussing the wave equation or Helmholtz's equation.

Like electromagnetic waves, ultrasonic waves experience reflection and refraction when the wave passes from one ultrasonic medium to another; the reflection depends on the acoustic impedance of the two mediums:

$$Z = \rho v_s, \quad (2.22)$$

where: ρ is the density of the medium. For the case of two different media, the reflection coefficient R , which is the ratio of the intensities of the reflected wave to the incident one is given by:

$$R = \left(\frac{Z_2 - Z_1}{Z_2 + Z_1} \right)^2, \quad (2.23)$$

and the transmission coefficient, T , is given by:

$$T = \left(\frac{2Z_2}{Z_2 + Z_1} \right)^2, \quad (2.24)$$

if the wave is incident at an angle θ_1 to the normal between medium 1, and medium 2, then it is reflected at an angle θ_1 , and emerges in medium 2 at an angle θ_2 given by Snell's law:

$$\frac{\sin \theta_1}{v_{s1}} = \frac{\sin \theta_2}{v_{s2}}, \quad (2.25)$$

this equation is visualized in figure 2.3.

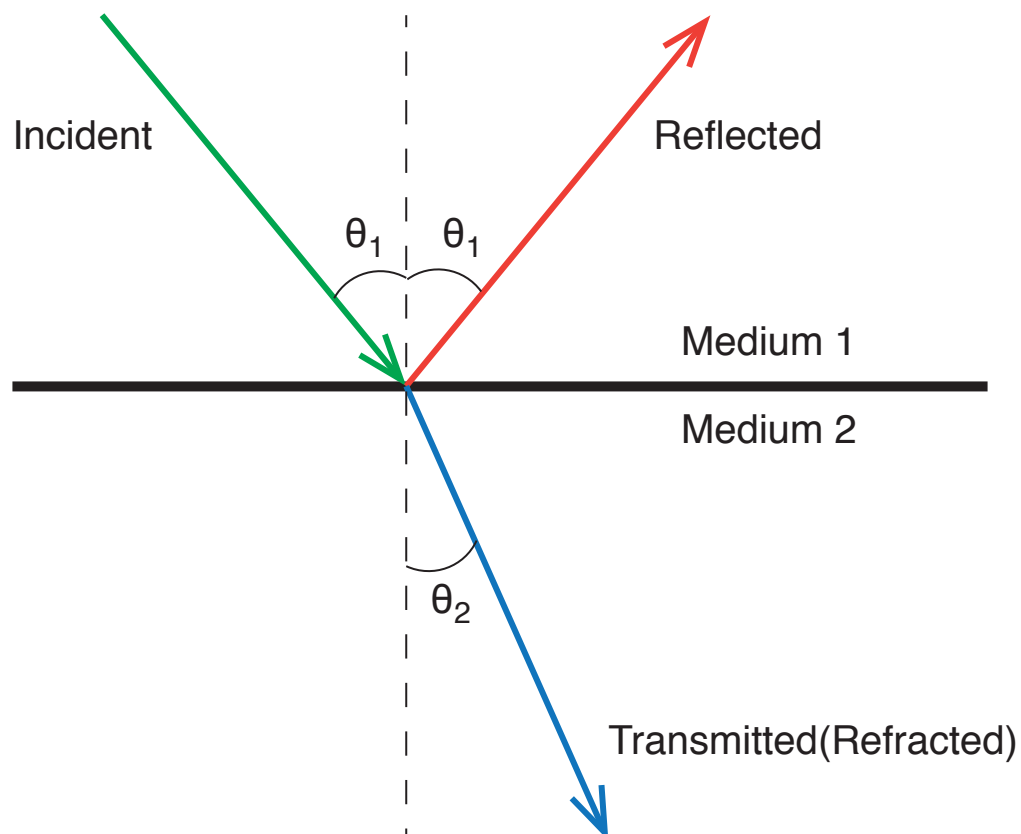


Figure 2.3: A graphical representation of Snell's law.

Fortunately in the case of imaging of soft tissues, the densities, and the speed of sound

in the different tissues are similar, thus for thermoacoustic imaging, it is a good approximation to consider the waves propagating in straight lines, and that they do not experience any kind of reflection, or refraction.

Finally, although shear waves exist inside biological tissues, they are much slower than longitudinal waves; longitudinal waves propagate in biological tissues at a speed of 1500 m/s. Shear waves on the other hand, propagate at a speed of 1-10 m/s, thus during a typical measurement window, 2-40 μ s, the effect of the generated shear waves is not observed. Moreover, as water is usually used as a coupling medium, between the sample and the ultrasonic array, shear waves do not reach the detector in the first place because they do not propagate in water.

2.4 Image reconstruction

Among the years, many reconstruction methods were developed for thermoacoustics. In the time domain there are two major classes of algorithms; the first one is called the space-time beamformers, and the second one is called model-based reconstruction [31].

Space-time beamformers are fast algorithms, and they have been widely used in other imaging systems, such as in synthetic aperture radar imaging and ultrasound imaging. Two examples of space-time beamformers are the delay and sum algorithm, and the filtered back-projection algorithm [31, 32].

The other class of time domain reconstruction algorithms is called model-based algorithms, where a mathematical model of the system is calculated, and then using optimization techniques, such as LSQR, a solution is found. Although these algorithms could be more accurate than space-time beamformers, and additional information, like the propagation of ultrasound waves, and the properties of the ultrasonic detectors could be incorporated into the model. Accounting for these properties is not easily done using the space-time beamformers. Nonetheless, model-based algorithms are slower and much more demanding in terms of memory than beamforming algorithms. In this dissertation, we use space-time beamformers to reconstruct the images.

Frequency domain methods exist as well [22, 24], but they are not as intuitive as the time domain methods are. Thus, we use only time domain methods.

In all the cases, the higher the number of measurements (projections), the better the reconstruction is, and the fewer artifacts appear in the reconstruction. The reason is that the increased number of measurements results in spatial averaging, which increases the signal-to-noise-ratio (SNR), in a similar way to time averaging [33]:

$$SNR \propto \sqrt{N_{projections}}. \quad (2.26)$$

2.4.1 Tomographic case

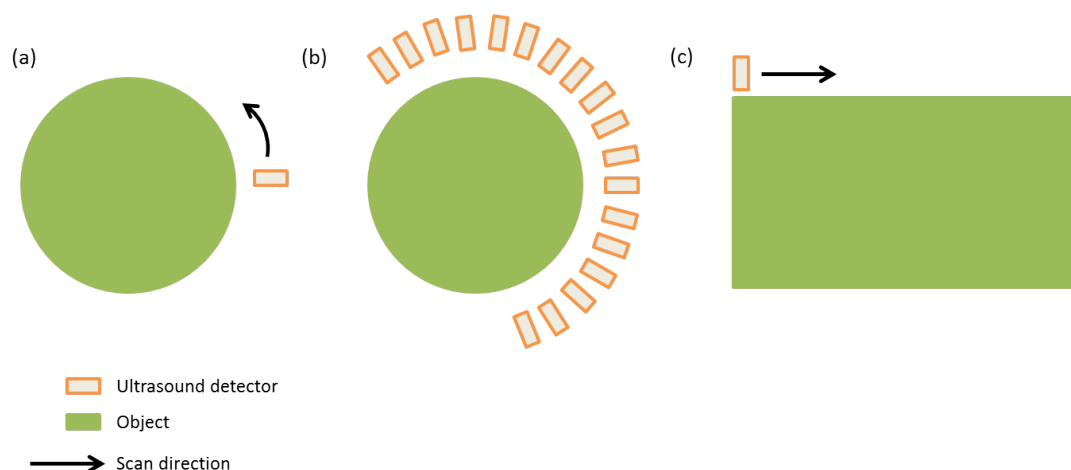


Figure 2.4: Different measurement geometries: (a) A single detector is scanned around the object, (b) an array of detectors is surrounding the object, (c) a single element detector is scanned above the object.

Tomography refers to imaging by sections, or sectioning, it comes originally from the Greek words *tomos* (part or section), and *graphein* (to write).

In tomography, the detectors are usually placed on a circle around the object, and the signals are assumed to come from a single plane. This configuration is physically achieved by using cylindrically focused detectors, and detector arrays that are sensitive only for signals coming from a single plane. As the detectors are placed on a circle, their distance to

the center of the sphere r is constant, while their angle ϕ changes from $0 - 360^\circ$, when fully surrounding the object. For the tomographic case, the reconstruction is usually performed using space-time beamformers, this includes the delay and sum algorithm, and the filtered back projection algorithm [32, 34]. When the signals measured using the detector at position \mathbf{r}_i , from a signal generated at pixel \mathbf{r}_j : $p_i[t_{ij}]$, where t_{ij} is the time of flight between the detector at position \mathbf{r}_i and the pixel at \mathbf{r}_j , then the intensity of that pixel is given by:

$$I(\mathbf{r}_j) = C \sum_i \left[p(t_{ij}) - t_{ij} \frac{\partial p(\mathbf{r}_i, t_{ij})}{\partial t} \right], \quad (2.27)$$

where C is a constant composed of all the other constants, for most cases C could be dropped out. In (2.27) there are two terms, the direct term, and the derivative term. The derivative term is the dominant term, thus for most practical cases (2.27) could be reduced to:

$$I(\mathbf{r}_j) = - \sum_i \frac{\partial p(\mathbf{r}_i, t_{ij})}{\partial t}. \quad (2.28)$$

On the other hand if the direct term of (2.27) is taken, then the solution takes the following form:

$$I(\mathbf{r}_j) = \sum_i p(t_{ij}), \quad (2.29)$$

we call this solution the delay and sum algorithm, and it represents one of the two basic variations of (2.27). Generally (2.28) gives a higher weight to higher frequencies, while (2.29) gives the same weight for all the frequencies, giving an image that is not very sharp on the boundaries. Both of the algorithms are used interchangeably in practice, and the generated image that looks better and more representative is the one that is used in the end.

2.4.2 Raster scanning

There are several cases where it is desirable to perform raster scanning of the specimen, rather than tomographic imaging. Two basic cases are; access is not available from all the sides, like in clinical applications and high-frequency scanning, where only single element

high-frequency detectors are available. Although raster scanning will generate worse resolution than tomography, see section 2.4.3, sometimes it is not avoidable to do it. In such cases a single element is raster scanned, hence the name raster-scan, above the sample. For high resolution imaging, high-frequency detectors are used because the resolution is proportional to the frequency, see section 2.4.3. If focused detectors are used then the imaging volume is limited to the focus of the detector, for this point detectors are desired. Unfortunately the sensitivity of the detector is proportional to the surface area of the active element, this means that for point detectors or extremely small ones, the sensitivity approaches zero. To overcome this limitation we decided to use spherically focused detectors, and consider the focal spot as a punctual detector or a virtual detector. This way the sensitivity is increased because of the huge area of the physical detector, and all the characteristics of point detectors are maintained when imaging after the focal region [35, 36].

In raster scanning, the detector is scanned in a two dimensional plane, the $z = 0$ plane, after acquiring measurements from all the positions, three-dimensional beam-forming or three dimensional tomographic methods are used in a similar way as in the case of tomography¹, see section 2.4.1, except that the signals are back-projected to a 3D grid, slowing down the reconstruction. In such a case a usual reconstruction takes several weeks, to accelerate it we reconstruct on a graphical processing unit (GPU). This way the reconstruction that would take days is done in less than one hour. Essentially raster-scanning with point detectors is a special case of tomography where the detectors lie on a single plane rather on a circle. In this case the angular coverage is defined by the angle of acceptance of the individual detectors rather than by the angle they cover around the object, in a typical case where spherically focused detectors with an $F_{\#} = 1$ are used, the angle of acceptance equals 60° . The $F_{\#}$ is defined as:

$$F_{\#} = \frac{F}{D}, \quad (2.30)$$

where F is the focal distance of the detector, and D is the diameter of the active element, figure 2.5 shows an example of this.

¹Tomographic methods means that computational methods are used to generate the final image.

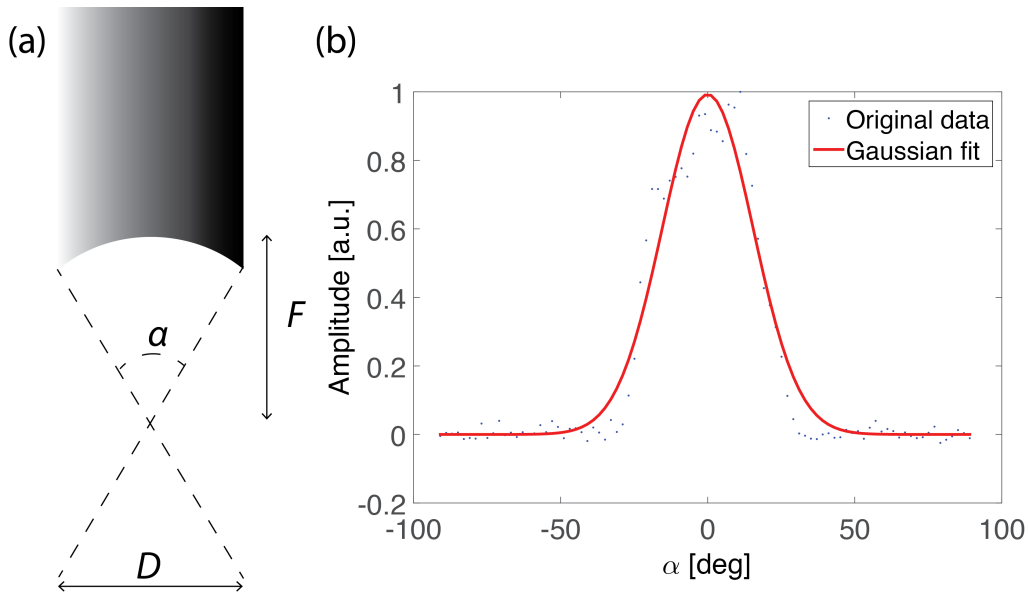


Figure 2.5: (a) Definition of the geometry used, (b) an example from a real detector, showing the angular acceptance of the detector.

2.4.3 Resolution, and scanning steps

There are several resolution criteria, one of them is the Rayleigh criterion, which is the minimum distance between two objects generating the same signal amplitude, such that it is possible to differentiate between the two objects. Another criterion for resolution is the full-width-at-half-maximum (FWHM) of the point spread function of an infinitely small object, mathematically represented by a delta function $\delta(\mathbf{r})$. In thermoacoustics, the resolution depends on three things; the frequencies employed, the F-number of the detector $F_{\#}$, and the scanning geometry, whether it is tomographic or along a line.

Resolution in raster-scan systems

Scanning along a line is a special case of tomography, where the angular coverage of the object is defined by the transducer characteristics. In case of focused transducers, these are the center frequency of the transducer f_c , and the $F_{\#}$. For the transverse direction this is given by [37]:

$$\delta x = 1.22\lambda \cdot F_{\#}, \quad (2.31)$$

where, $F_{\#}$ is defined in (2.30), and λ_c is the wavelength frequency f :

$$\lambda = \frac{v_s}{f}, \quad (2.32)$$

although this equation is a good first order estimation of the achievable resolution, for broad-band measurements, such as the ones used in thermoacoustics, the whole bandwidth plays a role in defining the resolution. In the next section, we will derive an expression for the lateral resolution of a broadband thermoacoustic system.

Derivation of the in-plane resolution for raster scans

The bandwidth of a detector (BW), defined as the set of frequencies between the lower cutoff frequency (f_{Low}), and the upper cutoff frequency (f_{High}). Moreover at every frequency (f), the detector has a sensitivity of $A(f)$. Assuming that the detector is a linear system, then the principle of superposition applies, thus the width of the focus, defining the eventual resolution, is a weighted average of the widths at the individual frequencies, or wavelengths:

$$\delta x = 1.22 \frac{\int_{f_{Low}}^{f_{High}} A(f)(v_s/f)df}{\int_{f_{Low}}^{f_{High}} A(f)df} F_{\#}, \quad (2.33)$$

discretizing (2.33) gives:

$$\delta x = \frac{\sum_{i=1}^N A_i(v_s/f_i)}{\sum_{i=1}^N A_i} F_{\#}, \quad (2.34)$$

where $f_1 = f_{Low}$, and $f_N = f_{High}$.

To simplify (2.34), we can derive an effective wavelength, λ_{eff} , which corresponds to the resulting resolution as:

$$\lambda_{eff} = \frac{\sum_{i=1}^N A_i(v_s/f_i)}{\sum_{i=1}^N A_i}, \quad (2.35)$$

this way the lateral resolution is given by:

$$\delta x = \lambda_{eff} \cdot F_{\#}. \quad (2.36)$$

From (2.34) the following result could be obtained:

If the bandwidth of the detector is symmetric around the center frequency: (f_c), then the effective wavelength, λ_{eff} , is larger than the central wavelength λ_c , thus the resolution gets dominated by the lower frequencies.

This could be seen from the following example: if we have a detector with a symmetric spectrum of two frequencies around the center frequency (f_c), the lower frequency is given by $f_{c1} = f_c - \Delta f$, and the higher frequency is given by: $f_{c2} = f_c + \Delta f$, because the spectrum is symmetric f_{c1} , and f_{c2} have the same weight, A . From (2.35), the effective wavelength is:

$$\begin{aligned}
 \lambda_{eff} &= \frac{A(v_s/(f_c - \Delta f)) + A(v_s/(f_c + \Delta f))}{2A} \\
 &= \frac{(v_s/(f_c - \Delta f)) + (v_s/(f_c + \Delta f))}{2} \\
 &= \frac{v_s f_c}{f_c^2 - \Delta f^2} \\
 &= \frac{v_s}{f_c - \Delta f^2/f_c}.
 \end{aligned} \tag{2.37}$$

This result means that the influx of low frequencies will degrade the resolution in raster-scan systems, such as RSOM, this degradation is worse than what is predicted by the center frequency. As seen from (2.37):

$$\lambda_{eff} > \lambda_c \Rightarrow \delta x_{eff} > \delta x_c. \tag{2.38}$$

This result emphasizes the degradation in resolution, and it becomes even more important for spectra that are not symmetric around the center, as is usually the case for most detectors.

Axial resolution for raster scans

The axial of a raster scan system is given by:

$$\delta z = \frac{0.88 \times v_s}{BW}. \tag{2.39}$$

Because of the importance of the axial resolution, we will derive it here. This derivation is based on the assumption that the impulse response $p(t)$ of the detector could be approximated as a gaussian-modulated sinusoidal function [38, 39]:

$$p(t) = Ae^{-\frac{(t-t_0)^2}{2\delta^2}} \times \cos(2\pi f_0 t + \phi), \quad (2.40)$$

Where t is time, A is the amplitude of the impulse response, f_0 is the central frequency of the transducer, and t_0 , σ , and ϕ are constants. In such a case the axial resolution δz would be given by the FWHM of the temporal gaussian envelope:

$$\delta z = 2\sqrt{2 \ln 2} \sigma \times v_s. \quad (2.41)$$

The Fourier transform of (2.40) is the following:

$$P(f) = A \frac{1}{2\sqrt{\pi}} \cdot \delta e^{-j2\pi f(t_0 - \frac{\phi}{2\pi f_0})} \cdot \left[e^{-2\pi(f-f_0)^2 \delta^2} - e^{-2\pi(f+f_0)^2 \delta^2} \right]. \quad (2.42)$$

The acoustic -6 dB bandwidth BW is approximated by the FWHM of the Gaussian peak of $P(f)$ as:

$$BW = \frac{\sqrt{2 \ln 2}}{\pi \delta}, \quad (2.43)$$

substituting (2.43) into (2.41) gives:

$$\delta z = \frac{4 \ln 2}{\pi} \cdot \frac{v_s}{BW} \approx 0.88 \frac{v_s}{BW}. \quad (2.44)$$

This formula for the axial resolution is an approximation, because it accounts for both the positive peak, and the negative peaks, based on our assumption of a gaussian envelope the negative peaks are smaller in amplitude than the positive ones. Thus, if only the positive peak is considered, the resolution improves. Thus in practice it should not be surprising if the resolution achieved is better than what is achieved with (2.44).

Resolution in the tomographic case

As for tomography, the in plane resolution is solely defined by BW :

$$\delta xy = \frac{0.88 \times v_s}{BW}, \quad (2.45)$$

this equation is similar to the axial resolution of scanning along a line case, see (2.39). As for the resolution achieved between the tomographic planes, this is similar to the case of a line scanning, (2.31), and it is given by:

$$\delta z = \lambda_c \cdot F_{\#}. \quad (2.46)$$

Choosing the scanning and the reconstruction step size

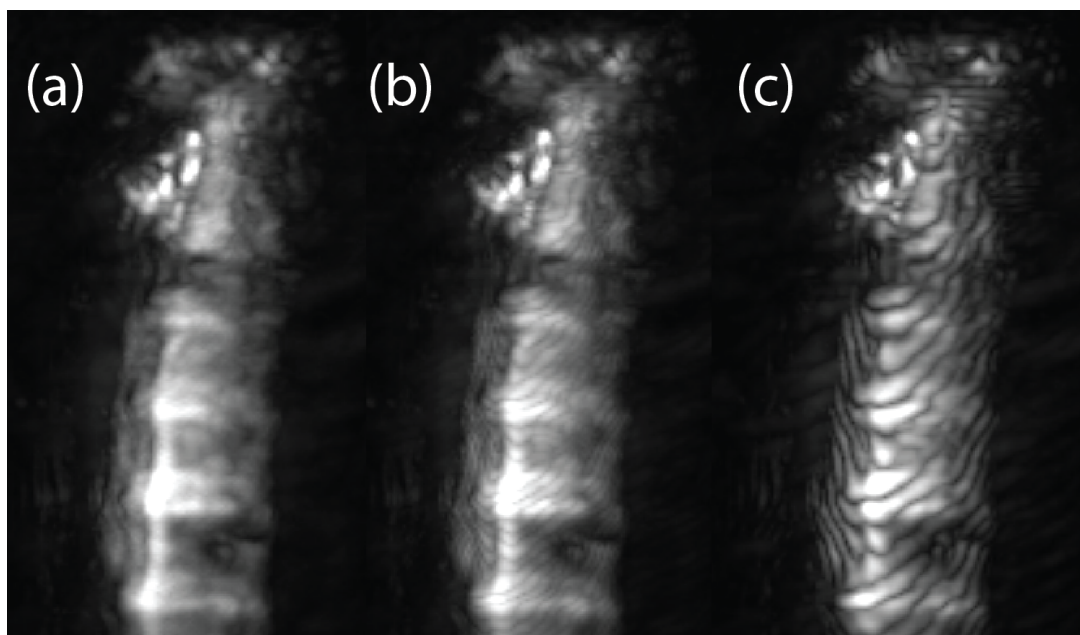


Figure 2.6: Example of aliasing when choosing the wrong z-discretization. (a) Discretization is $2.5 \mu m$, (b) discretization is $5 \mu m$, and (c) discretization is $10 \mu m$

Now, after defining the resolutions, we can start talking about the necessary step sizes for measurements, and for reconstruction to insure that all the information is represented on it. If the step size is small, then we get an image with better SNR, because of spatial averaging, see (2.26), but the measurement and the reconstruction will take a longer time. On the other hand, if the step size is large, then the image will be noisy, aliasing effects will

appear according to the Nyquist theorem, and the resolution degrades. Because of this, in the case of raster-scanning the step size needs to be half of the resolution.

For the tomographic case, the step size along the z-axis needs to be again half of the attainable resolution, and the angular step needs be half the beam width.

As for reconstruction, again If the grid step sizes are larger than the minimum step size such effects as aliasing starts occurring. See figure. Thus, to avoid such effects good care needs to be taken when choosing both the measurement grid, and the reconstruction grids.

2.4.4 Static vs. moving illumination

In section 5.2 we will describe a system based on static illumination, while in section 5.4 we will describe one where the illumination moves with the detection (dynamic). Both illumination types have their advantages, and disadvantages and the choice of one over the other usually depend on the imaged sample, and on the FOV to be scanned. Generally trans-illumination would be the choice for imaging of thin samples with a small FOV, in such a case the illumination could be made homogeneous, or quasi-homogeneous all over the sample, which could be achieved either by adding a diffuser in the path of the illumination beam, or by using turbid agar for embedding the sample. Other benefits of having a static illumination is the coherence of the signals generated², which is an assumption in the reconstruction code.

Nonetheless, in some cases it is not easy to have a static illumination, this is either the case when the FOV to be scanned is large, it becomes difficult to illuminate efficiently the whole FOV [40]. Thus, the illumination needs to be moved with the detection, or in the case of epi-illumination, where the position of the fibers is in the way of the detector, thus it is possible to scan only a small FOV, in this case as well the illumination needs to be moved together with the detector.

²Coherence here means that the signals generated while the detector is at position A, are the same signals generated when the detector is at position B.

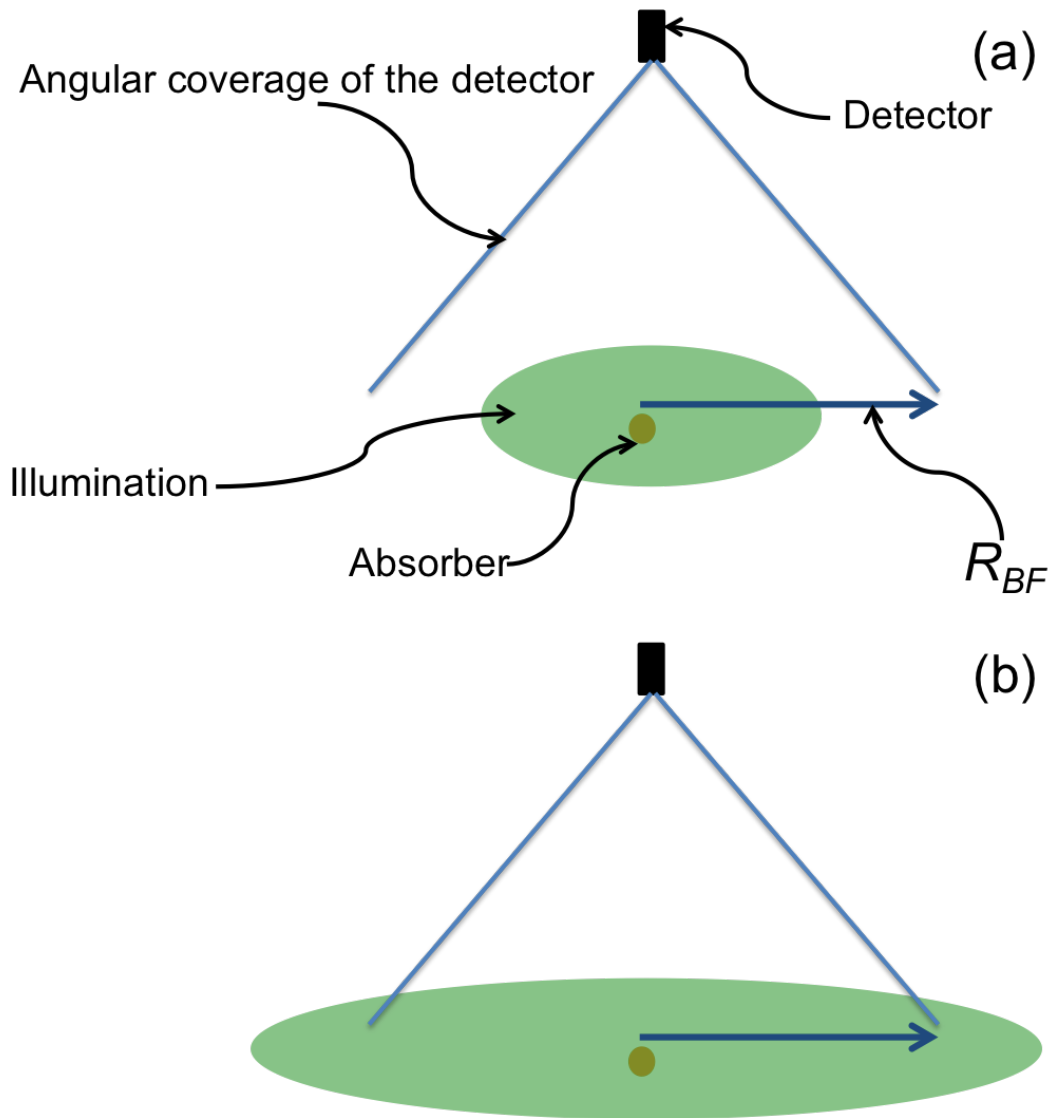


Figure 2.7: Comparison of a two illumination schemes, once with the radius of illumination smaller than R_{BF} (a), and once the radius of illumination is larger than R_{BF} (b).

In all the cases moving the illumination with detection puts a concern over the coherence of the generated signals, to address this it is necessary to illuminate homogeneously at least within what we call the beamforming radius (R_{BF}), this is the radius corresponding to the detector positions which are necessary to reconstruct a point (x_i, y_i, z_i) . In addition to the distance from the focus of the detector, R_{BF} depends on the angle of acceptance of the detector (α), if the distance from the focus point of the detector is: $|z_i|$, then R_{BF} is given by:

$$R_{BF} = |z_i| \tan(\alpha/2). \quad (2.47)$$

If the radius of illumination ($R_{illumination}$) is larger than R_{BF} , i.e.:

$$R_{illumination} \geq R_{BF}, \quad (2.48)$$

Then the generated signals are quasi-coherent, and the larger the radius of illumination is, the better the coherence is. In biological samples, this is usually the case because of the high scattering within the biological tissue, see figure 2.7

2.5 Multifrequency reconstruction

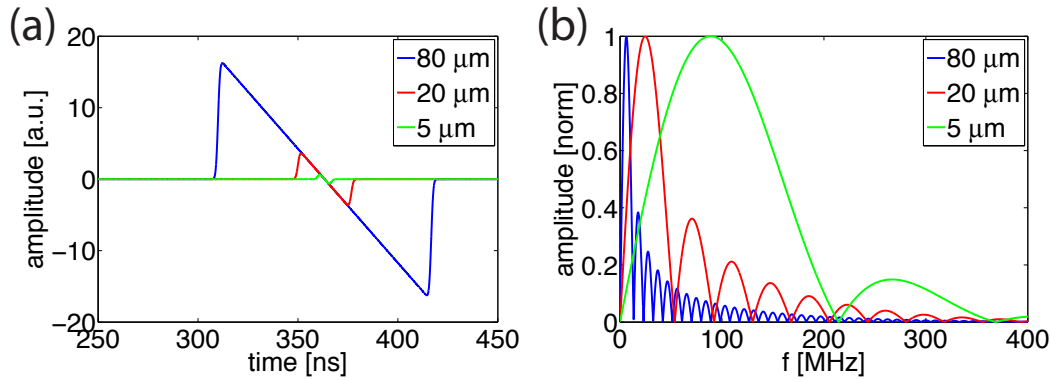


Figure 2.8: Thermoacoustic signal generated from a small sphere with different radii, (a) time domain signals, and (b) their frequency contents.

In the case of raster-scan optoacoustic mesoscopy (RSOM), see chapter 5, ultra-wideband ultrasonic detectors are employed, for example our 100 MHz detector spans a bandwidth (BW) from 10 MHz to 180 MHz, a similar statement could be said about the 50 MHz detector, which spans a BW from 10 MHz to 90 MHz. Such ultrawide bandwidths have in them both low frequencies which are less attenuated, they have higher amplitude than high frequencies, and subsequently they have a higher SNR, than corresponding high-frequencies. The reasons for this are multifold:

1. Lower frequencies correspond to larger objects; these objects absorb more energy, because the absorbed energy is proportional to the diameter of the object. Thus, they have larger amplitude:

$$A = C\mu_a D, \quad (2.49)$$

where: A is the amplitude of the generated optoacoustic signal, C is the proportionality constant, μ_a is the optical absorption of the object, and D is the diameter of the structure, or the object. Thus, considering the same absorption μ_a larger structures generate higher amplitude signals than smaller structures, which generate high frequencies, see figure 2.8.

2. Low frequencies are less attenuated than high frequencies; attenuation follows an exponential law [41]:

$$\alpha(f) = \alpha_{0f}|f|^n, \quad (2.50)$$

Where n is a real positive number, for normal tissue it is equal to 1, and for water, it is equal to 2. α_{0f} is the attenuation coefficient at the starting frequency. From (2.50) it is obvious that after propagating the same distance, high frequencies are more attenuated than low frequencies.

From the above mentioned we see that high frequencies have lower SNR than low frequencies. Because of this when all the frequencies are reconstructed together, then the high-frequencies are buried within the low frequencies. Thresholding the image won't help as this will bring up low-frequency noise together with the high frequencies. Thus, it is advantageous to separate the reception bandwidth into smaller sub-bands, and reconstruct the signals only within these sub-bands. After processing the sub-bands separately, the different images are combined again under different colors corresponding to the different sub-bands, the different sub-bands could be divided based on one of the following criteria:

1. Divide the bandwidth into N sub-bands, where all have the same bandwidth:

$$BW_1 = BW_2 = \dots \quad (2.51)$$

although this might be the most straightforward way, it suffers from the fact that the relative bandwidth $BW_{i\%}$ defined as:

$$BW_{i\%} = \frac{BW_i}{f_{ci}}, \quad (2.52)$$

where: BW_i is the bandwidth of the i th sub-band, and f_{ci} is the center frequency of the i th sub-band, becomes smaller and smaller. This shrinkage of the relative bandwidth towards the higher frequencies generates ringing artifacts at the higher sub-bands.

2. Divide the reception bandwidth into N sub-bands, with all the frequencies having the same relative bandwidth:

$$BW_{\%} = \frac{BW_1}{f_{c1}} = \frac{BW_2}{f_{c2}} = \dots \quad (2.53)$$

To find the cutoff frequencies, we need to define the very first cutoff frequency, the lowest cutoff frequency of the detector f_0 , as well as the relative bandwidth $BW_{\%}$, once this is defined, the next cutoff frequency, f_1 , is found from (2.52), as:

$$BW_{\%} = \frac{BW_1}{f_{c1}} = \frac{f_1 - f_0}{\frac{f_1 + f_0}{2}}, \quad (2.54)$$

from (2.54), we find f_1 as:

$$f_1 = \frac{2 + BW_{\%}}{2 - BW_{\%}} f_0, \quad (2.55)$$

which could be generalized as:

$$f_{i+1} = \frac{2 + BW_{\%}}{2 - BW_{\%}} f_i. \quad (2.56)$$

To optimally use the reception bandwidth of the detector it is instructive to divide the sub-bands in such a way that they fill the full reception bandwidth. This optimization could be done by choosing a few different values for the relative bandwidth, and calculating the cutoff frequencies, once the last cutoff frequency coincides with the upper cutoff frequency of the detector, then this relative bandwidth is chosen as optimum. For example, for a detector with reception frequency of 10-180 MHz, the optimum cutoff frequencies would be: 10 MHz, 26 MHz, 67.8 MHz, and 176.5 MHz, at a relative bandwidth of 89%.

3. Another way in dividing the bandwidth into sub-bands is using the wavelet transform [42]. The wavelet transform is a structured way in dividing the bandwidth into smaller sub-bands. It is a mathematical representation of a square integrable function by a certain orthonormal series generated by a wavelet [43]. The wavelet transform decomposes the signal into two parts by passing it through a low pass filter, generating what is called approximation coefficients, and again by passing it through a high pass filter, generating what is called detail coefficients [44]. This procedure could be repeated again on the approximation coefficients, generating a second level of detail and approximation coefficients, see figure 2.9:

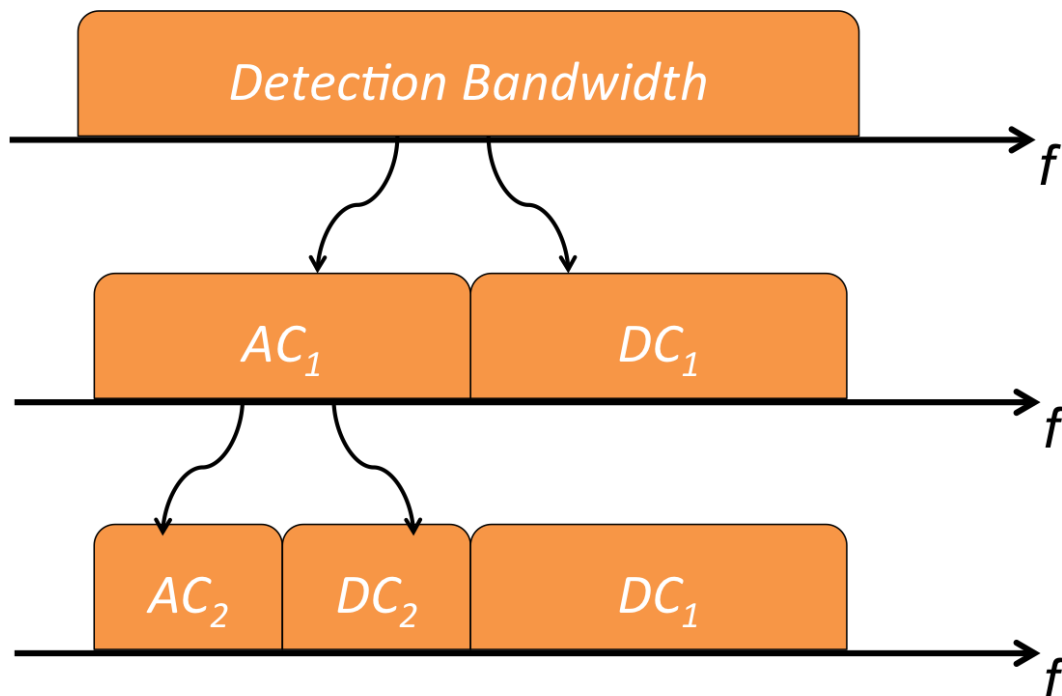


Figure 2.9: Representation of the wavelet decomposition of the detection bandwidth, into detail coefficients (DC), and approximation coefficients (AC), this procedure could be repeated again on the AC coefficients.

Following the above-mentioned procedure will result in a systematic way of dividing the reception bandwidth of the ultrasound detector, into smaller sub-bands, where every sub-band is half of the previous one.

Not only this can divide the bandwidth into smaller bands; this method could be used for denoising of the signals as well [45].

One drawback of the wavelet method is its relatively slow speed in comparison to the other methods based on FFT implementations, thus in the examples that will follow only the first two methods have been used so far.

The three different ways of dividing the reception bandwidth, are graphically summarized in figure 2.10.

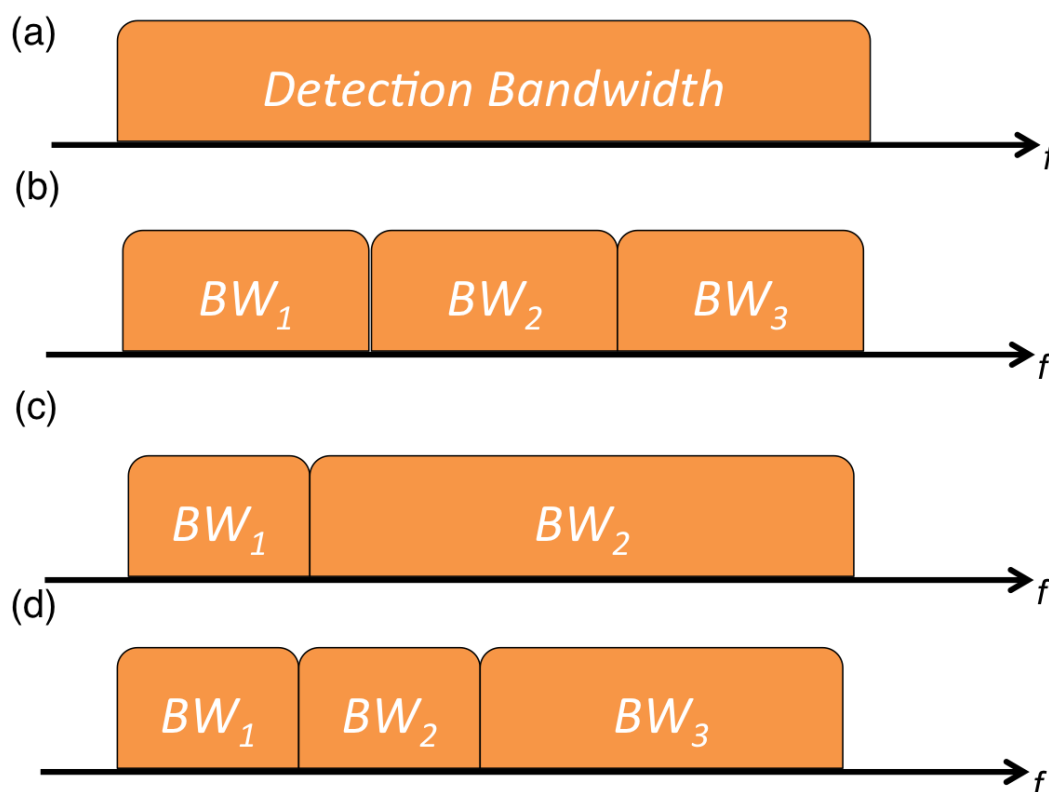


Figure 2.10: (a) Full detection bandwidth, (b) division into sub-bands with equal bandwidths, (c) division into sub-bands with equal relative bandwidths, and (d) division into sub-bands where every sub-band has double the bandwidth of the previous one.

An example of the improvements that are achievable using multifrequency reconstruction is shown in chapter 6, as well as here in figure 2.11. In figure 2.11 it is obvious that using multi-frequency reconstruction recovers the small vessels, which generate the high frequencies, on the other hand reconstructing all the frequencies together masks the small structures.

Currently it is under investigation which kinds of filters is better to use, if there are other methods of dividing the bandwidth, as well as dynamic methods of dividing the reception

bandwidth. In this context we look into the different frequencies, and then we choose based on some statistical measures such as kurtosis the sub-bands that have the most information in them [46]. This is a promising and powerful technique, by choosing only the band where most information is contained we maximize both the information content, and the SNR as well by throwing away all the noise from the other bands³.

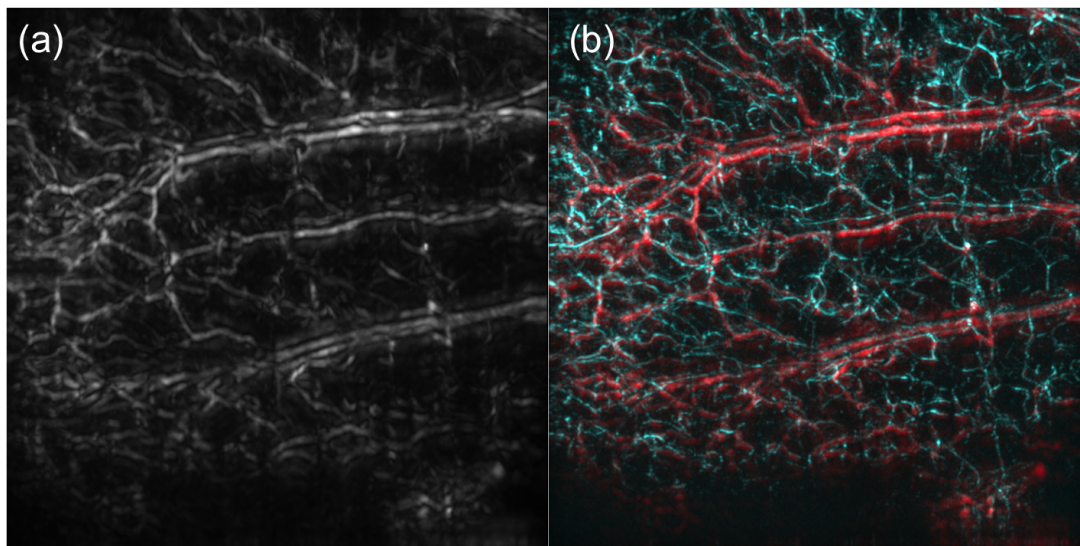


Figure 2.11: A comparison of the reconstruction achieved when: (a) reconstructing all the frequencies together, (b) performing multifrequency reconstruction. Adapted from Omar et al. [2].

2.6 Filtering in raster-scan optoacoustic mesoscopy

Because of the ultra-wideband nature of the detectors involved in the raster-scan optoacoustic mesoscopy (RSOM), filtering becomes an important aspect, both in terms of temporal filtering, and spatial filtering. Both kinds are needed, and as we will see, Fourier domain methods appear to be the best because of their simplicity, intuitiveness, and their fast performance based on the FFT implementation.

³This work is carried out by a master student of mine, Mr. Dimosthenis Koulikas, and in cooperation with Professor Leontios J. Hadjileontiadis from Aristotle University of Thessaloniki

2.6.1 Temporal filtering

Temporal filtering is needed in two cases; the first is to reject noise outside of the detection bandwidth, and the second is to divide the detection bandwidth into smaller sub-bands.

Temporal filtering is the easiest of both, because of the standardized methods for temporal filtering, to perform filtering we first employed Chebyshev zero-phase digital filter. In later implementations, we moved to direct exponential filtering of the 4th order in the frequency domain. This implementation saves enormous amounts of time in comparison to the built in filtering functions of Matlab, as this uses the fast implementations of FFT, and the fast matrices processing available in Matlab.

The filtering is implemented in such a way that the same attenuation per decade is applied on both sides of the bandpass filter, this assures that minimum ringing effects appear on the filtered version of the signal. If f_{low} is the lower cutoff frequency, and f_{high} is the high cutoff frequency, the transfer function $H(f)$ looks like the following:

$$H(f) = e^{-(f/f_{high})^4} (1 - e^{-(f/f_{low})^4}). \quad (2.57)$$

2.6.2 Spatial filtering

Spatial filtering is conceptually more complicated than temporal filtering, in part because there are no defined boundaries for filtering. Those boundaries could be found in temporal filtering either from the detector characteristics, or based on other characteristics, such as the definitions that come in the multi-frequency reconstruction.

Before going into the details of spatial filtering, it is worth to discuss the need for spatial filtering; focused, high-frequency ultrasound detectors are constructed from two parts: the active material and the acoustic lens. This combination results in a spherically focused ultrasonic detector, see section 3.1.3. The problem arises when a high-energy, laser pulse is incident on the sample, some of the photons, either through diffusion, reflection, or direct propagation reach the active material of the detector, generating an optoacoustic signal. This optoacoustic wave propagates towards the surface of the lens, as the acoustic mismatch is high between the lens and water, this wave is reflected back towards the active

material, resulting in a pulse bouncing back and forth between the active material and the surface of the lens, see figure 2.12. Every time the pulse reaches the active material a signal is measured, because this bouncing is not related directly to the sample but rather to the geometry of the lens, it happens almost always at the same time points, though with different amplitudes, depending on the amount of light that reaches the active element. Finally on the image, or on the b-scan this results in slow varying horizontal lines, with a strong amplitude, which might hide some weak features of the image behind it.

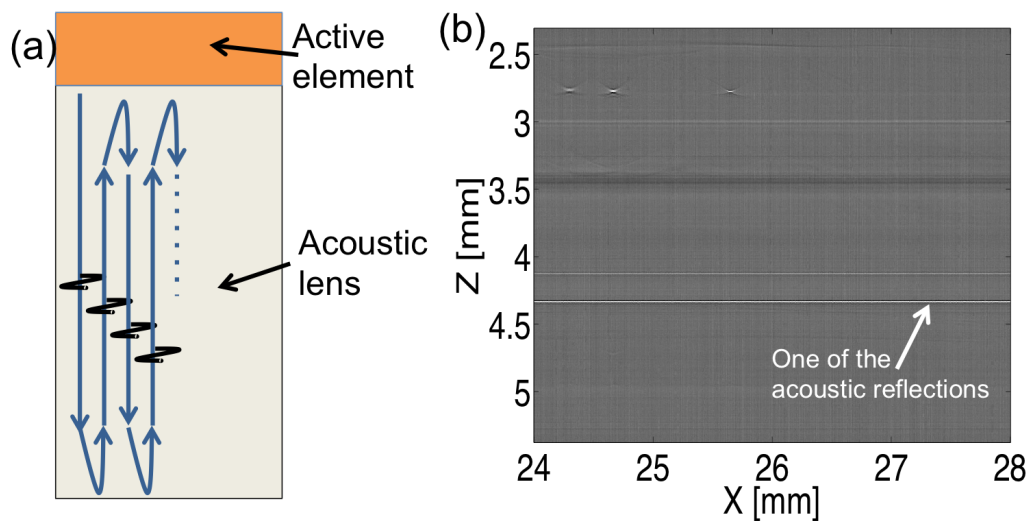


Figure 2.12: (a) Bouncing of the thermoacoustic signal between the active element, and the interface of glass and water, (b) appearance of the reflections on the b-scans.

Several measures could be taken to mitigate this: the first is to average all the signals within a single b-scan, and subtract this average from all the signals, this is fast. But, on the other hand, if there is a strong signal at one position, such a subtraction will pollute the neighboring signals. Another possibility is to use a high-pass filter, but rather than applying it temporally, apply it on the spatial direction, in such a way it becomes possible to filter out the DC, or quasi-DC part resulting from the reflections inside the acoustic lens. Finally, as these constant lines result in a constant z -plane on the reconstructed image, it is possible to apply spatial high-pass two dimensional filters on the image. Experience shows that this is the most efficient way for removing the reflections, an example of an image before and after is shown in figure 2.13.

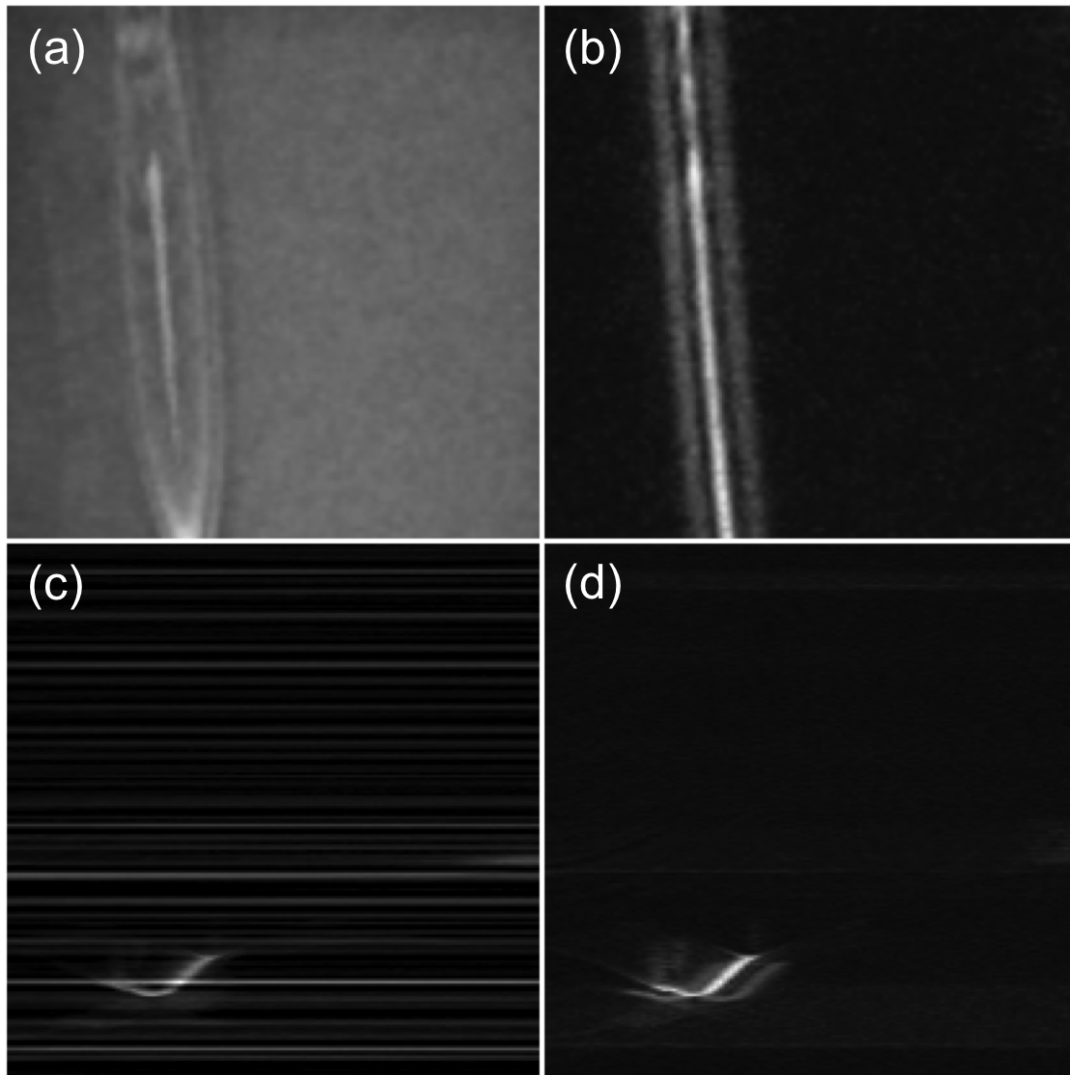


Figure 2.13: (a) MIP xy before filtering, (b) MIP xy after filtering, (c) MIP xz before filtering, (d) MIP xz after filtering.

2.7 Discussion

In this chapter, we discussed how a thermoacoustic signal is generated; this could be a result of absorption of radio frequencies or the absorption of laser pulses. In both cases, this absorption of energy results in the generation of acoustic waves at ultrasound frequencies, these acoustic waves are subsequently measured with ultrasound detectors. These ultrasound detectors could either form an array, in which case real-time detection and imaging is possible or single elements could be used, in which case scanning is necessary.

Afterward, we discussed how we can transform raw signals into a useful image, for our

case we implemented different beamforming algorithms, such as filtered back-projection, and the delay and sum algorithm. Although in both cases this is much faster than model-based reconstruction algorithms, in the case of raster-scanning with spherically focused detectors, this is even more critical, where the amount of generated data could not be processed using model-based approaches.

Afterward, we discussed resolution in thermoacoustics; this includes both axial and lateral resolution, we have observed that in the tomographic case, the lateral (in-plane) resolution is defined by the bandwidth of the detector. While the axial is defined by the geometrical properties of the transducer employed as well. On the other hand in the case of raster-scanning we have seen that the in-plane resolution is defined by the geometrical properties of the detector while the axial resolution is defined by the bandwidth of the detector.

Moreover, we looked into different possible ways of dividing the detection bandwidth into smaller sub-bands, to improve the SNR, and the visibility of higher frequencies. These methods include keeping the bandwidth of all the sub-bands equal, they also include keeping the relative bandwidth of all the sub-bands equal, and the wavelet decomposition. In this dissertation, we have mostly used the second method, and in some cases the first method. Other methods of dividing the reception bandwidth are currently under investigation as we have previously mentioned.

Finally, we discussed illumination, the limitation on dynamic illumination, and the different filtering methods applied, both temporal, and spatial.

This chapter should serve as basis for the further discussions related to the system design, and characterizations in the next chapters.

Chapter 3

Technology

In this chapter, we will be discussing the different technologies, and technological advances that are enabling for thermoacoustic imaging, both tomographic and mesoscopic. We will start first discussing ultrasonic detectors, then about lasers, motorized stages, and finally data acquisition.

3.1 Ultrasonic detectors

Ultrasound plays a major role in thermoacoustic imaging, as this is how thermoacoustic signals are detected. There are two kinds of detectors, high-frequency detectors, and low-frequency detectors. We discuss both kinds here. As there is no clear limit between low frequency and high frequency, we choose the frequency 20 MHz, where low frequencies are those below it, and high frequencies are the ones above it. This limit could be justified in two ways. From one side, this is almost the highest frequency for tomographic, and small animal imaging, while, above it, mesoscopic and microscopic systems start kicking in. On the other hand, this is where most array detectors exist, above this frequency mostly single element detectors are available, and used. Again, this is not an objective limit, for instance for some applications 1 MHz would be considered high, thus depending on the context this definition should be defined accordingly. Here we start first discussing what are the technologies used for ultrasonic detection, then we discuss low-frequency detectors, and finally high-frequency detectors.

3.1.1 Methods for the detection of ultrasound

Several methods and effects could be used to detect ultrasonic signals. In principle, any system that changes its state in response to mechanical perturbations could be used for this purpose, the most common are listed below:

1. Piezoelectricity: Detectors based on piezoelectricity are the most frequently used, this is a result of the abundance of piezoelectric materials in nature, as well as ease of manufacturing of such materials. Moreover, for low-frequency applications these detectors could be formed into almost any shape, this is important when considering focusing capabilities and different detection geometries.

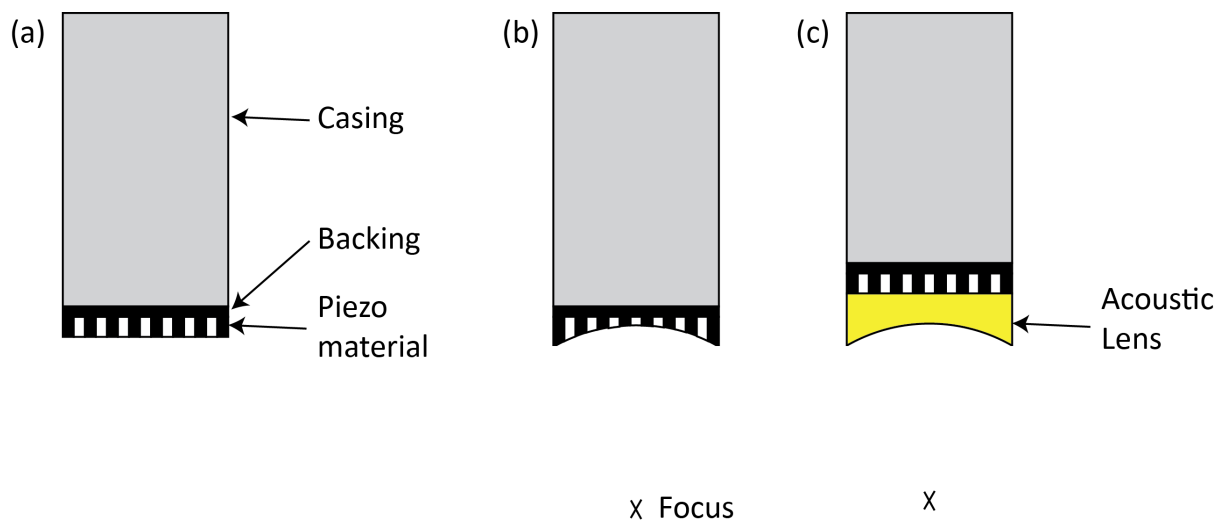


Figure 3.1: Different kinds of detectors: (a) unfocused detector, (b) spherically shaped detector for focusing, (c) focused detector using an acoustic lens.

Piezoelectric detectors (PZT¹) are built from piezoelectric crystals. The behavior of PZTs is described by the piezoelectric effect; where electricity is produced as a response to mechanical stress and vice versa. Such materials are either found in nature or manufactured.

Another possibility for manufacturing focused detectors is to shape the PZT crystal. This shape is manufactured by pressing the crystal against a metallic ball, although the sensitivity in such a case is theoretically higher because there is no mismatch

¹PZT stands for Lead(Plumbum) Zirconium Titanate, which is the most commonly used material for ultrasonic detectors.

between glass and water. Nonetheless, it is difficult to manufacture such detectors, and they are prone to break and fracture, because of the thin layer of PZT used at high frequencies.

In our case we are using detectors based on a Lithium Niobate ($LiNbO_3$) crystal grown on glass or sapphire. This crystal is diced into the suitable size, and a concave lens is machined into the glass, this adds the focusing to the detector. Finally, the detector is connectorized, where the ground connector is connected to the outer surface of the crystal, and the signal connector is connected to the inner side of the crystal.

As for the detectors that use an acoustic lens, there are different kinds of such a lens. These lenses could be manufactured from glass, sapphire, or any other material that has a different speed of sound compared to water. Compared to sapphire, glass is better matched to water, thus has a better coupling efficiency. For example, the acoustic waves propagate inside water at a speed of 1500 m/s, while in glass they propagate at a speed of 5600 m/s, and inside sapphire they propagate at a speed of approximately 11000 m/s. On the other hand, the sapphire lens could be manufactured with a higher numerical aperture than the glass lens, this happens because the acoustic rays, bend much more inside sapphire, than they do inside glass, thus for the same active area, the acoustic focus could be placed closer to the surface of sapphire than it is to the surface of glass, thus achieving a lower $F_{\#}$, see section 2.4.3.

At low frequencies, the large area of the active element, might result in the propagation of undesired surface waves. Moreover, in many applications it is desirable to tailor the properties of the detector, such as the electric impedance, the acoustic impedance, and so on. To achieve this, piezo-composites were introduced; the piezo material is divided into smaller parts, between which an insulator is inserted. The amount of the insulator inserted depends on the desirable parameters that need to be achieved [37].

2. Capacitive micro-machined ultrasonic transducers: Another category of ultrasound

detectors that is catching up pretty fast are the capacitive micro-machined ultrasonic transducers (cMUTs). This technology has been introduced in the 1990's, and it uses the CMOS manufacturing technology for producing such detectors. This technology allows for high-density packaging, and the transducers have a wider bandwidth than traditional PZTs. Nonetheless, the reception sensitivity could be made higher than the sensitivity of PZT detectors, this is achieved by integrating amplifiers, and filters directly on the same CMOS chip as the cMUTs themselves [47–49].

3. Optical interferometry techniques: optical detection could be used as well, where interferometric detectors are used, such as Fabry-Perot interferometers [50, 51], and Bragg-gratings, either on fiber or silicon [52]. Also micro-ring resonators are used for ultrasound detection [53–55]. The benefit of optical detection is the possibility to miniaturize them without losing sensitivity. This capability enables the production of very small ultrasound detectors. With very high bandwidth, for instance the fibre Bragg grating (FBG) sensor has an equivalent active area of $10 \times 300 \mu m^2$ [56–58]. Such elements have much higher sensitivity compared to a PZT of the same size. Additional miniaturization could be achieved through the use of silicon photonics, where the interferometer is built on a silicon on insulator platform. Using such technology an active footprint of $0.5 \times 30 \mu m^2$ is achieved [52].
4. Optical deflection techniques: This category of ultrasound detectors is based on detecting the deflection of an optical beam from the surface of the object. That is a result of displacement and vibrations on the surface resulting from pressure. The deflection is measured using a quadrature detectors [59].

3.1.2 Low frequency detectors

Low-frequency detectors are very versatile, and any of the detection techniques previously mentioned for detecting ultrasound could be used. They cost efficient and have high sensitivity because of the large detection areas used in manufacturing those low-frequency detectors.

For low-frequency detection, the detectors could be manufactured in any possible shape. For example, curved detectors are used to focus the sensitivity field of the ultrasound detector. Moreover, arrays of ultrasonic detectors could be easily manufactured at low frequencies, making it possible to have real-time detection, and build realtime imaging systems.

3.1.3 High frequency detectors

For efficient detection of high frequencies, the dimensions of the detectors needs to be either smaller or an acoustic lens needs to be used. This size limitation is a direct result of acoustic diffraction, where smaller active areas are required, such that the detector can detect signals from different directions. High-frequency detectors are not as versatile as those designed for low frequencies since arrays of detectors are not so easy to manufacture anymore because of the smaller dimensions. This small size puts a lot of demand on the connectorization process. Thus, it is difficult to manufacture high-frequency arrays at frequencies above 25 MHz.

Alternatively there exist several manufacturers of spherically focused ultrasound detectors, mostly based on a piezoelectric crystal that is grown either on a glass or a sapphire wafer. Such detectors are mostly used in acoustic microscopy applications and have frequencies as high as 2 GHz.

Similar to low-frequency detectors, optical detection could be used for sensing optoacoustic signals; Fabry-Perot sensors have been used to detect signals as high as 39 MHz [50, 51]. They are small in size but have low sensitivity. Microring resonators can detect signals as high as 300 MHz, with good sensitivity, but their size of 50-60 μm limits their application in optical resolution optoacoustic microscopy [60]. Finally, Bragg-gratings on a silicon chip, are a promising candidate for the detection of high-frequency ultrasound. They can measure frequencies as high as 250 MHz; they have a small active area and good sensitivity, but unfortunately they are still not widely available for imaging applications [52].

Because of all this, we are using spherically focused ultrasonic detectors, based on a piezoelectric crystal.

3.2 Lasers

Lasers are an important component in many thermoacoustic systems, specifically those that use optical excitation, more commonly known as optoacoustics or photoacoustics. As there are books that discuss laser operation, we will be discussing only those aspects which are related to raster-scan optoacoustic mesoscopy (RSOM) [61].

The major requirements on a laser for RSOM are as follows:

1. Short pulse width: to excite the high frequencies necessary for generating high-resolution images, as well as to insure thermal and stress confinement conditions² a pulse width of $< 4 ns$ is needed [36,62], as can be seen in figure 3.2.

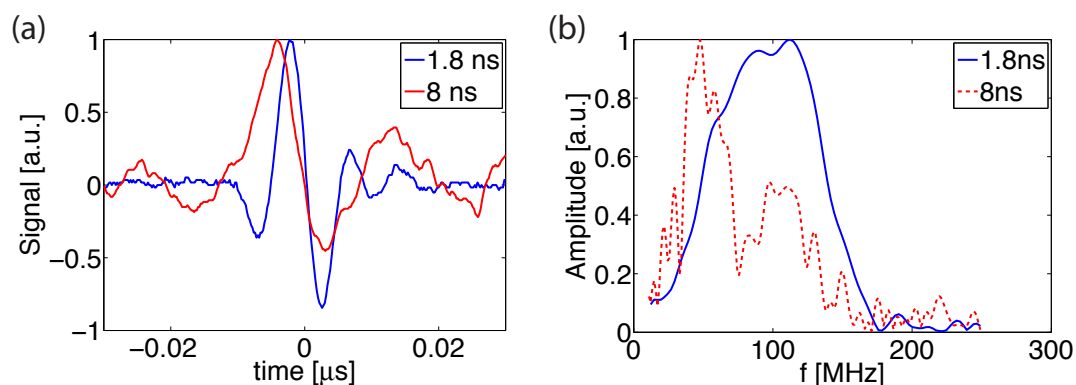


Figure 3.2: Optoacoustic signal generated from a $10 \mu m$ sphere: (a) time signals, (b) Fourier transform of the time signals.

2. High pulse energy: as in RSOM a big region of the sample is illuminated, relatively high pulse energies are required [40]. From our experience, energies of several hundreds of μJ are necessary for efficient excitation of the sample.
3. High repetition rate: because RSOM is based on scanning of a single element detector, the acquisition time is dependent on the repetition rate of the laser.
4. Excitation wavelength with maximum absorption: as high frequencies have lower amplitude than low frequencies. It is necessary to compensate this SNR with higher absorption from within the sample [40]. Looking at the absorption spectrum of biomolecules,

²Thermal and stress confinement were introduced in chapter 2.

such as haemoglobin, it is obvious that the absorption of haemoglobin in the green region is much higher than it is in the red region. Thus, using green generates stronger signals, see figure 2.2.

The lasers we use for RSOM are summarized below:

	Innolight	Bright Solutions
Wavelength	515 nm	532 nm
Max pulse repetition rate	1.4 kHz	2 kHz
Q-switching	Passive	Active
Pulse energy	570 μ J	1 mJ
Pulse width	1.8 ns	0.9 ns

Table 3.1: Lasers used for imaging in RSOM

In addition to the lasers mentioned in table 3.1, we have used a tunable laser with low repetition rate and long pulse width of 8 ns. This laser was used to show the necessity for a shorter pulse width. The output of this laser is tunable in the near-infrared range using an optical parametric oscillator (OPO) crystal.

3.3 Motorized stages

If an ultrasonic array is used, then real-time thermoacoustic imaging is possible. On the other hand, if a single element detector is used, then there is a need to scan this detector over the sample. This scan could be performed around the sample, as is the case for tomography, or it could be linearly above the sample, as is the case for raster-scan imaging. In both cases, the stage needs to be more accurate than the expected resolution; a factor of 10 is a good estimate.

For high resolution applications there is an even higher demand on precise stages, where the resolution of the stage encoder is important to achieve accurate positioning of the detector. Additionally, high-speed is necessary to achieve real-time or almost real-time imaging capabilities. This capability is necessary to be able to carry the detector, as well as all the cabling, and illumination as is the case for reflection mode RSOM. All of this is readily available in what is called piezo stages, such as those manufactured by PI (Physik

Instrumente GmbH, Karlsruhe, Germany). Such modern stages are capable as well of receiving, and transmitting trigger, and synchronization signals, which could be useful for several applications.

3.4 Data acquisition

	Tektronix 3054B	Gage CS12502	Gage CS121G2	ADQ412-3G
Interface	TCP/IP	PCI	PCI	PCIe-16x
Resolution	8 bits	12 bits	12 bits	12 bits
Max sampling rate	5 GSps	500 MSps	1 GSps	1.8 GSps
Multirecord support	No	Yes	Yes	Yes

Table 3.2: Comparison between the different data acquisition systems used throughout the dissertation.

Data acquisition is the last step in every measurement. This step is where the analog signals are digitized, and stored in a form that can be processed later. Requirements on data acquisition include the following:

1. High sampling rate: this is important for digitizing high frequencies. Although the Nyquist criterion requires that the sampling rate is twice the highest detectable frequency. In order to get a good representation of the signal, it is important to have a sampling rate 5-10 times higher than the highest frequency.
2. High resolution: this factor in combination with amplification determines the possible dynamic range of the system, the higher the number of bits per sample, the better.
3. High data transfer rate: this factor describes the speed with which the acquired samples are transferred to the computer. Common methods transfer data over TCP/IP link, PCI interfaces, and PCI/e interfaces. The need for faster data transfer rates becomes more apparent where high amounts of data are present, such as in the case of raster-scan optoacoustic mesoscopy (RSOM) imaging, see chapter 5.

In the development of the different imaging systems, we have used various data acquisition devices. Each one has its advantages. First, we used an oscilloscope connected through

a TCP/IP link, which is versatile, but slow, and has a bad resolution, then a PCI card, which is also versatile, but has some limitations in terms of data transfer, and finally a PCI/e card which is less versatile, but has a high acquisition speed, and a high data transfer rate.

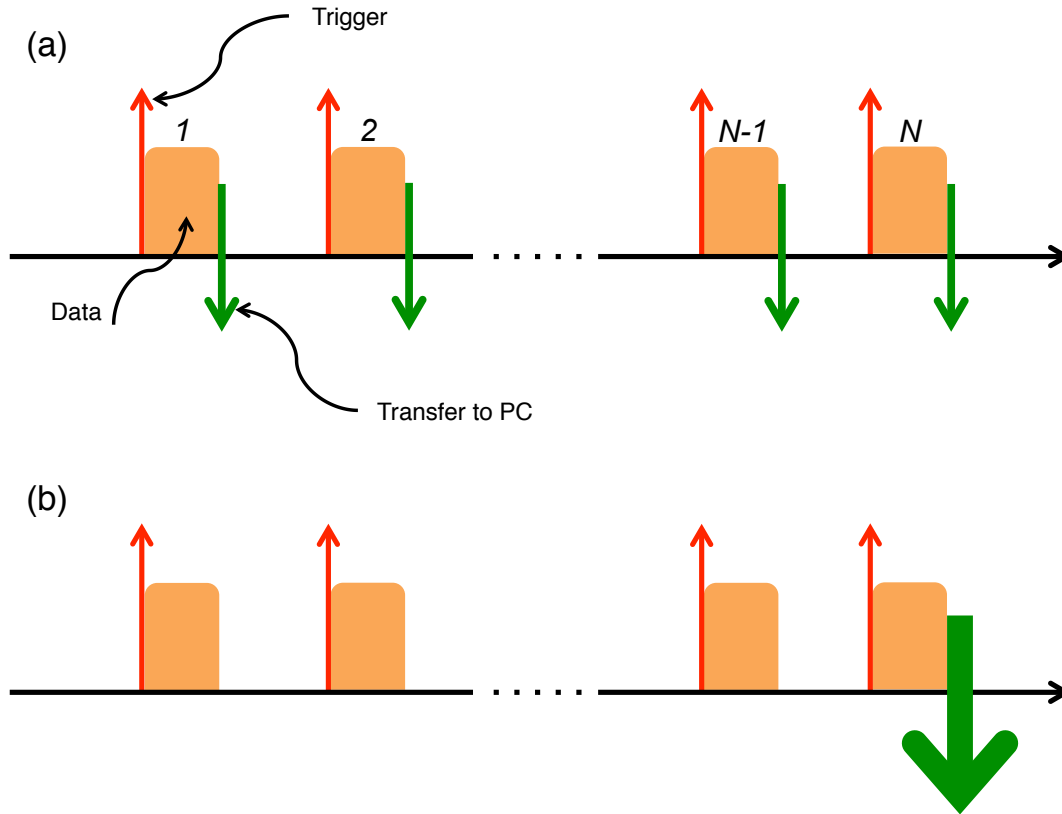


Figure 3.3: Trigger options: (a) single mode, where after every trigger event the data is transferred to the PC, (b) multi-record mode, the data acquisition system acquires a certain number of trigger events, then transfers them all together to the PC.

As for data transfer from the data acquisition system to the PC, whether it is an oscilloscope or a built in card, there are two major methods for this. Either single trigger data transfer, where the measured data is transferred to a computer after each trigger. This method is the most straightforward way, but it is relatively slow, with a maximum transfer rate of measurements of 2 kHz. The other method being multi-record transfer, where the card acquires a certain amount of events, and then transfers them all at once to the computer. As this method doesn't require continuous communication between the card and the computer, it achieves higher transfer rates, as high as several kHz, to hundreds of kHz. Nonetheless, it is more complicated to implement, and to synchronize than the single trig-

ger method.

Table 3.2 shows a comparison of the different acquisition systems that we used during the dissertation.

3.5 Parallel processing

Because of the large amount of data generated in raster-scan optoacoustic mesoscopy (RSOM), and the use of three-dimensional reconstruction, it would take several weeks to reconstruct an image on a computer. As the processes for reconstruction applied on one projection are identical to the processes applied on the other projections, this problem can be highly parallelized. To do this in the most efficient way, we are using graphical processing units (GPU) for reconstruction³.

GPUs contain a certain amount of memory, usually 2-4 GB of random access memory, and many hundreds of processing units, or cores, usually 1000-3000 cores. This number means that several projections can be processed simultaneously on a GPU. Compared to a central processing unit (CPU) of a computer, such a unit usually has 2-8 processing units. Thus, a GPU offers 2-3 orders of magnitude higher parallelization than what is possible on a CPU.

The programming of these GPUs is done either through the OpenCL interface, which is a general purpose programming language for GPUs, or through CUDA, which is a programming language developed for Nvidia GPUs.

What drives the development for such GPUs is the gaming market. Following the trends in the last years; increasing the number of cores in every generation of GPUs, which follows Moore's law. We expect even faster GPUs, with more parallel cores in the near future. This growth will enable us to accelerate our code by another 1-2 orders of magnitude.

³At the beginning we had the core of the GPU code implemented in OpenCL from iThera Medical GmbH, later Mathias Schwarz implemented a newer and faster version which is currently in use.

3.6 Outlook and conclusions

Technology as we have seen in this chapter plays a central role in the progress of thermoacoustic imaging. The better this technology becomes, the better the images that we will get, and the better, as well, our understanding of biological processes. Several key breakthroughs in the last two decades have enabled the imaging technologies that we are using today. First, advancements in ultrasonic detection, in its sensitivity, and in its ability to reliably measure high-frequency ultrasound. Although ultrasound detectors have been around for many years, the current levels of sensitivity are much better than what was possible 20 years ago. This sensitivity enables us to use lower laser energies in for optical thermoacoustic excitation.

Another important advancement was in the availability of fast, high-repetition rate, ns-lasers; these lasers have now enough energy to excite a high enough thermoacoustic signal that could be measured with current ultrasonic detectors. The pulse widths used are short enough to excite the high frequencies that we can measure with our high-frequency detectors [36]. And the repetition rate is high enough to enable measurements within several minutes, rather than waiting for hours.

In the future, we expect the technology to develop along two lines: we expect the detection technology to improve, providing smaller, more sensitive, and even paralleled detection schemes. This advancement will improve the signal to noise ratio of the images, increase the measurement speed, provide wider angular coverage, and become more applicable in situations where the current detection technology fails. The other direction is the development of less expensive, fast, tunable ns-lasers, with higher repetition rates. Such lasers will enable faster measurements. They will be possible a wider range of applications, and the tunability will increase the detection sensitivity of certain molecular agents or disease biomarkers. Thus, enabling multispectral, or multicolor, imaging of bio-samples. As well as going to higher wavelengths, into the red, or near infrared. These wavelengths will enable imaging at higher depths, currently not possible due to the limited penetration depth of green light. Moreover, such tunable lasers can enable the imaging of several molecules at the same time, such as oxy- and deoxy- haemoglobin. These measurements in turn can

elucidate information about the current physiological status of a certain organ, and whether there is any abnormal activity there.

Chapter 4

Near-field Radio-frequency

Thermoacoustics (NRT)

4.1 Earlier work

The idea of using radio-waves to image biological tissues using the thermoacoustic effect goes back to 1981. Then Theodore Bowen suggested the use of electromagnetic waves to generate temperature transients, and subsequently measure the generated thermoacoustic waves using ultrasonic detectors [14]. Unfortunately, this took until 1999 to be realized. Then Robert Kruger used a radio-frequency (RF) amplifier that generated pulse modulated, high power, RF signals at a frequency of 434 MHz [63]. He used these pulses to image an excised lamb kidney; the nice thing about this setup was the use of a hemispherical ultrasonic array which is suitable for imaging of the breast. The same year, Lihong Wang generated RF-thermoacoustic signals, this time using a microwave generator operating at a frequency of 3 GHz [16]. Using his system he imaged some extracted biological tissue, mostly fat, and muscle tissue formed into different shapes.

A drawback of using RF or microwave amplifiers to generate the thermoacoustic signals is the relatively long pulse width of those amplifiers. To irradiate with enough energy, pulses with durations longer than 500 ns are used. Consequently, the attained resolution is limited to around 1 mm, which is not sufficient for most applications.

To overcome this limitation, posed by the pulse width, our group has introduced in 2010 the concept of near-field radio-frequency thermoacoustics tomography (NRT) [64]. Where instead of using a high-frequency, high-power RF amplifier, broad-band, high energy pulses are used. These pulses could be as short as 10 ns [18], and have energies as much as 1 J. As they are much shorter than what is used in other systems, it is possible to get higher resolution images.

In its first version, the system used a dipole antenna to couple the energy from the pulse generator to the sample, and was used to image a wire, and some other phantoms [64]. Later the system was upgraded with a helix antenna which coupled more energy to the sample, and was used in this form to image a mouse *ex-vivo*. Characterization of the system using two wires crossing revealed a resolution on the range of 150 μm [65]. A further improvement of the system was based on using transmission lines instead of a simple high voltage capacitor for generating the pulses. The advantage of doing this using transmission lines instead of a simple capacitor, is the possibility to decouple the energy stored inside the transmission line from the width of the pulse generated as we will see later in this chapter. This system was used to image mice *ex-vivo*, and achieved pulse durations as short as 10 ns. Using such pulses a resolution of 45 μm is achieved [18].

At a later stage the concept was replicated by another group [66, 67]. Moreover, we have also introduced the concept of quasi-continuous wave thermoacoustic imaging [68], and see section 4.5.

4.2 System description

4.2.1 Equipment and characteristics

Besides the impulse generator, which we will discuss in section 4.3, other equipment was used as well, these include an ultrasonic detector. This was mainly a 3.5 MHz cylindrically focused, ultrasound detector (V382, Olympus-NDT), and a 15 MHz cylindrically focused, ultrasound detector (V319, Olympus-NDT), this detector was used to characterize the resolution of the system.

Due to diffraction the generated RF-thermoacoustic signals are not confined, but rather spread all over the water tank. Because of this the amount of energy that is used to excite the thermoacoustic signals is much lower than what is traditionally used in optical thermoacoustics. To be able to measure the signals, a low noise amplifier is used to bring the signals into the dynamic range of the data acquisition system (63 dB, model AU-1291, Miteq Inc., U.S.A). After amplification of the signals, they are digitized using an oscilloscope that is remotely connected to a personal computer (PC) for synchronization between the acquisition and the measurement position. The oscilloscope is controlled from Matlab through a TCP/IP connection. After every acquisition, the sample is moved to the next position, this is facilitated using a rotation stage, and after a section is acquired the sample is translated to the next z-level using a translational stage. All of this is synchronized using a PC.

4.2.2 RF interference and system isolation

Because of the high energies generated in the system, a single pulse is enough to interfere with other electronic devices around, such as the ethernet router, the mouse, and the keyboard in the system. To minimize these interferences the system needs to be properly grounded and isolated from the surrounding environment. For this reason the system is placed in a grounded aluminum box, which serves as a Faraday cage, and minimizes the interferences escaping from the system through direct radiation. Moreover all the cables carrying trigger signals, control signals to the stages, and the generated thermoacoustic signals needs to be properly shielded and grounded. This shielding could be achieved by covering them with an electronic sheath. Experience have shown that when all this is not properly done huge electromagnetic interference is seen from the system.

4.3 Impulse generator

4.3.1 Basics of impulse generation

The basic idea behind high voltage impulse generators is the slow storage of the energy in the energy storing element and the subsequent fast discharge of this energy. The charging is usually done using a high voltage DC source, and the discharge is usually performed using a fast, high voltage switch, see figure 4.1.

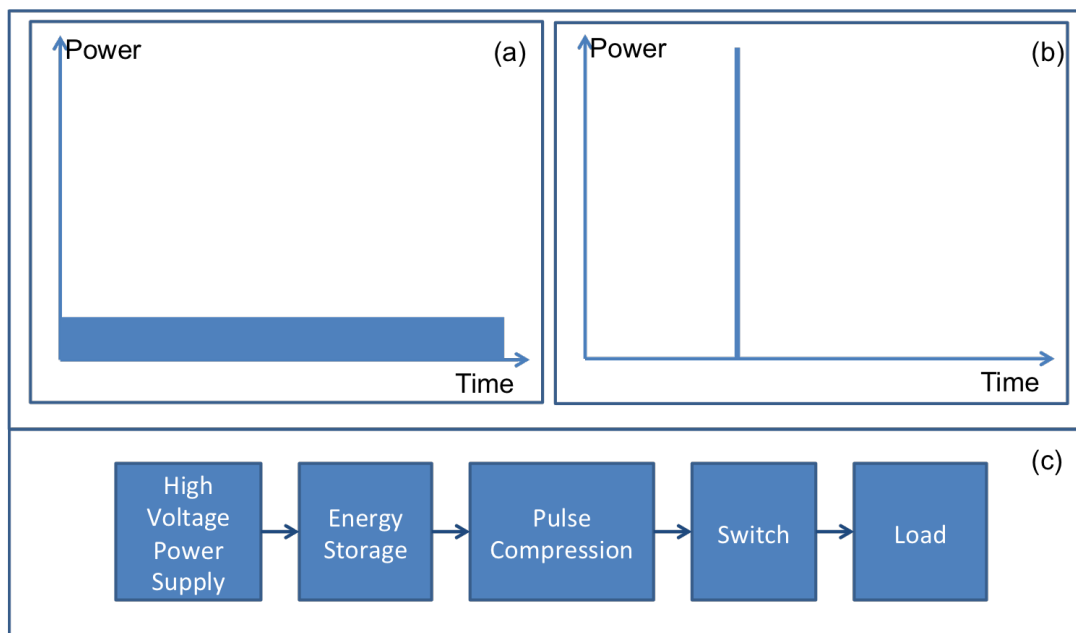


Figure 4.1: (a) Energy is steadily stored into an energy storing element, (b) the release of the energy happens very fast, (c) schematic of the pulse generation.

There are many basic designs of a pulse generator [69]:

1. Capacitor based impulse generators.
2. Pulse forming lines (PFL).
3. Blumline impulse generator.
4. Marx-bank.

For fast switching several possibilities are available, spark gaps, and solid state circuits such as avalanche transistors and diodes are the most popular [70]. The spark gap is a chamber full with gas, by triggering the spark gap an ionization process of the gas inside

starts. This process decreases the break-down voltage inside the spark-gap, by this if there is enough voltage difference between the cathode and the anode then a circuit closes, and a pulse is generated.

4.3.2 Capacitive impulse generators

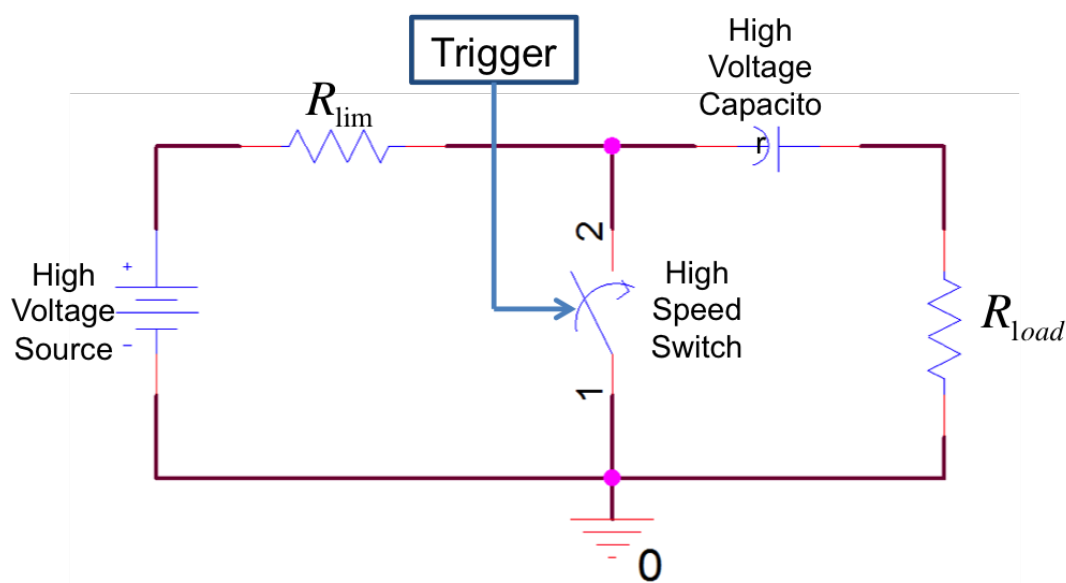


Figure 4.2: Schematic of the capacitive impulse generation circuit.

Capacitive impulse generators are the basic form of impulse generation, as a matter of fact other impulse generators are a variation on it. In the capacitive impulse generator, see figure 4.7, a capacitor, C , is slowly charged from a high voltage source through a large resistor R_{lim} . Afterward using a fast high voltage switch the capacitor is discharged through the load, R_{load} . Both the charging and the discharging are exponential procedures, with a characteristic time τ_{pulse} given by:

$$\tau_{pulse} = R_{load}C, \quad (4.1)$$

this time is also the time needed for the capacitor to discharge 63% of its energy; it is on the order of tens of nanoseconds. Charging, on the other hand, is a slow process, with

a charging time τ_{charge} defined by the following:

$$\tau_{charge} = R_{limit}C, \quad (4.2)$$

this τ_{charge} is the time needed for the capacitor to charge to 63% of its energy, usually this time is on the order of milliseconds. Eventually, this time is what defines the maximum pulse repetition rate.

For proper pulse generation, the discharge time needs to be much smaller than the charging time. This implies that $R_{lim} \gg R_{load}$. Usually, the charging resistor is on the order of 50 M Ω , while the discharge resistor is on the order of 50 Ω . The major benefit of capacitive pulse generators is their simplicity, where a simple high voltage capacitor is enough. On the other hand these impulse generators have a big disadvantage when it comes to controlling the pulse width, especially when this needs to be done without sacrificing the energy of the pulse. The total energy generated in this impulse generator is given by:

$$E_0 = \frac{CV^2}{2}, \quad (4.3)$$

where V is the voltage that charged the capacitor.

4.3.3 Pulse forming lines (PFL)

Pulse forming lines (PFL) are often used in impulse generators to overcome the limitations of traditional capacitor based impulse generators. A major limitation is inability to control the pulse width and the pulse energy separately. To solve this limitation, transmission lines could be used. Transmission lines, or pulse forming lines have the capability to decouple the pulse width from the pulse energy. Where the pulse width is related to the length of the line ℓ_{line} according to the following equation:

$$\tau_{pulse} = \frac{2\ell_{line}}{c}, \quad (4.4)$$

where c is the speed of propagation of an electromagnetic wave inside the pulse forming line, see figure 4.3.

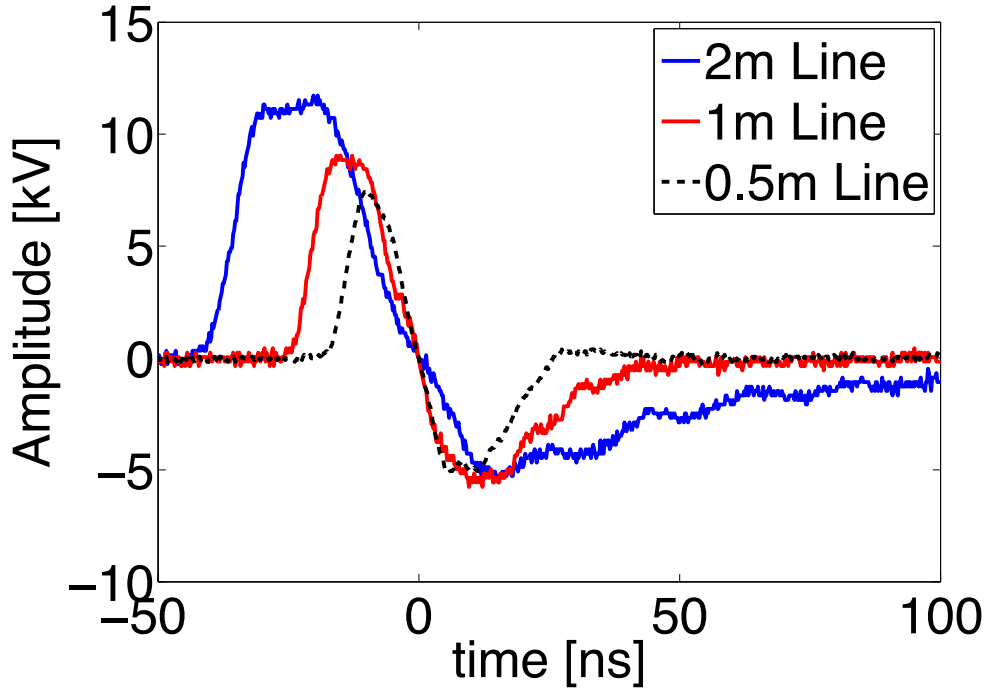


Figure 4.3: Comparison between the length of the transmission line and the width of the pulse.

On the other hand, the stored energy in the PFL is:

$$E_0 = \frac{\ell C_0 V^2}{2}, \quad (4.5)$$

where C_0 is the capacitance per unit length, and V is the charging voltage. Although from (4.4) and (4.5) both the pulse duration and the pulse energy depend on the length of the transmission line ℓ . The pulse energy could be increased by adding several such lines in parallel, for example, when N lines are connected in parallel, the total energy is given by:

$$E_{total} = N E_0. \quad (4.6)$$

Using this relation, the total energy of the impulse could be decoupled from the width of the pulse, this makes the transmission lines very attractive for impulse generation. It is worth

mentioning that the pulse amplitude is half the charging voltage.

The PFL can take several forms; any transmission lines can do the job. To this end coaxial cables have been mostly used for this. In this work a coaxial cable was used to generate a high voltage pulse, which was subsequently used to excite the biological samples. A schematic of the pulse forming line circuit is shown in figure 4.4.

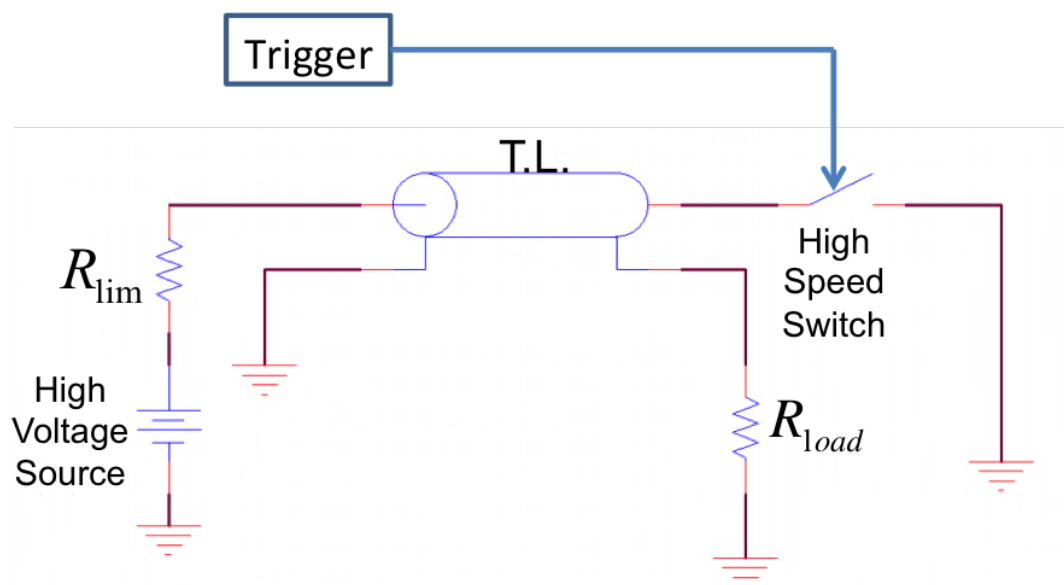


Figure 4.4: Schematic of the pulse forming line circuit, showing the charging circuit and the coupling circuit.

4.3.4 Other methods

Other methods for impulse generation exist as well, such methods include the Marx bank and the blumline impulse generator. The Marx bank is a variation on the traditional capacitive impulse generator, where several switches and several capacitors are used. These capacitors are charged in parallel, and discharged in series, because of this small charging voltages could be used to generate a much higher output voltage at the output [69].

The blumline, on the other hand, is a variation on the PFL, where two transmission lines are charged in parallel, and discharged in series. This configuration generates a much higher voltage than what an individual transmission line can do.

4.3.5 Improving the switching times

As previously mentioned, one of the problems with the switching is the spark gap, which is a bulky element, and cannot generate pulses with a fast rise time. To overcome this, it is possible to use avalanche transistors.

Avalanche transistors are normal transistors that operate in the avalanche mode, several of them are connected in series, a voltage V_c is applied across all of them together. If the breakdown voltage of a single transistor is V_b , then the applied voltage should satisfy the following inequality:

$$NV_b > V_c > (N - 1)V_b, \quad (4.7)$$

where N is the number of transistors connected in series. By switching one of them, the applied voltage V_c becomes larger than the total break-down voltage of the remaining transistors, thus switching large voltages in a very short time. Usually on the order of 1 ns, or even less. The switch is based on off the shelf transistors such as the 2N5551 and the 2N5550, and in the impulse generator circuit used instead of the spark gap. Unfortunately, satisfying results were not achieved with this switch, as:

1. The pulse broadens with higher voltage.
2. The pulse doesn't trigger in a reliable way.
3. The transistors don't survive more than several hundreds or thousands of pulses.

For these reasons, we decided to stay with the spark gap.

4.4 Results and imaging

4.4.1 Choice of imaging parameters

The parameters that play the main role in deciding the mode of operation:

1. The signal to noise ratio (SNR): this is proportional to the number of the projections N_{proj} , and the number of averages N_{avg} .

2. The acquisition time t_{acq} : this decreases with N_{proj} , and N_{avg} .
3. Artifacts, especially strike artifacts: this decreases with N_{proj} .

The basic modes of operation are continuous acquisition, where the sample continuously rotates from $0 - 360^\circ$, here $N_{avg} = 1$, and N_{proj} is proportional to the rotation speed, and the triggering rate, or the pulse repetition frequency f_{pulse} :

$$N_{proj} = \frac{360^\circ f_{pulse}}{\omega}, \quad (4.8)$$

where ω is the rotation speed of the sample in degrees per second. The second mode of operation is the discrete mode, where the sample is moved from one angular position to the other, this happens at steps of $\Delta\phi$, thus the number of projections in this case is equal to:

$$N_{proj} = \frac{360^\circ}{\Delta\phi}, \quad (4.9)$$

although this mode is slower than the continuous acquisition mode, it allows for averaging at every position, this increases the SNR by a factor of $\sqrt{N_{avg}}$. For the measurements using the thermoacoustic tomography system we settled on the discrete mode, with $\Delta\phi = 2^\circ$, and $N_{avg} = 16$, most of the experiments were also done using a 3.5 MHz cylindrically focused transducer. A schematic of the setup is shown in figure 4.5.

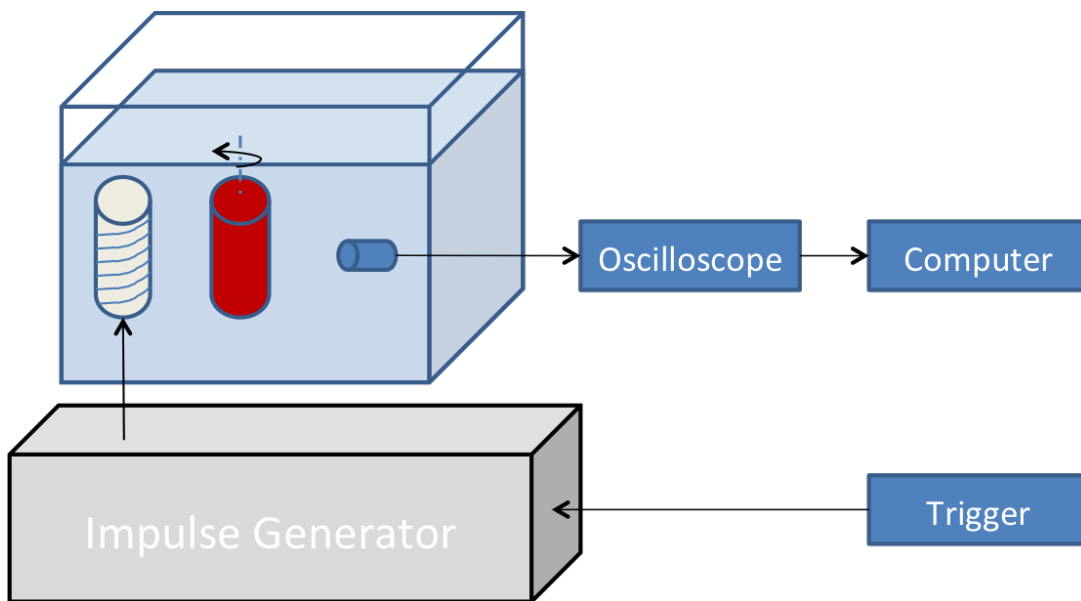


Figure 4.5: Schematic of the setup, both the excitation and the acquisition are shown.

4.4.2 Imaging of phantoms

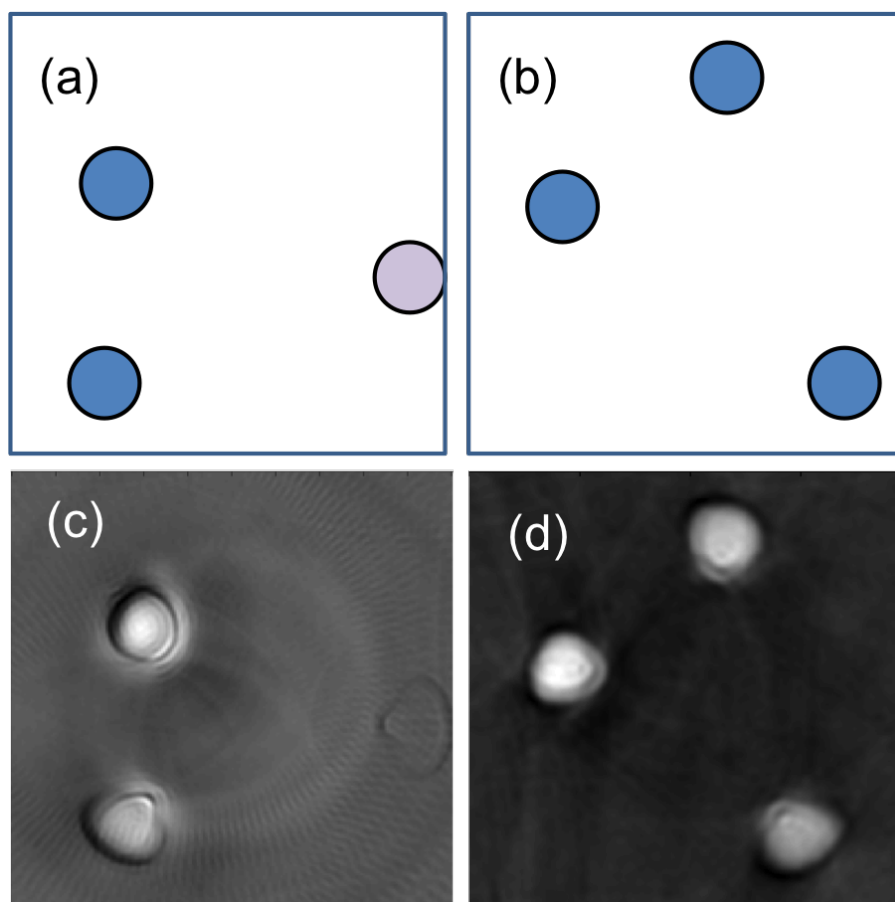


Figure 4.6: Comparison of the signals generated from saline tubes (blue circles), and tubes filled with de-ionized water (violet circles).

We have used phantoms to characterize the system resolution, and to characterize the contrast generated from different materials. For resolution characterization, we used a copper wire that has a diameter of $50 \mu\text{m}$. Such a wire induces a very strong thermoacoustic signal when excited with a short pulse; the reason for this are the high currents that pass inside the wire due to the high electric field present. For this characterization a transmission line that has a length of 0.5 m was used, as seen in section 4.3.3 such a transmission line generates a pulse of duration 10 ns, to match this with detection a detector that has a center frequency of 15 MHz was used. Moreover, to decrease the stray capacitance between the coupling element (the antenna), and the surroundings the helical element was replaced with another element that has a shorter total length, and is placed much closer to the phantom. After deconvolution with the wire geometry, the resulting FWHM of the wire

profile is $45\ \mu\text{m}$. Further, we imaged some plastic tubes filled both with de-ionized water and biological saline, to monitor how does the system differentiate between the different kinds of biological tissues. Saline solutions represent highly conductive tissue, such as blood, and muscles. De-ionized water solutions, on the other hand, represent fatty tissues. As seen in figure 4.6, the saline gives a strong signal, while the tube with de-ionized water is almost invisible on the image. This measurement was done using a 3.5 MHz cylindrically focused transducer, and the pulse generation was done using three 2 m transmission lines connected in parallel for increased energy.

4.4.3 *Ex-vivo* imaging of small animals

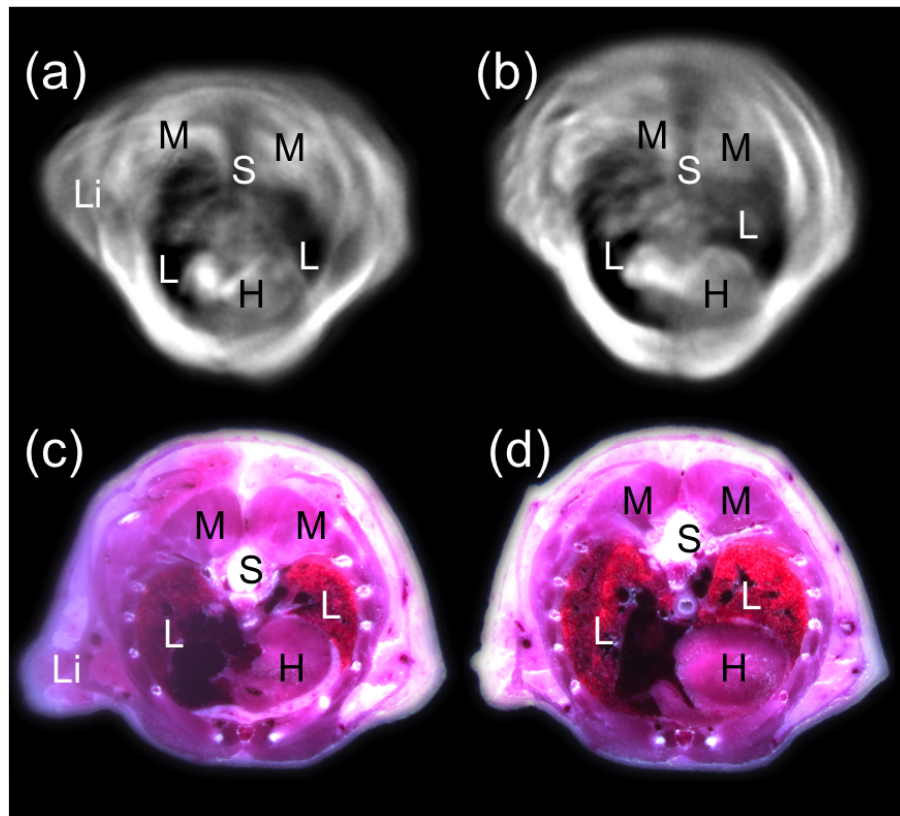


Figure 4.7: Tomographic thermoacoustic images of a mouse from the thorax region: (a&b) thermoacoustic images, (c&d) corresponding cryoslices; (M) muscles, (S) spinal cord, (L) lungs, (H) heart, (Li) limbs.

After characterizing the system, we decided to image some biological samples, the simplest of all was *ex-vivo* mice, before imaging, we shaved the mice in the thorax and abdomen region. After doing a full tomography, the detector was manually moved to the next *z-level*.

Finally, following the experiments the mouse was frozen to $-80C^\circ$, and then cryosliced, the resulting cryoslices were used to compare the generated thermoacoustic images with the anatomy of the mouse.

For comparison, we took two images from the stack, from the thorax region. On them the following organs are seen: the heart, the muscles in the back of the mouse, the ribs, the spinal cord, and the lungs. In the case of the lungs they are observed because of the mismatch in the speed of sound between soft tissue and air. We can see the same organs on the cryoslices.

4.5 Other modes of RF excitation

As mentioned in section 2.1, the generated thermoacoustic signal is proportional to the applied signal. In such a case if the applied signal is a delta pulse then we get the traditional N-shaped response. On the other hand if the excitation pulse is a sinusoidal, or a decaying sinusoidal then the result will have the same form but at double the frequency [68]. The system used for the experiments is depicted in figure 4.8.

This result could be derived starting from the thermoacoustic response (2.13), which is repeated here for convenience:

$$p(\mathbf{r}, t) = \frac{\beta}{4\pi C_V} \int_{\mathbf{r}'} \int_{t'} \frac{\delta(\mathbf{r} - \mathbf{r}', t - t')}{|\mathbf{r} - \mathbf{r}'|} \frac{\partial H(\mathbf{r}', t')}{\partial t'} dt' d\mathbf{r}', \quad (4.10)$$

separating the temporal and the spatial parts of the heating function $H(\mathbf{r}, t)$, as was done in section 2.2 we get the following:

$$p(\mathbf{r}, t) = \frac{\beta}{4\pi C_V} \int_{\mathbf{r}'} \int_{t'} \frac{\delta(\mathbf{r} - \mathbf{r}', t - t')}{|\mathbf{r} - \mathbf{r}'|} H_r(\mathbf{r}') \frac{\partial H_t(t')}{\partial t'} dt' d\mathbf{r}', \quad (4.11)$$

where the temporal heating function $H_t(t)$ represents the excitation source, for the case of thermoacoustics, and frequencies less than 100 MHz this is given by (2.18). Assuming that the excitation source is a continuous wave, at frequency f then the electric field E will

have the following form:

$$\mathbf{E} = \mathbf{E}_0 \sin(2\pi ft). \quad (4.12)$$

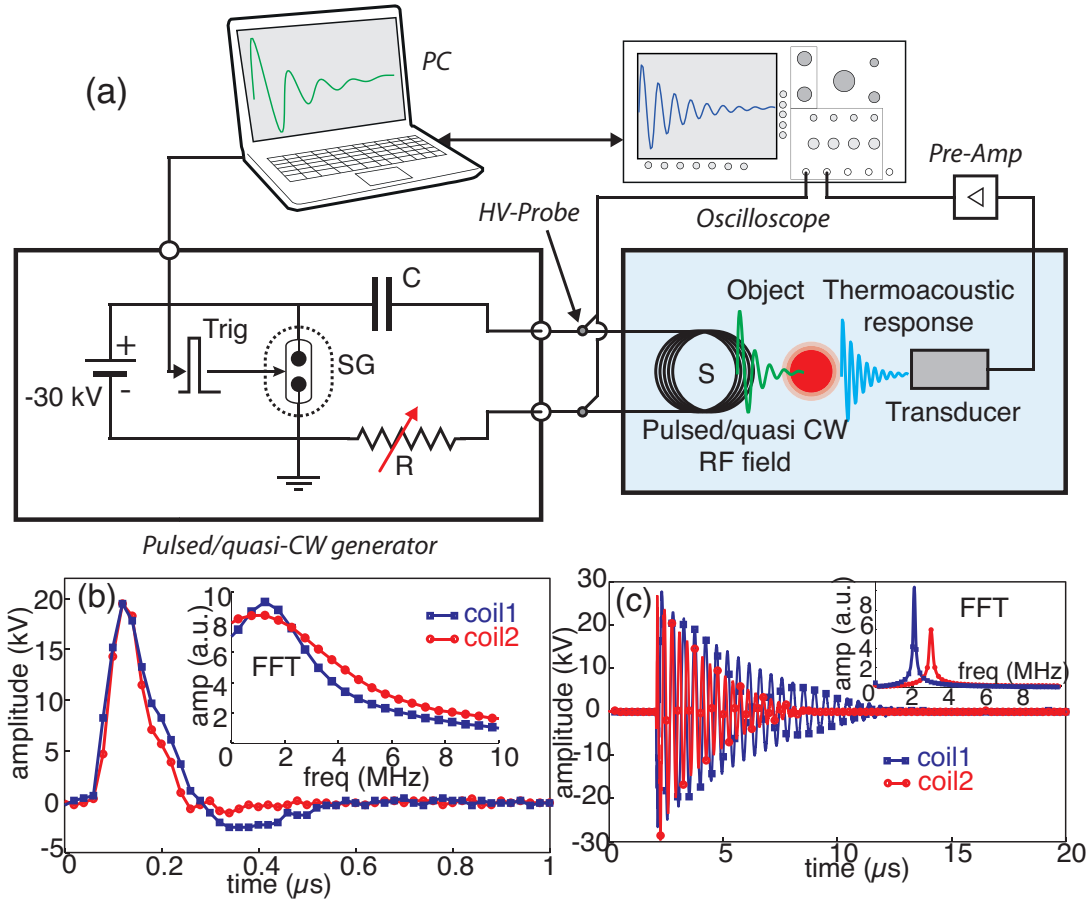


Figure 4.8: Schematic, and comparison between the signals generated using the pulsed mode and the quasi CW mode of excitations.

In the case of (4.12) the heating function becomes:

$$H(\mathbf{r}, t) = \sigma(\mathbf{r}) E_0^2 \sin(2\pi ft)^2, \quad (4.13)$$

By using trigonometric identities (4.13) becomes:

$$H(\mathbf{r}, t) = \sigma(\mathbf{r}) E_0^2 \frac{1 - \cos(2\pi(2f)t)}{2}, \quad (4.14)$$

this result established the origin of the second harmonic generation in RF thermoacoustics when excited with a continuous wave (CW) or a quasi-CW field [68].

4.6 Discussion and outlook

In this chapter we have described a system capable of imaging the electrical properties of biological tissues, with resolutions reaching tens of microns. Considering that the wavelength of the excitation pulse used is on the order of tens of meters, such a resolution is on the order of $\lambda/1000$. Which is unprecedented for imaging of electromagnetic properties of biological tissues before!

Such a system is based on a house made impulse generator, which is coupled to a helical antenna, this antenna couples the electrical pulse to the sample in its near field. The impulse generator is based on transmission lines, which enabled us to decouple the width of the pulse, from the energy inside the pulse, see section 4.3.3. And pulse widths of 10 ns were achieved, approaching the width of the pulse of lasers used in optical thermoacoustic imaging, thus achieving similar resolutions.

Using the system we have been able to image mice *ex-vivo*. From the reconstructed images we were able to see the skin of the mouse, the muscles, the heart, the lungs, the intestines, the ribs, the spine, and the forelimbs. Where the contrast comes from the conductivity of the tissues, in such a case muscles have more conductivity, thus have a higher contrast than fat, for example, see section 4.4.3.

Besides building the system we also investigated the characteristics of the systems, we have seen the capability of the system in generating pulse widths as small as 10 ns, and achieves resolutions as high as 45 μm .

We also investigated the generation of second harmonics in thermoacoustics, this happens when a CW excitation, or a quasi CW excitation is applied. In such cases the generated frequencies inside of biological tissues are at double the excitation frequency, see section 4.5.

As was previously stated RF-thermoacoustics combines the high contrast of RF absorption for biological tissues [1, 29, 30], combined with high resolution, and the low scattering of ultrasonic waves in soft biological tissues. Thus, it is possible to achieve both high resolution and high contrast imaging inside biological tissues. Compared with optical thermoacoustic imaging, which we will be discussing in chapter 5, RF thermoacoustics offers higher

penetration depth of excitation. Thus, the possibility for application in clinical situations where optical thermoacoustics would only offer a penetration depth of 2-3 cm, additionally the large wavelength of RF thermoacoustics offers homogeneous excitation of the sample compared to other methods.

To make thermoacoustics available for a wider community, and later in the clinics some problems need to be solved. Major problems include a low energy density in RF thermoacoustics; this is in part due to the inability to focus RF waves to a small spot. Thus, certain advances in the detection of thermoacoustic waves need to be done. Such as increasing the sensitivity of detection, by using better detectors.

Additionally to enable real-time imaging using RF-thermoacoustics, which is essential for imaging animals *in vivo*, and later patients in the clinics, it is essential to have the capability of real-time imaging. Such capabilities can enable real-time and dynamic monitoring of quantities of interest, and reduce motion artifacts, especially when done in the clinics. To do this the system needs to be redesigned, this includes adding an ultrasound array, well shielded against electromagnetic interference, as well as an amplifier bank to amplify the weak thermoacoustic signals, and parallel data acquisition.

Another problem that needs to be solved is the interference of excitation with PZT based ultrasonic detection, the current detectors are based on the piezoelectric effect. Which is prone to electromagnetic interference, methods not based on the piezoelectric effect, but based on optical interference for instance need to be further advanced [52, 56–58].

If RF thermoacoustics manages to solve these problems, then we should expect a strong method that can complement medical ultrasound, MRI, and other modalities currently used in clinical and pre-clinical research.

Chapter 5

Raster-scan Optoacoustic Mesoscopy

In this chapter, we will be discussing high-resolution optical thermoacoustics, in this chapter, and in the following one, chapter 6, we will simply call it optoacoustics.

5.1 Introduction

In the last decade the research in optoacoustic imaging has soared, only in the year 2013 alone more than 800 papers were published in this area. Several reasons played a role in the explosion of the field of optoacoustics. These include the sensitivity of the optical absorption to both endogenous contrast, such as blood, both oxy, and deoxy, as well as the ability to detect exogenous contrast with high sensitivity as well, see figure 2.2. Moreover, because in optoacoustics the detection happens through ultrasound, it is possible to image optical contrast much deeper inside the tissue than what is possible with optical microscopy techniques. Thus, fine acoustic resolution is achievable at depths beyond the optical diffusion limit [13]. Technological advancements in both laser technology and detection technology have enabled faster, more sensitive, and cheaper systems as well. All this led to the explosion of the field of biomedical optoacoustic imaging.

Applications of optoacoustics vary, and include depending on the configuration used both clinical applications [71–73], and pre-clinical research where optoacoustics is used to study different disease models. In both these systems, and the systems used for clinical applications, high penetration depth of several centimeters is achieved at a resolution of 100-

300 μm . On the other hand optoacoustics has found its way into microscopic applications, where either high-frequency, spherically focused ultrasonic detectors are used, or the laser beam is focused into a tight spot, and the generated ultrasound is measured by a detector that is usually confocal to the optical focus. In both cases to generate the final image, either the acoustic or the optical focus is raster scanned throughout the sample. In the case of acoustic focusing, the achieved resolution is dependent on the properties of the detectors used. For example a 50 MHz detector, has a resolution of 40 μm laterally, and 15 μm axially. While in the case of optical focusing this would be around 1-5 μm laterally and 15 μm axially as well. In both cases the axial resolution is dependent on the reception bandwidth of the acoustic detection, see chapter 2. Moreover, hybrid systems, where the resolution is a combination of optical focusing, that blends slowly into acoustic focusing have also been recently introduced [74].

Although these systems both acoustic resolution and optical resolution cover a large area of applications, there is still a need for a system that achieves a higher resolution than the acoustic resolution systems in use, and at the same time capable of imaging deeper inside biological tissues than what is currently possible using optical microscopic systems. Such a system would be used to image samples that range in diameter from 500 μm to 5 mm. This range is where microscopy is cannot reach, and tomography is still irrelevant. Because of this we call it Mesoscopy, there this refers to the system imaging in the range between microscopy and macroscopy. This range includes, but not limited to, skin diseases, tumor development and tumor angiogenesis, imaging of the development of model organisms such as the zebrafish, the *Xenopus*, and the *Drosophila Melanogaster*, and finally imaging of cells deep inside the tissue.

Although mesoscopy have been previously introduced, for example tomographic fluorescence imaging [75], and mesoscopic optical projection tomography [76], those two systems are only suitable for imaging of very small animals like *Drosophila melanogaster*, and at a relatively low resolution. Optical coherence tomography, and optical frequency domain imaging [77], can generate high resolution imaging of biological tissue, but it is limited in

contrast, and it can image up to 1 mm of depth only, afterwards it suffers from light diffusion as well, while for most applications several millimeters are needed. Because of all this a new, mesoscopic system is needed. Additionally, having a mesoscopic optoacoustic system, will give the possibility to do multi-scale optoacoustic imaging, and thus gain from the rich contrast provided by optical absorption at the different scales of imaging.

5.2 Design of a high-resolution system

5.2.1 Ultrasonic detection

As was mentioned in section 5.1, our goal is to develop a high-resolution system, capable of delivering images at depths beyond what microscopic system can achieve, and at a resolution higher than what current acoustic resolution systems can achieve. For this reason, we decided to do acoustic resolution, but at higher frequencies, to push the resolution. Thus, we chose a detector with a center frequency above 50 MHz. To get the best sensitivity, we decided to use spherically focused detectors with an $F_{\#} \cong 1$, this way we increase the sensitivity inside the focus, as well as the angular coverage outside of the focus. Although point detectors at high frequencies exist, they suffer from low sensitivity, where the sensitivity of an ultrasonic detector is usually proportional to the area of the active element [37, 40]. For more information about ultrasonic detection, and the different possibilities for detecting ultrasound, please refer to chapter 3.

5.2.2 Laser source

For excitation we used several sources, see chapter 3, at the moment we are using a diode pumped solid state laser (DPSS) operating at 532 nm, 2 kHz repetition rate, 0.9 ns pulses, with an energy of 1 mJ per pulse (Bright solutions SRL, Pavia, Italy), for more about lasers please refer to chapter 3.

5.2.3 Data acquisition

Currently we are using a 4 channel high speed data acquisition card (ADQ-412-3G, Signal Processing Devices Sweden AB, Sweden), for comparison with other cards, and to read more please refer to chapter 3.

5.2.4 Scanning

There are many possibilities for scanning the transducer, the simplest one of them is mechanical scanning. Here motorized stages are used for scanning the ultrasonic detector through the different positions, the general requirement on the stages is high resolution, see chapter 3. We used for RSOM high resolution piezo stages (model M683, PI, Karlsruhe, Germany). These stages have a resolution of $0.3 \mu\text{m}$, which is more than enough, considering that the resolution of the system is on the order of $20 \mu\text{m}$. Such scanning could be performed in two ways, either discrete movement on both axes or continuous movement on one of the axes, which we call the fast axis. This way the acquisition is accelerated by one or two orders of magnitude. The scanning speed v_{scan} is limited by the pulse repetition frequency of the laser (PRF_{laser}), and the step size of the scan Δx , this could be written as:

$$v_{scan} = PRF_{laser} \cdot \Delta x. \quad (5.1)$$

Other possibilities for scanning are to use an immersed mirror, in this case the transducer remains at one position, and the mirror guides the ultrasound from one position to another. This scanning is similar to what happens in laser scanning microscopic systems, where light is scanned by using galvanometric mirrors. Although scanning the ultrasound beam is an interesting idea and holds a lot of potential, especially for fast systems, nonetheless for pulse repetition frequencies of several kHz it doesn't hold a lot of advantages [78].

5.2.5 Synchronization and control of the system

For synchronization of the measurements and control of the system a personal computer (PC) was used. The control was done through the instrument control toolbox of Matlab

as the system matured the synchronization advanced as well. Currently, we acquire in multi-record mode, see section 3.4, as discussed in chapter 3 such an acquisition scheme is more than enough for our needs. This way all the pulses occurring during a b-scan are transferred together to the PC.

As there is a jitter between the time the stage starts actually to move, and the moment when the DAQ starts recording we upgraded the trigger strategy. In the new strategy instead of triggering the laser continuously we let the stage send trigger pulses when it has reached a certain position¹, both kinds of synchronization are seen in figure 5.1.

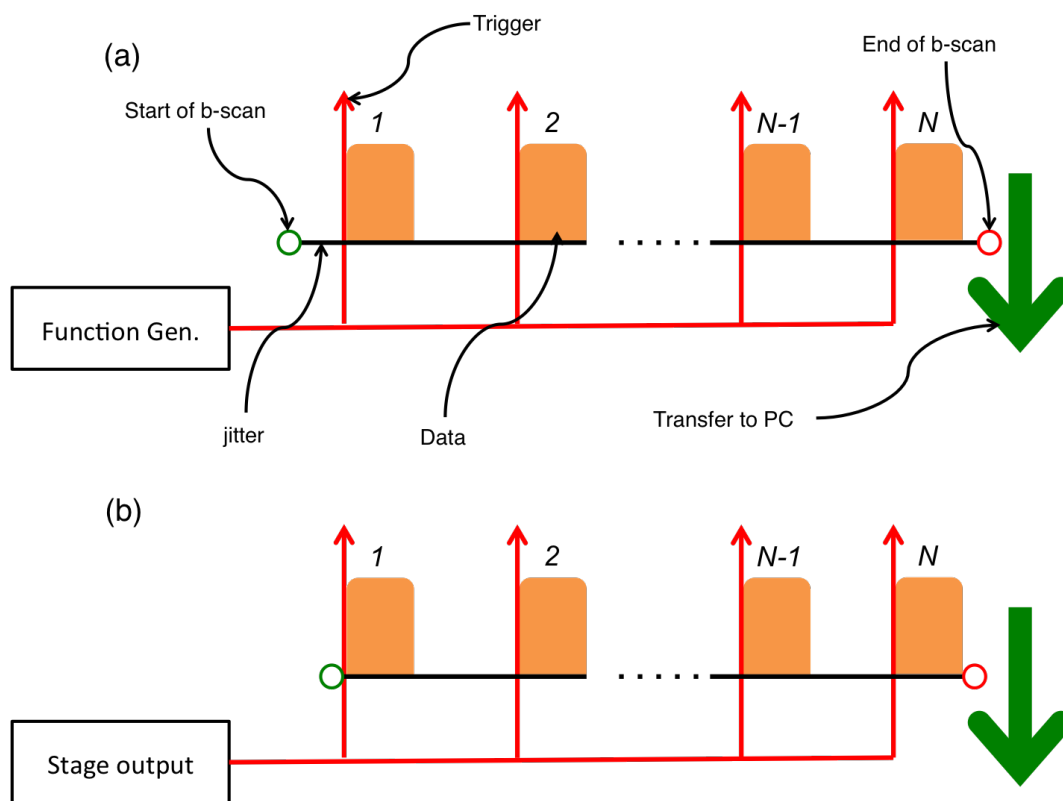


Figure 5.1: (a) Normal operation and synchronization, (b) synchronization based on pulses from the stage.

¹As there is a discrepancy between the pulse width of the stage output $\tau_{stage} = 50 \mu s$, and the laser requires a trigger pulse of at least $\tau_{trig} \geq 125 \mu s$, we used the 555 timer chip to increase the pulse width coming out of the stage.

5.3 System characterization and calibration

In this section we will describe how we characterized the system, the characterization ranges from measuring the resolution, to measuring the bandwidth of the detector, and finally the characterization of the penetration depth of the system, and the degradation of the resolution with depth. For most of these characterization we used small micro-spheres, either $10\ \mu\text{m}$, or $3\ \mu\text{m}$ microspheres (Polybead, Polysciences Inc., Warrington, Pennsylvania, USA). In other experiments we used surgical sutures with a nominal diameter of $10\ \mu\text{m}^2$. All of these objects strongly absorb light, and generate broadband optoacoustic signals of hundreds of MHz , depending on their size, and the pulse width of the laser as we are going to see [19, 36, 62, 79]. Similar objects were used as well to find the focal point of the detector.

5.3.1 Bandwidth characterization

To characterize the bandwidth of our detectors we used small microspheres, mostly $10\ \mu\text{m}$ microspheres, located in the acoustic focus of the detector. After scanning the phantom containing the microsphere, we located it. We subsequently moved the acoustic focus to it. Initially this consumed a lot of time because of the slow acquisition times; we used back then a slow laser with a repetition rate of only 20 Hz, thus the scan times were on the order of several hours.

We started with the 78 MHz detector, which we will call detector 1. At the very beginning when we measured the optoacoustic response from the microsphere using detector 1 we observed a strange behavior. Although the test-sheet of the detectors shows frequencies above 100 MHz, we were able only to measure signals up to 80 MHz. This behavior could be explained by simple calculations taking into account the laser pulse width τ_{laser} , which based on the stress confinement condition limits our bandwidth, see section 2.1. To test our hypothesis we brought another laser, with $\tau_{laser} = 1.8\ \text{ns}$, such a pulse width is theoretically capable of generating optoacoustic waves up to 275 MHz. Thus, the generated

²This size usually refers to a size range, for example $10\ \mu\text{m}$ usually refers to a size range of 10-19 μm .

optoacoustic signals are much shorter, see figure 3.2(a).

After measuring the microsphere with the short pulse laser, we calculated the Fourier transform of the measured signals. This time the frequency content extends beyond the 100 MHz point, and reaches around 150 MHz, limited by the actual bandwidth of the detector. Because of this we took the range 25-125 MHz as our bandwidth, see figure 3.2(b).

With the new detector, detector 2, which has a center frequency of 98 MHz, and can measure signals up to 180-200 MHz according to the test-sheet, the 10 μm microsphere is too big to cover its expected bandwidth, for example such measurements generates optoacoustic signals that have a zero at around 150 MHz with τ_{laser} of 0.9 ns, and measuring a smaller sphere such as a 3 μm microsphere inside the focus proved to be difficult. Thus, for reconstruction we use the bandwidth of 20-180 MHz, provided in the test-sheet.

5.3.2 Resolution and penetration depth characterization

There are several definitions of resolution, the most famous being the Rayleigh criterion [80]. Using this criterion two objects are said to be resolved if it is possible non-ambiguously to distinguish between them. Usually, this is done by moving two objects as close to each other as possible, and then plotting a cross section through their profile. When the two objects move closer and closer towards each other their peaks also do so, and at some point they merge together, if this happens when one peak coincides with the zero of the other object then this is called the Rayleigh criterion, and as we have seen in section 2.4.3, for a focused detector this is equal to [37]:

$$\delta_s = 1.22\lambda F_{\#}. \quad (5.2)$$

As manipulating small micro-particles is extremely difficult, this approach is not suitable. Thus, we took another approach, where we imaged micro-particles inside the focus, and outside of the focus of the ultrasonic detector. After reconstructing and plotting the results we get an image of this particle, in the case when the particle is much smaller than the expected resolution of the focus this image is called the point spread function (*PSF*) of

the system. The full width at half maximum ($FWHM$) of the PSF is considered as the resolution in this case, the $FWHM$ is given by [37]:

$$\delta_s = 1.4\lambda F_{\#}. \quad (5.3)$$

If on the other-hand the size of the particle imaged is comparable to the expected resolution of the system, then its size needs to be de-convolved from the resulting image, and the $FWHM$ of the result is considered as the resolution then.

Detector 1 had a bandwidth of 25-125 MHz as we saw in the previous section. To characterize the resolution we imaged $10\ \mu\text{m}$ microspheres that were embedded in a turbid phantom for homogeneous illumination, the microspheres were distributed at all depths homogeneously. Thus, we first imaged a microsphere in focus, and afterward we imaged the rest of the phantom by raster-scanning it. After reconstruction, we took cross sections across microspheres at different depths.

For the microsphere at focus the $FWHM$ is equal to $22\ \mu\text{m}$, which is upon de-convolving the size of the sphere from it, gives a $FWHM$ of $18\ \mu\text{m}$. Corresponding roughly to the width of the focus at 100 MHz, the width of the focus could be derived according to (2.36). Outside of the focus we calculated slices of $100\ \mu\text{m}$ each, centered at different depths, from these slices we took the maximum intensity projection (MIP), and on the MIPs we plotted the profiles of different microspheres. From these profiles, we took the $FWHM$ to represent the resolution of the system. At all the different depths the $FWHM$ of the in-plane profiles was around $30\ \mu\text{m}$, and the axial $FWHM$ was $7\ \mu\text{m}$, corresponding well to the expected resolution derived from the bandwidth of the detector. Moreover, the resolution is isotropic in-plane, and homogeneous at the different depths, this results from the full 3-dimensional reconstruction using the dynamic aperture [2, 36].

For detector 2 we characterized the resolution using $3\ \mu\text{m}$ microspheres. Such microspheres are suitable for characterizing the resolution as they are much smaller than the expected resolution given by the width of the focus of the detector at the center frequency, 100 MHz. Again the microspheres were embedded in a phantom made from turbid agar for homogeneous light distribution, after the measurement, reconstruction was performed

using 3-dimensional beamforming with a dynamic aperture. After reconstruction profiles were taken across the images of the microspheres to give an estimate of the resolution. The *FWHM* of the results show that the in-plane resolution was $18 \mu\text{m}$, and the axial resolution was $4 \mu\text{m}$. Once again, the resolution was isotropic in-plane.

To characterize the homogeneity of the resolution at the different depths another phantom was prepared, this phantom contained a knot made out of a $10 \mu\text{m}$ surgical suture, which is also a good absorber, the knot was imaged at different depths: 2 mm, 3 mm, 4 mm, and 5 mm. Afterwards a profile was taken across the point where the two sutures start separating from each other, the distance between the two sutures is $30 \mu\text{m}$, and it degrades minimally to $35 \mu\text{m}$ at the depth of 5 mm.

5.3.3 Calibration of the system

One of the first measurements that we did with the detector involved characterizing its focal spot, as well as the optimal speed of sound for best reconstructions.

Although the dimensions of the detector are provided by the manufacturer in the test sheet, minimal errors in the distance of the focal spot, in the range of $5\text{-}10 \mu\text{m}$, makes a huge difference for reconstructions, and can focus, or de-focus the image. Moreover, the time it takes for the signal to propagate from the focus towards the detector, is not only the focal distance divided by the speed of sound, rather it is a combination of the time it takes the optoacoustic wave to reach the acoustic lens, which is characterized by the focal distance, combined with the time it takes the wave to propagate inside the acoustic lens, which is characterized by a parameter called the delay line: t_d . In such a case the total time, which we call the focal time (t_F) is given by:

$$t_F = t_d + \frac{F}{v_s}. \quad (5.4)$$

In conclusion to verify the numbers given by the manufacturer, and to calculate the optimal focal point, that will be used later in the reconstructions we characterized the focal time, see (5.4).

To characterize the focal time, we used a $10\ \mu\text{m}$ suture, that was scanned in and out of the focus, the point where the maximum is found we call it the focal time. If an object is imaged inside the focus, then no reconstruction is needed.

This characterization of the optimal focus time, generated $t_F = 1.84\ \mu\text{s}$ for transducer 1, and $t_F = 1.74\ \mu\text{s}$ for detector 2.

5.4 Reflection-mode RSOM

5.4.1 System design

Until now we discussed the operation of a trans-illumination system, in this configuration the sample is illuminated from one side, and the signals are collected from the opposite side. This system was used to generate very nice images of a drosophila pupae expressing GFP from the future location of the wings, as we will see in chapter 6, as well as images of the vasculature of a mouse ear. Nonetheless, to fully use the potential of RSOM it needs to operate in reflection-mode. In the reflection mode (also called epi-illumination), both the acoustic detection and the optical excitation are arranged on the same side. Such a configuration is more universal, and could image more samples, especially in those cases where it is difficult to efficiently illuminate from one side and detect from the other side, such as skin lesions, tumor models in mice, disease micro-environments, and samples that are prepared in special holders, where access is provided only from one side, such as cells.

Many mesoscopic systems are reported that operate in the epi-illumination mode, such as a 24 MHz system based on a linear array [81], an all optical optoacoustic scanner [82], as well 50 MHz raster scan systems [74, 83, 84]. Again, we wanted to explore higher frequencies. Thus, we decided to go for a 100 MHz detector, detector 2. Unfortunately, we couldn't use detector 1 for epi-illumination, because it had a large shape, and it was impossible to couple light from the same side, see figure 5.2, because of this we decided to go for custom made design, here we asked our partner company to produce a new transducer which had the lens shaped in the form of a cone, such a cone would allow coupling of light at an angle of 45° .

Coupling of light would be performed using fiber bundles, where the light is coupled at one side, and on the other side the light is divided into several arms, which are used to generate a homogeneous illumination at and around the focal spot of the detector. It is necessary to maintain a homogeneous illumination around the focal spot, within the area necessary for beamforming, or within what we call the beamforming radius (R_{BF}), see (2.47). If this is the case, then the signals are summed coherently from the different positions. Ideally, the illumination should be stationary, but this would limit the scanning area. Thus, it is only suitable for small samples, where the detector doesn't need to scan several mm 's.

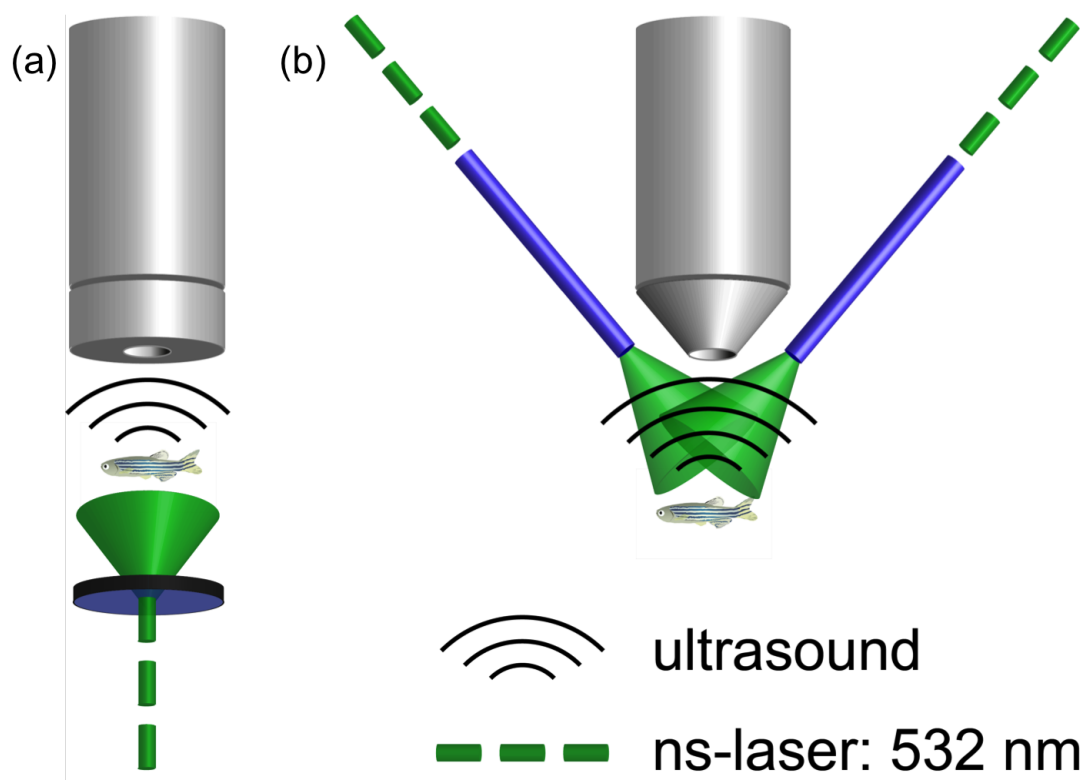


Figure 5.2: Comparison in the form of the old detector (a), and the new detector (b).

5.4.2 Performance comparison of 100 MHz and 50 MHz systems

For several measurements we used both a 100 MHz detector, and a 50 MHz detector, if the 100 MHz detector is used we call the system RSOM100, on the other hand if the 50 MHz detector is used we call the system RSOM50. For both cases, the illumination was provided by a fiber bundle with three arms.

The next table shows a quantitative comparison between the two detectors:

	100 MHz	50 MHz
Center frequency	98 MHz	51.5 MHz
Usable bandwidth	10-180 MHz	5-95 MHz
Diameter (D)	1.5 mm	3 mm
Focal distance (F)	1.65 mm	2.97 mm
Angle of acceptance	51°	61°
Resolution	18 μm	30 μm

Table 5.1: Comparison between the characteristics of the 100 MHz detector, and the 50 MHz detector.

In table 5.1 a new term has been introduced, usable bandwidth, this refers not to the -6 dB bandwidth reported in the manufacturers test-sheet, but rather to the range of frequencies that we found useful in reconstruction, and give meaningful results.

A further comparison between RSOM50 and RSOM100 is shown in figure 5.3, it shows both the angular coverage of both the detectors used in RSOM50 and RSOM100, as well as a comparison of the achievable in-plane resolution of both RSOM50, and RSOM100.

The major difference between the two detectors is in the focal distance, in the case of RSOM50, the focal distance is farther away. Thus, it is easier to perform scans than using RSOM100. Another difference is in the diameter of the active element, which is twice as large in case of RSOM50 compared to RSOM100, thus RSOM50 is four times more sensitive than RSOM100³, this larger active area means that lower laser energies could be used for scanning of biological samples.

RSOM50 also has a larger angle of acceptance, although not significantly larger than RSOM100, it still better captures the oriented structures compared to RSOM100, this larger angle of acceptance makes RSOM50 a better choice for imaging of oriented structures, such as vessels, and surfaces.

Because RSOM50 has a lower resolution than RSOM100, the scanning steps are larger, while still satisfying Nyquist criteria, see chapter 2, and thus either the field of view (FOV) could be increased, or the scanning times could be decreased.

Although RSOM50 is better than RSOM100 in many aspects, we need to keep in mind that RSOM100 is capable of achieving better resolution, it can better detect and image smaller structures, and finally for smaller structures, where most of the generated frequencies are

³The detection sensitivity is proportional to the area of the active element [40].

high frequencies it is definitely a better choice than RSOM50.

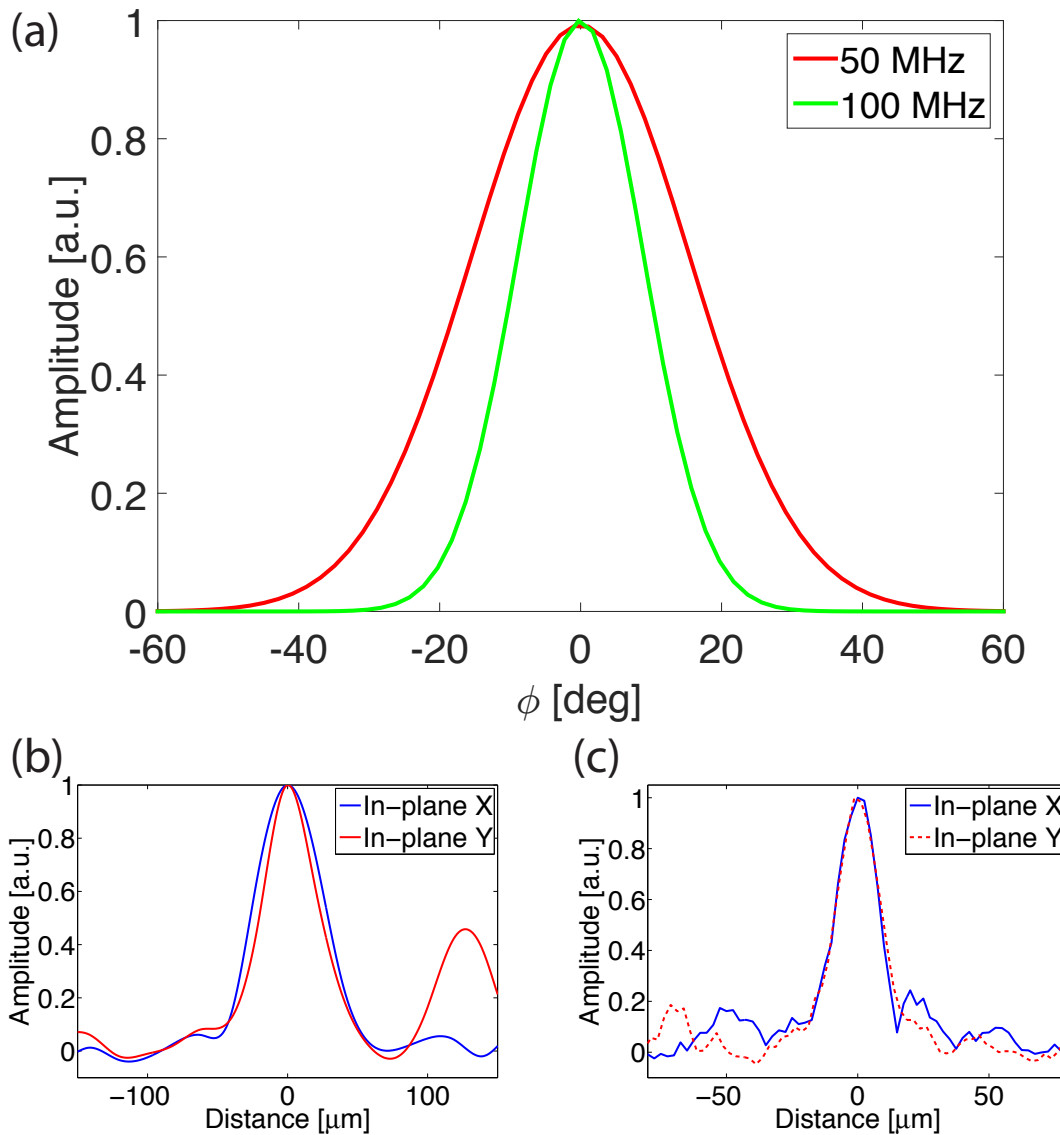


Figure 5.3: Comparison of the performance of RSOM50 and RSOM100. (a) angular coverage of RSOM50 vs. RSOM100, (b) FWHM of a $10 \mu\text{m}$ sphere imaged with RSOM50, (c) FWHM of a $3 \mu\text{m}$ sphere imaged with RSOM100.

From the previous discussion it is obvious that no detector by itself is the ultimate detector, rather in a practical situation there might be need for using both the 100 MHz, and the 50 MHz, where one captures the fine structures, and gives more details into a specific region, while the other one images larger structures, and captures a larger field of view (FOV). Moreover, because lower frequencies are less attenuated in biological tissues than high frequencies are, this means that with RSOM50 it is possible to image deeper than

what is possible with RSOM100, but at a coarser resolution.

First examples of where such a combination is used will be seen in imaging tumor models in mice, in section 6.4.

5.5 Tomographic RSOM

5.5.1 What are the limitations of RSOM?

Although RSOM is capable of generating great images of several biological samples, as we will see in chapter 6, it is possible to image model organisms used in developmental biology, in imaging tumor development, and in imaging human skin. It has some drawbacks:

1. The limited angle of acceptance of the detector, which is defined by the $F_{\#}$ of the detector, thus for the 100 MHz detector it is around 50° , and for the 50 MHz detector it is 60° . This limited numerical aperture is a problem in the sense that it limits the resolution as we have seen in chapter 2 that the resolution is inversely proportional to the $F_{\#}$. Another problem is that absorbers that don't radiate acoustic signals isotropically, might not be detected by the ultrasound detector, This means that at least two-thirds of the energy is not detected by the detector. Thus, many structures inside the sample might not be seen, for instance in the case of zebrafish imaging, the side walls of the fish are not seen.
2. The second problem lies in the high attenuation of the high frequency acoustic waves, as we have seen in chapter 2, the acoustic attenuation coefficient increases with f^2 in water, and linearly with f in biological tissues, thus the ultrasonic waves that have to travel from the other side of the sample are displayed with a much less amplitude than those which travel from the side of the sample close to the detector.
3. Finally, the sample is not homogeneously illuminated, it is either illuminated in trans-illumination mode where the backside of the sample receives more light, or it is illuminated in epi-illumination mode, where the front side of the sample receives more

light than the back side, in both cases this results in a non-homogeneous illumination. Even if a scattering medium is used, one side still receives more energy than the other one, if moreover the sample is strongly absorbing a small amount of energy will reach to the other side of the sample.

5.5.2 Design of a tomographic RSOM

To overcome the issues mentioned in section 5.5.1 the following we decided to develop a tomographic RSOM. From the very beginning we have designed this system to be suitable for imaging of model organisms used in developmental biology and experimental genetics. Such organisms include *Xenopus*, zebrafish, and *Drosophila Melanogaster*⁴. These organisms share a similar form, all of them are cylindrical. Thus, it is possible to embed them into agar, and then rotate the sample throughout the different angular positions.

It is advantageous to both rotate and translate the sample. This combination will result in a more homogeneous resolution in plane, the ultrasonic waves propagating at angles larger than the angle of acceptance of the detector will be detected, and the effects of the acoustic attenuation of the signals will be minimized. Moreover, such a design allows for a homogeneous illumination of the sample from all sides. Thus, minimizing the effects of single sided illumination and increases the coherence of the generated optoacoustic signals when measuring from the different angles.

Before agreeing on a certain geometry we considered both horizontal rotation of the sample, and vertical rotation of the sample, the horizontal case is advantageous because at first thought RSOM doesn't need to be changed, or modified, where only an extra bath with a rotation stage is added. Nonetheless, the mechanical design, where a gear box is needed to translate the rotation from the rotation stage to the axis of rotation, as well as trying to keep the agar phantom from falling down, or bending, during rotation. As this design looked like a complicated structure, we moved to a vertical configuration, where the sample hangs from a special holder through the rotation stage. This vertical design is much simpler for assembly, the sample won't bend from one side to another during rotation, and it allows

⁴Johannes Rebling, a master student of mine, helped in designing and assembling the system.

greater flexibility in putting the sample in and out of the holder.

The new design will enable a multi-view, or a multi-orientation RSOM (MO-RSOM), where the detector is scanned in the xz -plane, and then the sample is rotated around the z -axis, a schematic of the system is shown in figure 5.4.

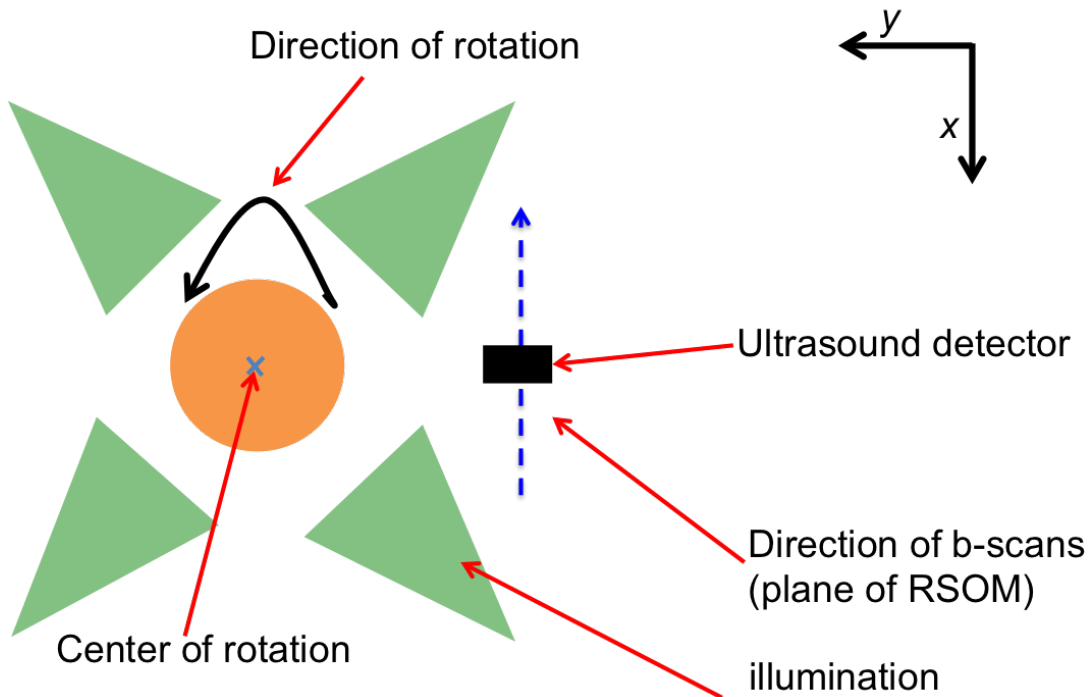


Figure 5.4: Schematic of Multi-Orientation RSOM

5.5.3 MO-RSOM calibration and reconstruction

Because of the tomographic nature of MO-RSOM, knowledge about the relative positions of the detectors to each other is not sufficient anymore, rather a knowledge about the absolute positions in respect to the axis of rotation is required. Thus, we reconstruct the measurements at the individual angles, in the same way as in RSOM. After the reconstruction we take a section from every angle and combine it with the sections from the other views. The optimum combination will result in the signals being summed coherently, thus the amplitude is maximized, the two parameters that we vary to reach the optimum values are the center of rotation (COR), and the lateral distance between the center of the array, and the axis of rotation ($shiftX$). Once the optimum values are found we combine the reconstructions at the different angles, see figure 5.5.

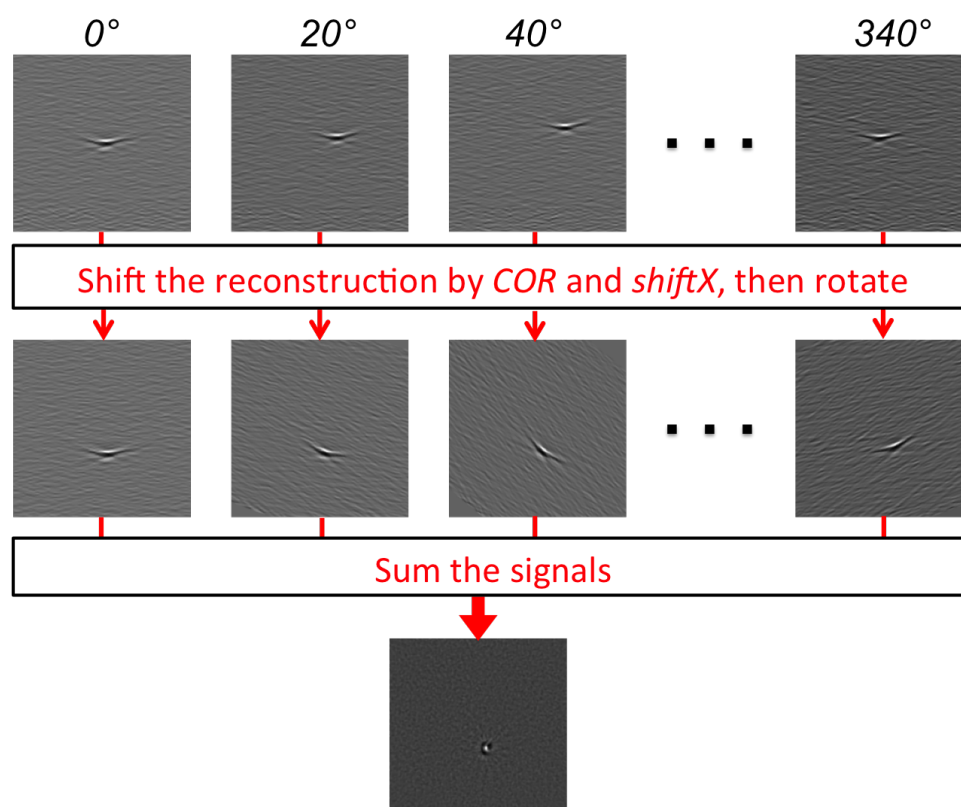


Figure 5.5: An example of combining the different views in MOR SOM, different measurements taken at different angles, with steps of 20° are combined into a single image, with improved resolution and *SNR*.

5.5.4 Characterization of MO-RSOM

Besides the obvious improvement on the *SNR*, we performed two measurements, in the first one we used a suture normal to the axis of rotation, which we rotated through the different angular positions and collected optoacoustic signals, the amplitude of the optoacoustic signal was plotted against the angle to characterize the angle of acceptance of the detector, which is seen in figure 5.6. By rotating the sample through different angular positions, the signals that are not measured because of the limited angular coverage of the detector at one angular position are measured by the detector at another angular position, resulting in a complete angular coverage of the sample.

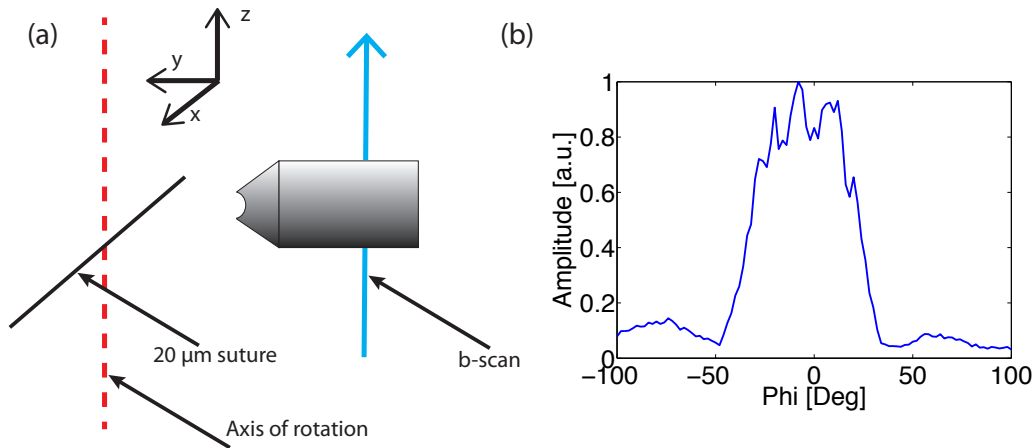


Figure 5.6: A figure showing the measurement, as well as the measured angular coverage of the 50 MHz detector.

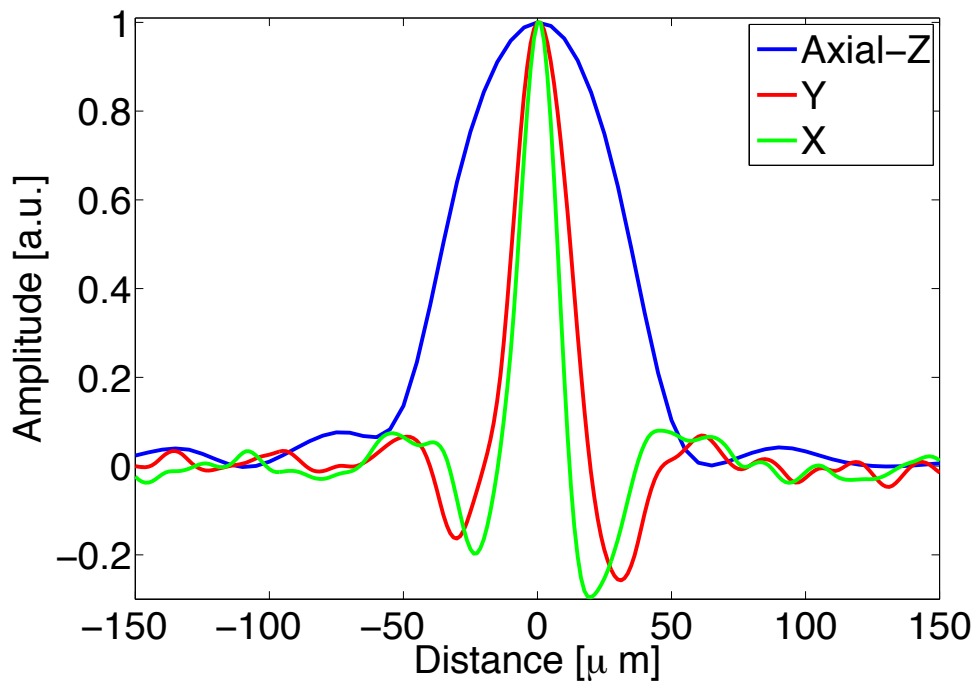


Figure 5.7: Profiles through a 10 μm sphere measured with MOR SOM.

Then we imaged 10 μm spheres embedded in turbid agar, after reconstruction, and combination of the different angles together into a single reconstruction, we took profiles through one of the microspheres. As we can see we get almost an isotropic resolution in plane on the order of 15-20 μm , and an axial resolution around 70 μm , this way we have improved the resolution along one of the axis, the results are plotted in figure 5.7. As

discussed in section 2.5.5 because of the tomographic nature of MO-RSOM the in-plane resolution improves, and becomes defined by the detection bandwidth, see (2.45).

The total measurement time depends on the number of angles measured, for angular steps of 20° the measurement lasts around 30 minutes, which could be accelerated in the future.

5.5.5 Examples of MO-RSOM imaging

To showcase the performance of MO-RSOM we imaged a 7 dpf zebrafish, wild zebrafish, for comparison with RSOM we took cross sections from a single view (at angle 0°), and we compared this with the resulting cross sections when taken from the combined image. We embedded the fish in turbid, low melting agar, and imaged at angular steps of 20° . The results are shown in figure 5.8. A comparison of cross sections taken at the same location, shows improved performance for MO-RSOM compared to RSOM, not only in terms of *SNR*, but also in terms of the information seen on the cross sections.

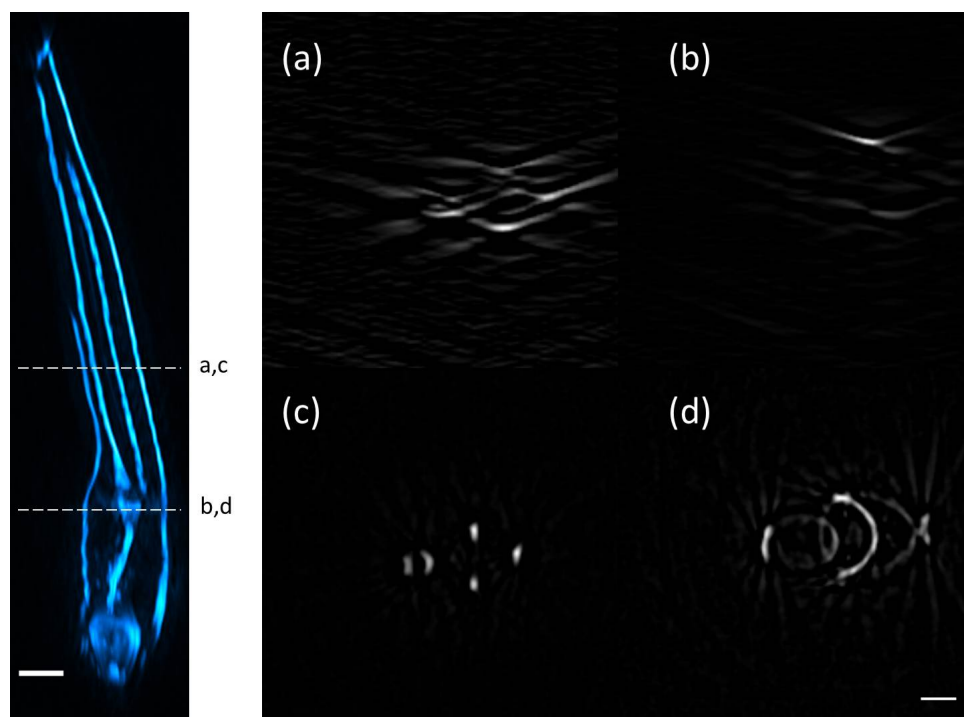


Figure 5.8: A fish measured with MORSEM, as well as a comparison of the cross sections, generated using RSOM (a, b), versus MORSEM (c, d).

5.6 Combination with optical microscopy techniques

RSOM delivers nice images of different samples, nonetheless, it doesn't normally reach the resolution of microscopic techniques, such as two photon laser scanning microscopy (TPLSM), second harmonic generation microscopy (SHG), third harmonic generation microscopy (THG), selective plane illumination microscopy (SPIM), and optoacoustic microscopy (OAM). On the other hand, these microscopic techniques are not capable of penetrating deep into biological tissue, where diffusion of light becomes an issue [13], see figure 1.2. Because of this, the combination of both should make a nice paradigm, where microscopic techniques either image the first hundreds of microns of tissue, and mesoscopy image deeper structures. Or in which optoacoustic mesoscopy images a large region, and then microscopic techniques zoom-in into a smaller region of interest, with higher resolution.

Example applications of such a combination would be in imaging model organisms, such as the zebrafish, through the different phases of development, from embryonic to post-embryonic. In such a case microscopy can image the first stages of development and optoacoustic mesoscopy images the later stages of development. In this section, we will describe such a combination, where optoacoustics is combined with non-linear microscopy techniques. Before describing the combination we will briefly describe the individual imaging modalities; then we will discuss their complementarity, and finally we will talk about their combination. Although it is possible to combine RSOM with different modalities, here we will only describe this combination with non-linear microscopy techniques, more specifically with multiphoton techniques.

5.6.1 Non-linear optical microscopy techniques

Non-linear microscopy is based on the interaction of multiple photons with tissue simultaneously; this happens when several photons cooperate to elevate the energy of an electron from the ground level to an excited energy level. Usually, this requires high light intensities both spatially, and temporally. Because of this dependence on high intensities multiphoton

microscopy has better sectioning capabilities than other optical techniques. This process is possible by using ultrafast lasers, capable of generating fs-pulses, these pulses are usually generated through a process called mode-locking [61]. Such requirements on pulse width, and tight focusing emerge, because the multiphoton process is a statistical one in nature, where the first absorbed photon elevates the electron into a virtual energy level, and the electron stays there for a short amount of time, if within this amount of time a second photon hits the atom or the molecule, then this electron is elevated into a higher energy level. If, on the other hand, the second photon arrives at a later time, after the electron has returned to the ground level, then no photon absorption is experienced by the atom or the molecule. Thus, the two photon absorption rate (dN_{TP}/dt) is given by the quadratic relation [85]:

$$\frac{dN_{TP}}{dt} = \sigma_{TP} N_{GS} F^2, \quad (5.5)$$

where: N_{TP} is the number of molecules in the excited energy level due to two-photon absorption, σ_{TP} is the two-photon absorption cross section, N_{GS} is the number of molecules in the ground energy level, and F is the photons flux (number of photons per unit time and area.) In the case of three photon absorptions, (5.5) will depend on the third power of the flux.

As in the case of confocal microscopy, laser scanning, usually based on galvanometric mirrors, is used to scan the focus of the laser beam in the xy -plane. While a motorized stage is used to translate the imaging plane along the z -axis. Other possibilities exist to capture the whole imaging plane at once, like in temporal focusing, where the fs-pulse diverges temporally, and only converges at the focus [86, 87].

The most prominent examples of multiphoton microscopy are two photon microscopy, second harmonic generation, and third harmonic generation.

Two photon microscopy is a fluorescent microscopy technique, where the same fluorescent markers that are used for confocal microscopy are used here as well. Nonetheless, ultrafast laser pulses, with double the wavelength, of the lasers used for confocal microscopy are used here. This results in higher penetration depth compared to confocal microscopy, and in less photo-toxicity, because only those molecules which satisfy (5.5) get excited.

Because of its high penetration depth, low photo-toxicity, and high speed, two photon microscopy has become a workhorse and the desire of many laboratories. Applications include neuroscience [88], developmental biology [89], and monitoring of tumor growth among others [90].

Another technique which is based on multiphoton interaction with tissue is called second harmonic generation microscopy (SHG) [85,91,92], in SHG two photons are combined together to generate a third one with half the wavelength, and double the energy, this happens in non-centrosymmetric structures, such as collagen, myosin fibrils, and microtubules [92]. Which enables imaging of such tissues as muscle fibers.

A third process for multiphoton excitation is called the third harmonic generation microscopy (THG) [89,93–95], in this process three photons combine together to generate a fourth one, with one-third the wavelength, and three times the energy. This process always happens when there is an optical heterogeneity, for instance at the interface between two different kinds of tissues, or when the photons meet a small particle on their way. Because of this THG has been used to image the nuclei of cells or imaging of lipids [96].

From the above mentioned techniques SHG, and THG are label-free, while two photon microscopy requires fluorescent labeling of the samples, such fluorescent labels of the samples are commonly used these days, thus if a tunable laser exists a multitude of fluorochromes, and biological tissues could be imaged.

5.6.2 Optoacoustic microscopy

Optoacoustic microscopy, is another technique based on the optoacoustic effect [40,97–99], it differs from optoacoustic mesoscopy in the way the light is delivered to the sample. In the case of optoacoustic mesoscopy, the light is homogeneously illuminating the whole sample, and the resolution comes from the acoustic detection, while in the case of optoacoustic microscopy, sometimes known as optical resolution optoacoustic microscopy, a focused beam of light is used, in a similar way to optical microscopy techniques, and the ultrasound is detected only from the optical focus. Thus finer resolution, on the same order as in confocal microscopy, and two photon microscopy could be achieved in optoacoustic

microscopy as well, resolutions as fine as 200-300 nm have been reported [100].

The resolution in optoacoustic microscopy is defined laterally by the size of the optical focus and axially by the bandwidth of the ultrasonic detector. Thus high-resolution, label-free, images of optical absorption could be generated, see figure 2.2, moreover if a tunable laser is used. Then it is possible to generate multicolor images of optical contrast. Because optoacoustic microscopy is based on focusing of optical beams, this limits the penetration depth to a few hundreds of microns [13], limited by the optical mean free path in tissue.

Since its inception in 2008 this method has found wide use, where it is used to image micro-environments of diseases, generate high resolution images of tumors, and micro-vasculature.

Unlike optical microscopy techniques where laser scanning is used, usually mechanical scanning is used in the case of optoacoustic microscopy, the reason behind being the need for high sensitivity, the highest sensitivity could be achieved only when both the optical and the acoustic foci coincide, hence confocal. Thus, usually either the sample is scanned, and the optical and the acoustic heads are static [92] or the optical and the acoustic head are combined using homemade optical and acoustic lenses [98, 99]. Laser scanning has been tried before, but this resulted either in a shrinking of the field of view, where the laser scanning is done within the acoustic focus of the detector, or degradation in sensitivity, where unfocused detectors are used [101, 102].

As discussed in this section, optoacoustic microscopy has a resolution cell that is much larger in the axial direction than it is in the transverse direction, some groups are trying to use non-linear effects, and absorption saturation to improve the axial sectioning of optoacoustic mesoscopy. Nonetheless, these methods are still relatively slow [103, 104].

5.6.3 Hybrid multiphoton optoacoustic microscopy

From what has been previously mentioned it is obvious that these methods can complement each other, where two photon microscopy images the fluorescent distribution, SHG images non-centrosymmetric structures, such as muscles, THG images the interfaces between the different tissues, and optoacoustics images the optical absorption, further functional

measurements could be done as well is more wavelengths are available. A schematic of the system is shown in figure 5.9.

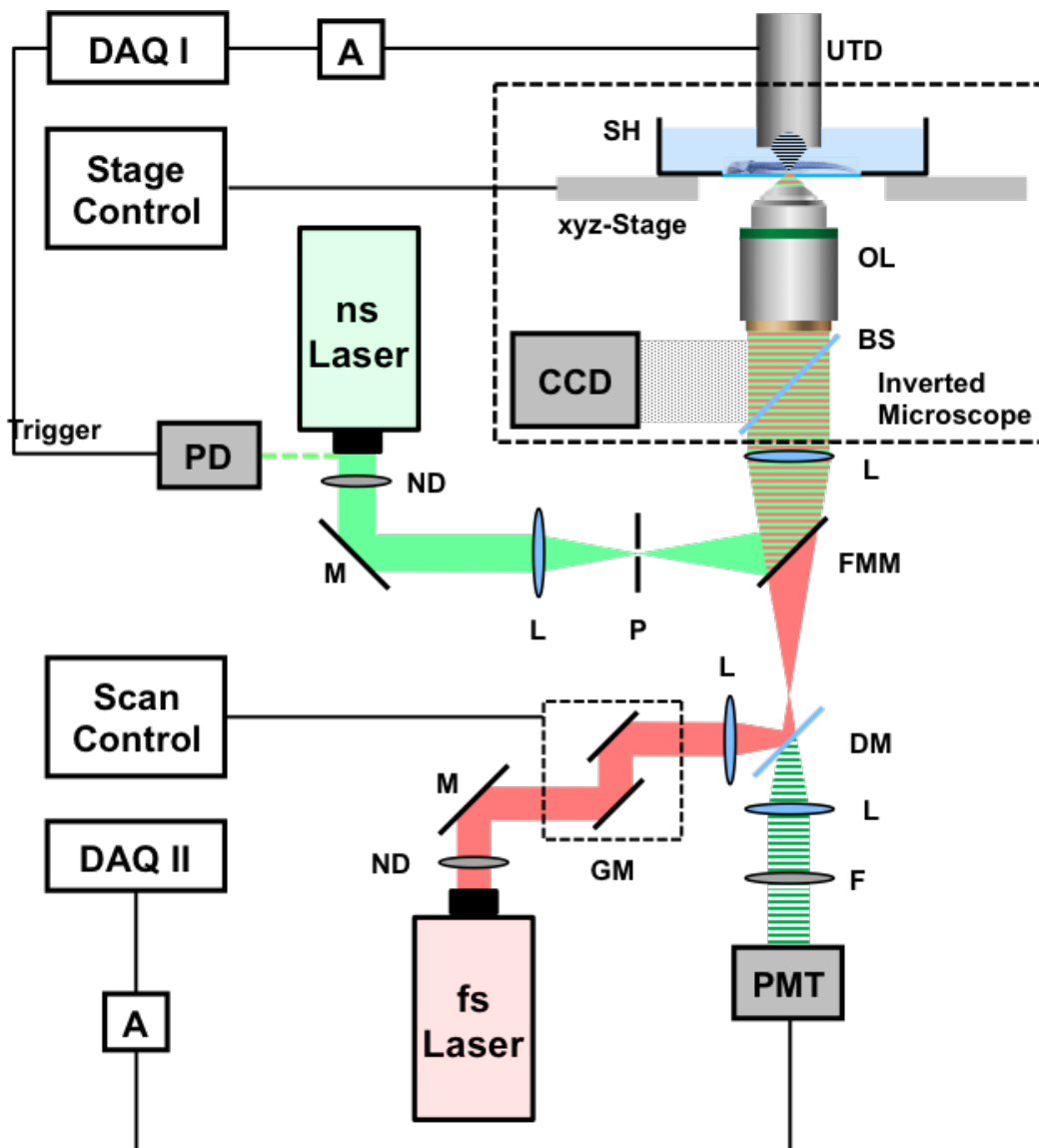


Figure 5.9: Schematic of the multiphoton, optoacoustic microscopy system (MPOM).

To build such a system we combined two optical paths, one for fs-laser, and one for ns-laser, afterward the optical focus is aligned with the acoustic focus. The fs-laser is scanned through galvo mirrors, and the fluorescence, as well as the harmonics, are gathered and measured using photo-multiplier tubes. The optoacoustic measurement is done through mechanical scanning of the sample, to keep the foci confocal, afterward the sample is translated to the next z -plane [92, 105].

This system has achieved a resolution of ca. 700 nm for the non-linear microscopy, and a

resolution of ca. $2\ \mu\text{m}$ for the optoacoustic microscopy, covering a field of view (FOV) of $400 \times 400\ \mu\text{m}^2$.

In the first few experiments a zebrafish was imaged, where the melanin pigments have been imaged using optoacoustic microscopy, while the muscles were imaged using SHG microscopy, see figure 5.10.

Currently, the system is being optimized for higher speed, larger field of view, and higher sensitivity⁵. Together these systems are called Hybrid, multiphoton optoacoustic microscopy (MPOM).

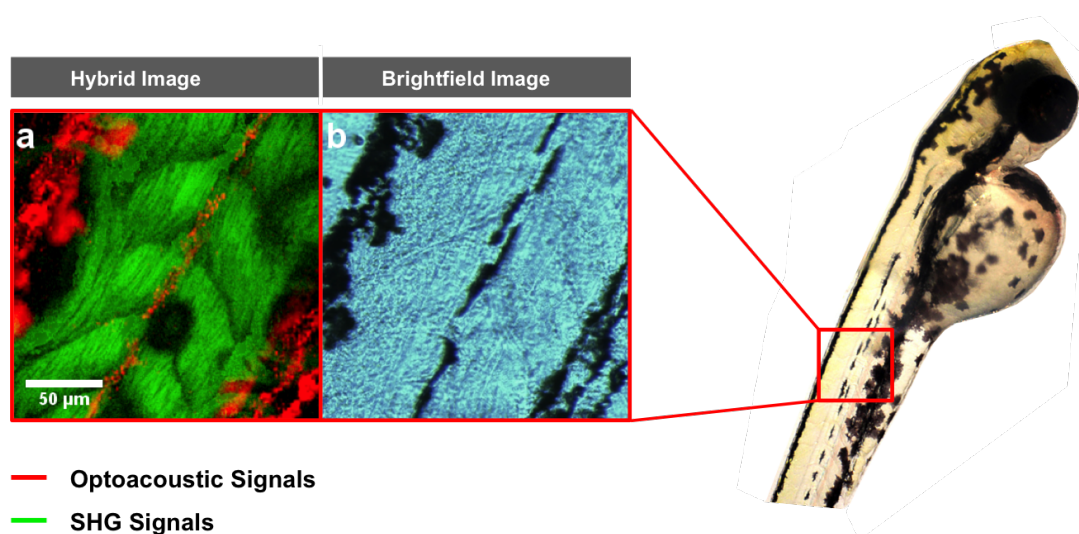


Figure 5.10: An example of a fish measured with MPOM. (a) An overlay of SHG and optoacoustic microscopy, (b) bright field image. The image of the fish is a courtesy of Google.

5.6.4 Combination with RSOM

All the systems mentioned in section 5.6.3 are microscopic, their FOV is limited, and their penetration depth as well. To improve on this, we are currently combining optoacoustic mesoscopy (RSOM), with MPOM. This way using RSOM a large FOV could be scanned, while MPOM generates higher resolution images of an interesting region of interest. This combination results in a true multi-scale high resolution imaging modality, currently such a system is being developed [105]. An example of the combination with RSOM is shown in

⁵This system, and the further optimization is being carried out by Dr. George Tserevelakis and Dominik Soliman

figure 5.11. Additionally, we combine other techniques such as selective-plane illumination microscopy with optoacoustic mesoscopy [106].

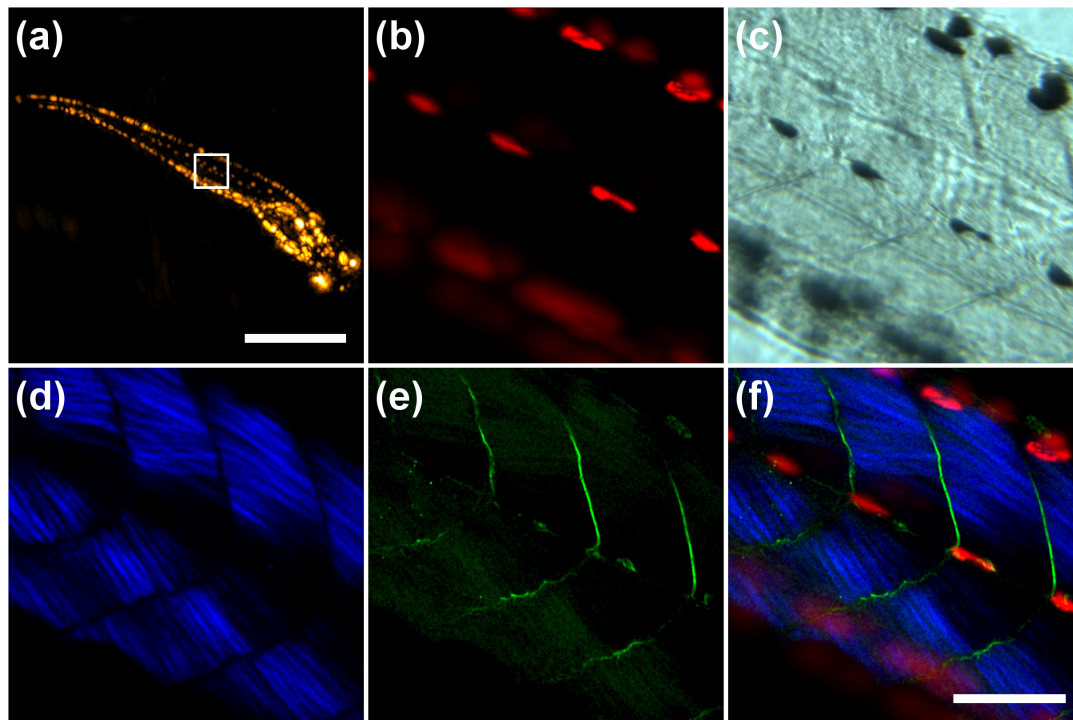


Figure 5.11: (a) Fish imaged in RSOM, (b) zoom in using optoacoustic microscopy, (c) bright field microscopy, (d) second harmonic generation showing the muscle fibers, (e) third harmonic generation microscopy showing the spaces between the muscles, (f) combination of (b), (d), and (e). Scale-bar (a) 0.5 mm, (b)-(f) 100 μm .

5.7 Discussion and outlook

In this chapter we have discussed a new technology, called raster-scan optoacoustic mesoscopy (RSOM), where the mesoscopic range refers to the size of the sample, or the depth of interest, which lies between what microscopy can offer, approximately 100-500 μm , and where tomography starts becoming interesting, i.e. above 5 mm, To achieve this we use broad illumination, in contrast to focused illumination for optoacoustic microscopy, and we use high frequency ultrasonic detectors, $f_c \geq 50 \text{ MHz}$.

We first developed a trans-illumination system, then based on a custom designed ultrasonic detector we developed an epi-illumination system, this allowed us to image all kinds of samples, not restricted by the illumination spot used in the case of trans-illumination. Reconstruction based on beamforming of the signals with dynamic aperture allowed us to

get a homogeneous resolution through several millimeters.

System characterization shows that a lateral resolution of $18\ \mu\text{m}$, and an axial resolution of $4\ \mu\text{m}$ could be achieved down to a depth of 5 mm [2], moreover, our experiments have shown the importance of laser pulse width on the generated frequencies [36], and thus on the final resolution of the image, this could be explained by the thermal, and the stress confinement condition, see chapter 2.

Using the highest repetition rate of the lasers that we have at the moment enables us to scan an area of $10 \times 10\ \text{mm}^2$ in less than 10 minutes, faster lasers will enable us to take this time down, although such a number appears long, and for some applications, such as cell division it won't generate any results, it is still fast enough for many applications, such as imaging morphogenesis on the whole organism level, as well as imaging of tumor development over time.

To optimize the system for model organisms a tomographic RSOM is currently under development, this as we have mentioned should improve several aspects of the system, first it will enable us to recover signals propagating outside of the angular coverage of the detector, second this will improve the resolution in the plane normal to the axis of rotation, in which the resolution will be defined by the bandwidth of the detector, rather than by the geometrical properties of the detector, see section 2.4.3, and finally this will improve the signal to noise (SNR) ratio of the image, in part because more projections will be taken, the SNR is proportional to the square root of the number of projections, and in part because the signals which originate from the side far from the detector, after a rotation of 180° will be on the side closer to the detector, thus less attenuated, this in turn will improve the visual perception of these signals.

As a tomographic system is not suitable for imaging of tumor development for example, for clinical applications, for such cases we are developing a system where several detectors are acquiring in parallel, as those detectors are located on a part of a hemisphere, this will synthetically increase the angular acceptance of the detector, not only improving the detection of tilted waves, but also improving the resolution and the SNR of the image.

Additionally, we are currently working on the development of point ultrasonic detectors, and

collaborating on the development of high numerical aperture detectors. In both cases the angular detection, and the in-plane resolution of the system will improve [52].

Besides the development of RSOM itself we are expecting that combining RSOM with other technologies, such as multiphoton microscopy, optoacoustic microscopy, and selective plane illumination microscopy, will add another dimension to the generated images, resolve small structures of interest on a larger RSOM image, and enable biologists to follow the development of model organisms from pre-embryonic to post-embryonic stages.

In addition to the development of the technology itself, a lot of efforts has been put into the understanding of the role of frequencies, within the framework of RSOM. We are developing new methods where we divide the detection bandwidth into several sub-bands, where each one of these sub-bands is treated separately. Finally, these sub-bands are overlaid together for improved visualization, and to recover lateral resolution as well.

Major problems on which we are currently working include both hardware and software problems, within hardware we are interested in higher repetition rate lasers. This increased repetition will reduce the measurement times. We are also interested in tunable lasers to enable multispectral imaging. This tunability will improve the molecular detection sensitivity and will enable multicolor imaging, where, for example, the bio-distribution of a molecular agent is displayed, or the oxygenated and deoxygenated hemoglobin map is shown. To enable better usage for RSOM, the reconstruction time needs to drop at least to the same order of magnitude of the measurement time, i.e. several minutes. To accomplish this we are currently working on the optimization of the reconstruction software; this includes better GPU programming among others⁶.

If we manage to achieve all what we mentioned then we expect RSOM to become a potent technology, and we expect it to be used in several biomedical applications, both pre-clinical and clinical. Moreover with new technologies, we expect the quality of RSOM images to improve within the next years.

⁶Mathias Schwarz is currently working on it.

Chapter 6

Applications of raster-scan optoacoustic mesoscopy

In this chapter we will discuss some applications of raster-scan optoacoustic mesoscopy (RSOM). We will start with a discussion of the application of RSOM in imaging model organisms, then we will talk about imaging of micro-vasculature, imaging of cells, imaging of tumor growth and development, and finish with a discussion of the application of RSOM in skin imaging.

6.1 Imaging of model organisms

Model organisms are widely used for the study of experimental genetics, and developmental biology, such organisms include *Caenorhabditis elegans*, *Drosophila melanogaster*, Zebrafish, and *Xenopus* among others. Light microscopy techniques, such as multiphoton microscopy, selective plane illumination microscopy (SPIM), and confocal microscopy, play a major role in studying the development of such organisms at the embryonic stages [107].

Developmental processes, such as neurogenesis, morphogenesis, and organogenesis, are dynamic processes that happen at several levels and scales. It includes fast cellular and sub-cellular processes where optical microscopic techniques are indispensable, as

well as slow processes that happen at the whole organ or organism level, where optical microscopic techniques are limited to the use at the embryonic, and sometimes early post-embryonic, where the sample is still small, and might be transparent.

In the case of larger samples, or for the post-embryonic stages where the organisms become opaque, and the size of the sample becomes larger than what optical microscopic techniques can offer in terms of penetration depth. It becomes necessary to look for alternative methods; such methods should be able to penetrate deeper into biological tissues while still keeping a high resolution. In such cases, optoacoustics becomes an attractive alternative, although with some relaxation on the spatiotemporal resolution compared to optical microscopy techniques.

Before showing some examples of imaging model organisms using RSOM, we describe how we embed and fix samples. Later we show examples, and proof of principle studies, to show the feasibility of raster-scan optoacoustic mesoscopy (RSOM) in imaging model organisms. The only organism that is not interesting for RSOM, is the *Caenorhabditis elegans*, with a diameter of $70\ \mu\text{m}$ it could be efficiently imaged with optical microscopy techniques, such as non-linear microscopy techniques, which could be used for example for fast volumetric imaging of neural circuits as an example [108].

6.1.1 Handling of samples

To fix the samples, we used low melting agar, solidifies at $37\ ^\circ\text{C}$, thus we could embed the sample at lower temperatures, compared to normal agar. This way we insure that the sample is not cooked during preparation. Finally, while embedding the sample in agar, we make sure that the axis of the sample is parallel to the scanning plane. Thus, most of the generated signals could be efficiently measured with RSOM. In MOR SOM, the sample is fixed in such a way that it is coaxial with the axis of rotation.

6.1.2 Imaging of *drosophila melanogaster*

*Drosophila melanogaster*¹, or fruit fly, is a widely used model organism, it is one of the favourites of developmental biologists, the reason for this its small size, its fast life cycle, and because its genetic map is well known and understood *drosophila melanogaster*. So it could be easily manipulated to express certain biomarkers from certain organs, such as the ability to express green fluorescent protein (GFP) from the wings. Or the ability to express the red fluorescent protein (RFP) from certain parts of the neural system, within a very fast time.

The life cycle of a *Drosophila melanogaster*, starts with an embryo, later it develops to a larvae, which could be easily studied using optical microscopy techniques, after growing enough as a larvae, the *drosophila melanogaster* enters the pupal stage, in this stage the *drosophila melanogaster* undergoes big changes, through these changes it becomes an adult fly, afterwards the cycle is repeated again.

The pupal stage is of extreme interest: during this stage, which lasts several days, the *drosophila* undergoes many changes. Thus, it is interesting to image it during this stage. The challenge though, is that after hour 30, the pupae becomes extremely opaque, and even such techniques as two photon microscopy are not able any more to penetrate deeper than 100-200 μm . The capability of optoacoustics in imaging the pupae has been previously shown, where multispectral optoacoustic tomography (MSOT) has been used to image eGFP labeled salivary glands. In this system a 15 MHz cylindrically focused detector was used, resulting in a diffraction-limited resolution of 38 μm [109].

To capitalize on our previous experience with imaging of *drosophila melanogaster* pupae, and to get better resolution, we imaged a pupae that expresses GFP² from the future location of the wings. For this experiment we used the first generation of RSOM, with trans-illumination, and a pulsed laser at 515 nm, which can pick up GFP expression, green fluorescent proteins, or GFP has a maximum absorption at 488 nm, but still absorbs at 515 nm. Moreover, we imaged a fly from the same transgenic line, in the case of the fly, the

¹We thank Dr. Moritz Bennecke for providing us with the *drosophila* samples.

²What we actually used was enhanced GFP, or eGFP, but for simplicity inside this dissertation we will refer to eGFP as GFP.

GFP expression stems from the wings.

For imaging we used step sizes of $5\ \mu\text{m}$, and a sampling rate of 500 MSps, which is four times the maximum frequency detected by the detector ($f_c = 78\ \text{MHz}$, $BW = 25 - 125\ \text{MHz}$), after the experiments the signals were reconstructed using three dimensional beamforming with a dynamic aperture, see chapter 5 for more details, this delivers isotropic in-plane resolution, and homogeneous resolution throughout the different planes, the achievable resolution with this transducer is $30\ \mu\text{m}$ in-plane, and $7\ \mu\text{m}$ axially [?].

From the resulting three-dimensional images of the pupae, we took the maximum intensity projection (MIP) along the z -axis and along the y -axis as shown in figure 6.1. On the figure we see several anatomical features, the shape of the pupae, the spiracles, and we observe a strong signal in the middle of the pupae corresponding to the future location of the wings.

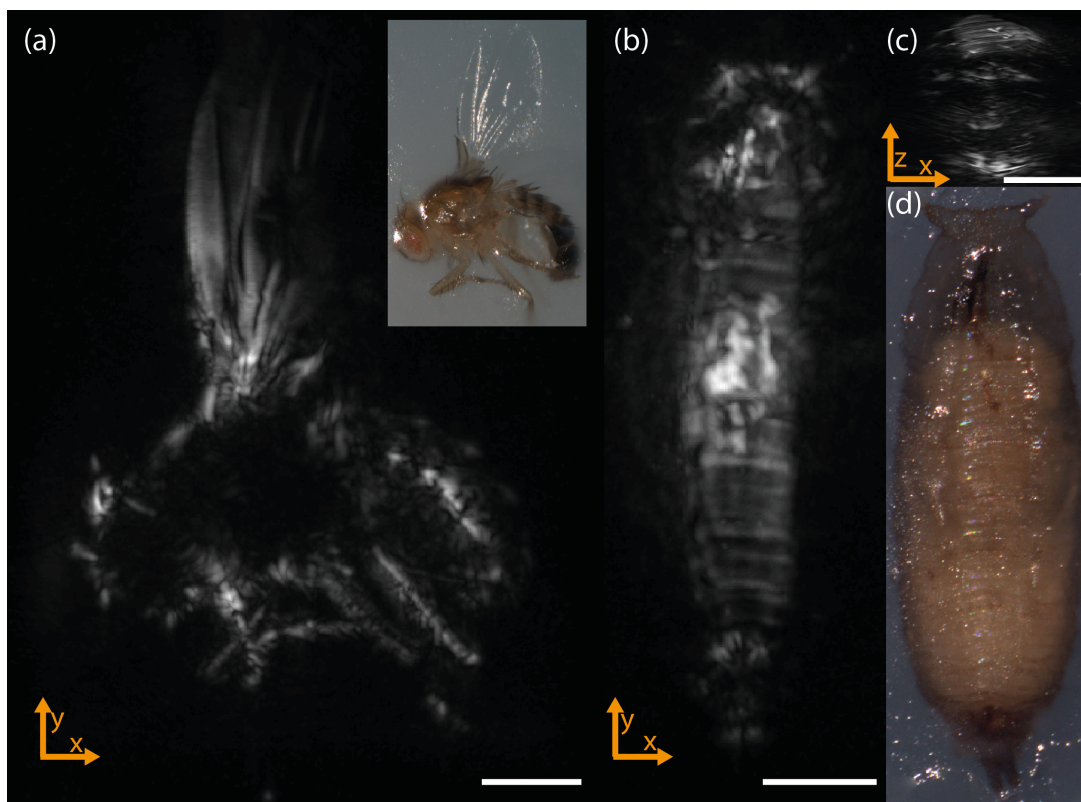


Figure 6.1: Optoacoustic image of a genetically modified fly, the inset shows a photo of the fly(a), and pupae (b, c), photographic image of the pupae. The scale bars are $500\ \mu\text{m}$.

The reconstruction was performed with $dx = dy = 10\ \mu\text{m}$, and $dz = 5\ \mu\text{m}$, coarser discretization will result in aliasing effects as was discussed in section 2.4.3, while finer discretization will result in higher reconstruction times. After reconstruction, interpolating

the reconstructed image, using smaller step sizes will improve the image, at a much lower computational cost.

In the case of the fly, on the MIP we can see many anatomical features, such as the head, the body shape, the legs, and the wings. In the case of the wings, which are transparent usually, the signal comes from the GFP expression, see figure pupaeRSOM.

This study shows the capability of the system in imaging *drosophila melanogaster* pupae, and generate three-dimensional images of the pupae, these capabilities could be used in the future to monitor the development of the wings in the pupal stage. On the other hand, improved performance is still needed in terms of speed of acquisition, and in terms of the capabilities of the system in capturing signals propagating in all directions, which is a disadvantage of limited-view systems, see section 5.5.2.

6.1.3 Imaging of zebrafish

Zebrafish is another tool that developmental biologists, and genetics experimentalists use very often, as in the case of *drosophila melanogaster*, see section 6.1.2, the zebrafish could be easily manipulated, and various phenomena could be studied using the zebrafish. Moreover, because zebrafish belongs to vertebrates, it is much closer to the development of humans than the *drosophila melanogaster*.

The challenge in the case of zebrafish imaging has two reasons:

1. Most of the zebrafish are not transparent, and full of black pigments that strongly absorb light, thus they could be imaged only before they develop those pigments, which is the case for embryos and larvae zebrafish.
2. Zebrafish reaches sizes much larger than what optical microscopy techniques can image, thus the use of optical microscopy techniques is limited either to superficial structures, or to embryonic, and early larval stages of the zebrafish development.

The potential of optoacoustics in imaging post-embryonic, and adult zebrafish has been previously shown by Razansky et al. [109], but again, as in the case of the *drosophila melanogaster*, the resolution was not sufficient to image the details. To improve on that

experiment, we used the second generation of RSOM, with a laser of 532 nm, and an ultrasound detector with a center frequency of 100 MHz, operated in epi-illumination mode, see section 5.4.

We imaged a 1 week old, wild zebrafish³, *ex vivo*. This fish had a diameter of $> 500 \mu\text{m}$. Although this diameter is not large enough, because of the pigmentations on the skin of the zebrafish it is almost impossible to image it with optical microscopy techniques, even with such techniques that can penetrate deeper, like non-linear microscopy. The reason for this being as we previously mentioned the pigments on the skin of the fish, which absorb not only the excitation light, but also the emitted light, being it the fluorescence, or optical harmonics.

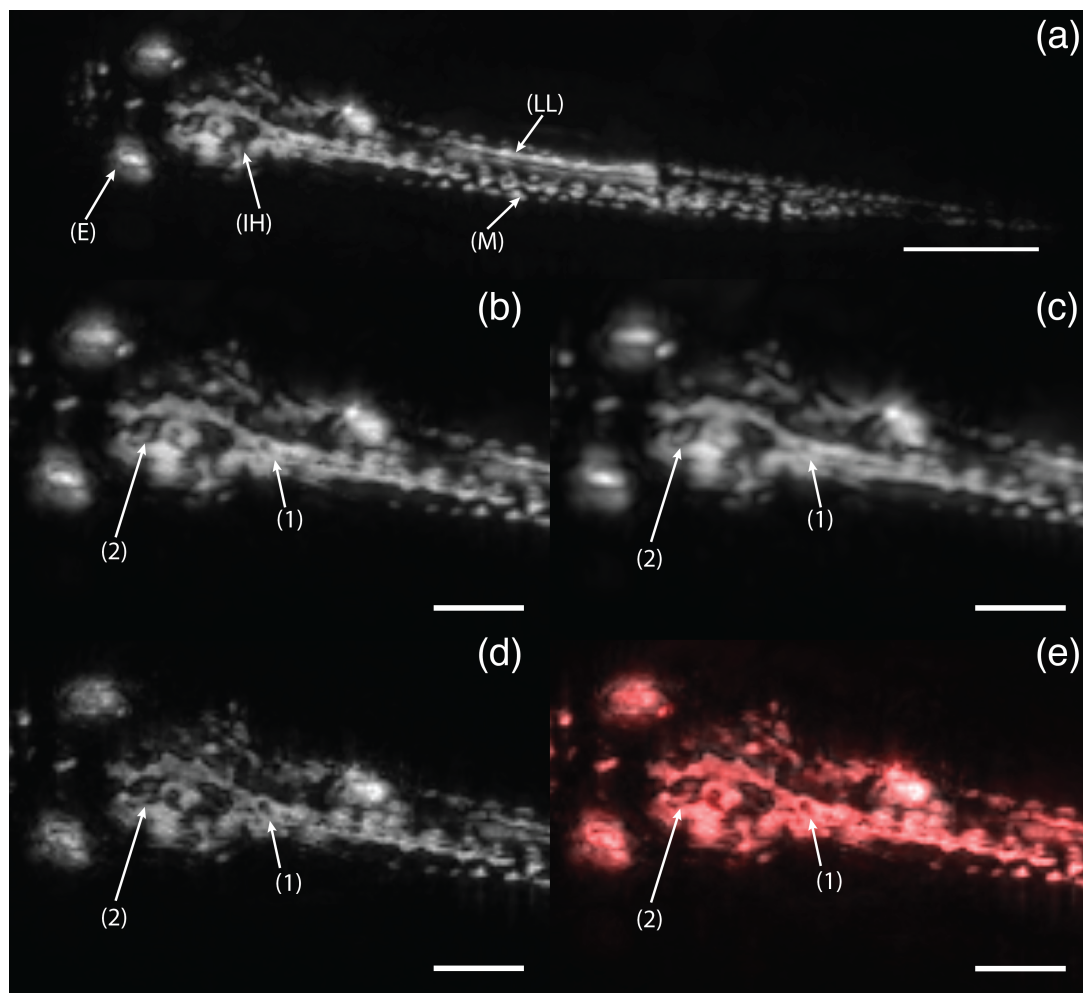


Figure 6.2: Optoacoustic image of a zebrafish (a), zoom-in on the front part of part a (b), same region reconstructed using only the frequencies 20-100 MHz (c), 100-180 MHz (d), an overlay of parts b and d (e). The scale bars are $500 \mu\text{m}$ in (a), and $250 \mu\text{m}$ in the rest.

³We thank Dr. Hernan Lopez-Schier for providing us with the zebrafish.

For the imaging experiments, we performed a raster-scan, with step sizes of $dx = dy = 10 \mu m$, and at a sampling rate of 1 GSps, which is 5-6 times the highest frequency measured by the ultrasound detector, satisfying the Nyquist criteria.

We reconstructed the images using beamforming with a dynamic aperture, which has shown resolutions of $18 \mu m$ transversely, and $4 \mu m$ axially [2], see chapter 5. Moreover, we applied multi-bandwidth reconstruction, where before reconstruction we divided the detection bandwidth into smaller bandwidths, and then reconstructed each of these bandwidths separately. This way we were able to treat the noise in every one of these bandwidths separately, moreover, when reconstructing the high frequencies, which are inherently smaller in amplitude, see section 2.5, we have much less noise in such a way. By doing this we were able to improve the resolution of the final image, and enhance small features that otherwise have been smeared as we will see later in this section [2].

From the three-dimensional reconstruction we took the MIP, which is shown in figure 6.2, in figure 6.2(b) is a zoom in on the front part of the zebrafish, which was reconstructed using the full detection bandwidth, 20-180 MHz, next to it is a reconstruction using the lower half of the bandwidth only, 20-100 MHz, and then comes the reconstruction using only the upper half of the bandwidth, 100-180 MHz. As we can see from the features marked with the numbers 1 and 2, that they look almost similar in the full-bandwidth image, and in the lower half of the bandwidth, while it becomes sharper in the image reconstructed from the upper half of the bandwidth. Overlaying the high-frequency image, over the full-bandwidth image in two different colours, white for high-frequencies, and red for the full-bandwidth image, we generate a new colour scheme, showing both high-frequency features, and large features corresponding to lower frequencies [2].

Looking at the reconstruction of the zebrafish, see figure 6.2, several anatomical features could be spotted, this includes, the eyes, the melanin pigments, the lateral line, and the heart and the intestines.

The images that we have seen show the capabilities of the system in imaging a highly pigmented zebrafish, such a zebrafish would have been difficult to image using a traditional optical microscopy technique, moreover, the system could be used for imaging older fish

as well, moreover *in vivo* measurements could be done if the right protocol is available. Finally using detectors with a high NA or a tomographic system will reveal features that have been obscured in RSOM because of their directionality, and improve the resolution, see section 5.5.2.

6.1.4 Imaging of *Xenopus*

Xenopus is another tool for developmental biologists and many models having been developed around the *Xenopus* [110]. As within the first days of development they are very scattering; it is almost impossible to get any useful images of them using traditional optical microscopy techniques. Because of this we believe that RSOM is a good method to image *Xenopus*⁴. The model developed by Prof. Dr. Ralph Rupp, and his group is based on micro-injection, where at the level of several cells (16-32 cells), one of the cells is injected with a fluorescent probe, as the fate of this cell is already predetermined at this stage, the development of this cell could be then imaged by measuring the signal from the AF546, moreover by altering the genes of the injected cell, it can develop into something else, or could be compromised, and in such a case it's effect on the rest of the *Xenopus* could be studied. It is worth mentioning that although, the fate of the cells is predetermined, it can happen that biology works in a different way, thus micro-injection is more a tool to label certain cells with high probability, rather than an exact tool.

For injection we used Alexa fluor 546 (AF546, SigmaAldrich), which exhibits a peak absorption at 546 nm, which makes it suitable for imaging in RSOM using the 532 nm laser. In the first round of experiments, the cell that is responsible for the generation of heart was injected with AF546.

For imaging, we used *Xenopus* in which a solution with 2.5% of AF546 was injected, and a control *Xenopus*. The *Xenopus* were embedded in low melting agar, 1.3%, and a region of $8 \times 4 \text{ mm}^2$ was scanned at step sizes of $10 \mu\text{m}$, using RSOM100, and RSOM50. From the three-dimensional reconstruction it is observed that in some cases the *Xenopus* exhibits

⁴we thank Prof. Dr. Ralph Rupp for providing us with the *Xenopus*, and we thank Dr. Josefine Reber for organizing the collaboration with Prof. Rupp.

a strong signal from the heart, which is supposed to be full with AF546 as seen in figure 6.3. While the control *Xenopus* exhibits no strong signal from the location of the heart, the *Xenopus* in figure 6.3 where done using RSOM100.

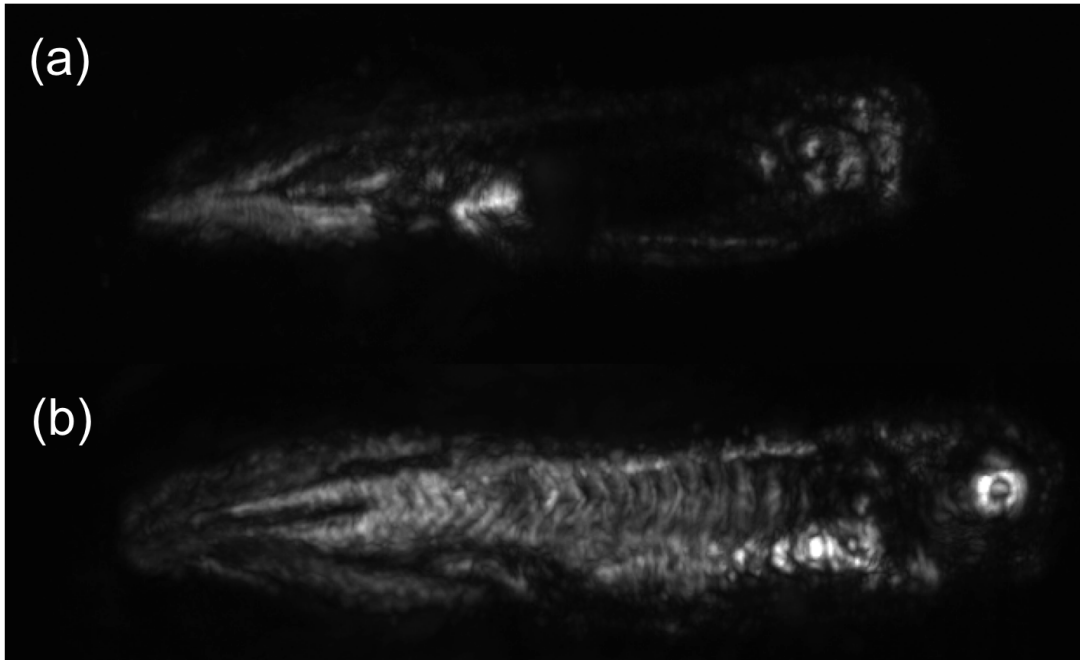


Figure 6.3: Optoacoustic image of a *Xenopus*: control (a), with 2.5% AF546 injected.

6.2 Imaging of the vascular network in a mouse ear

The ear of a mouse is an attractive target for studying the performance of high-resolution optoacoustic systems. Because of the variety in the number and size of vessels inside the mouse ear, where large vessels cross each other at different depths, and large vessels bifurcate into smaller ones. Moreover, the mouse ear with its network of blood vessels, can simulate the micro-environment of some diseases.

Although the mouse ear was imaged several times with optical resolution optoacoustic systems, and with acoustic resolution optoacoustic systems working at 50 MHz, the ultra-wide bandwidth of our detector, $> 100\%$, poses a further challenge. Because of the co-existence of large vessels together with small ones, in the mouse ear, low-frequencies and high-frequencies are generated together, because low frequencies have inherently stronger amplitude than lower frequencies as was previously mentioned, see section 2.5, and they

are less attenuated [41], and thus have a higher SNR , this means that if all the frequencies are reconstructed together, then the small vessels, generating high frequencies, will not appear on the image, and the image will be dominated by low frequency structures.

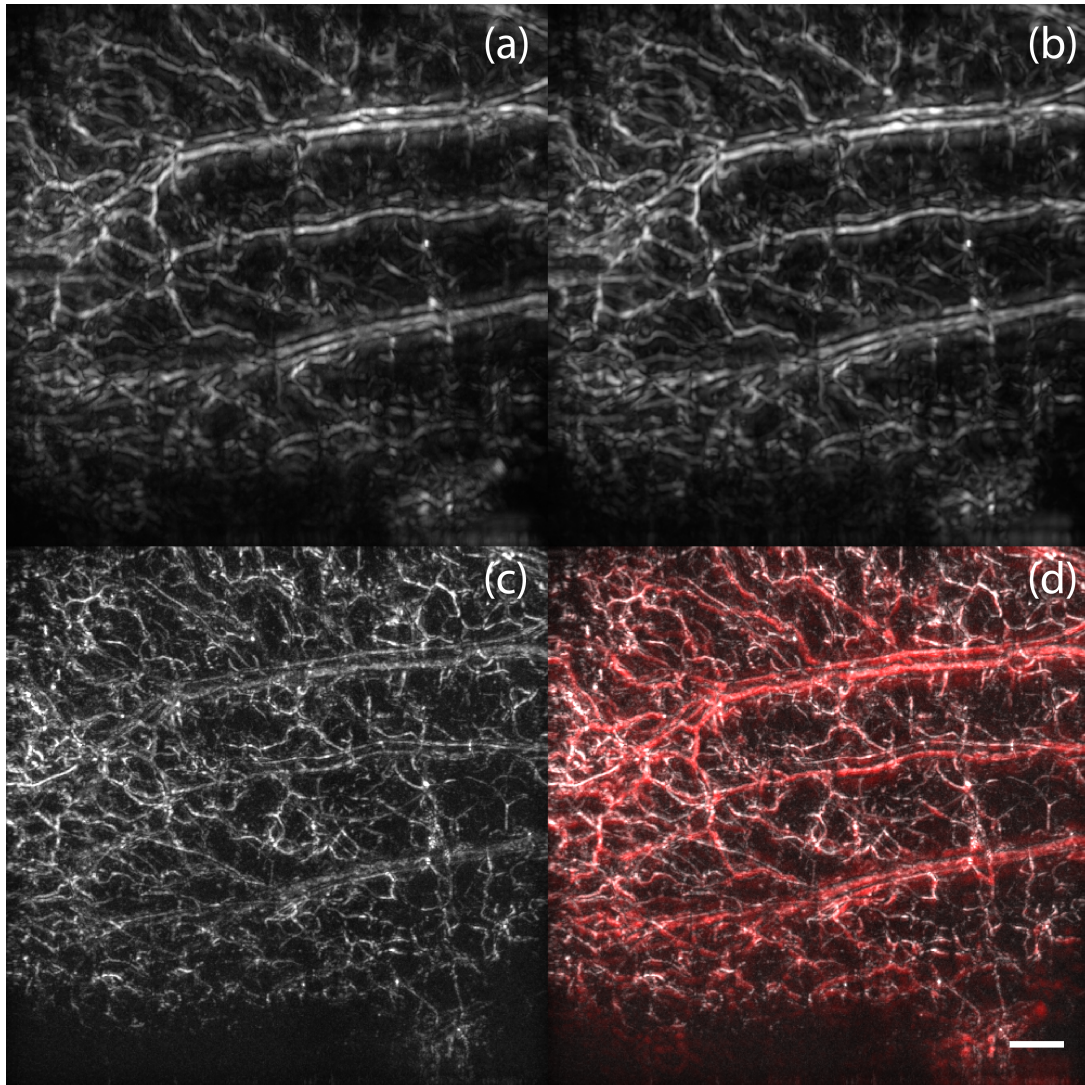


Figure 6.4: Optoacoustic image of an excised mouse ear: (a) all frequencies, (b) low frequencies, (c) high frequencies, (d) overlay of a and c. Scale bar: $500 \mu\text{m}$.

To overcome this, we built over our multi-frequency reconstruction that we used for the reconstruction of the zebrafish, see section 2.5, and section 6.1.3, and as in the case of the zebrafish we divided the wide reception bandwidth into two, the low frequencies: 20-100 MHz, and the high frequencies: 100-180 MHz.

From the different reconstructions, look at figure 6.4, we can observe that the image reconstructed using the full bandwidth of the detector looks very similar to the figure generated using the lower half of the detection bandwidth. The reason for this being the inherently

higher amplitude of the low frequencies, where they are generated from larger structures, thus more energy is generated from a large object. On the other hand, when reconstructing the high-frequencies separately, as seen in figure 6.4, small structures, and tiny microvessels start appearing, which are not seen on the low-frequency image.

Finally, to visualize simultaneously the small structures, together with large structures we use two different color channels, one for every image, which we merge into a single one to generate a hybrid image. In the hybrid image, we have both small structures, and large ones together, where we use white to represent high-frequencies, and red to represent low frequencies, see figure 6.4.

In figure 6.4 some large vessels appear as if they are repeated. In reality, these are two vessels, one of them carries the oxygenated blood and the nutrients, while the other one carries back the deoxygenated blood [97].

6.3 Imaging of Cells

Although cells could be better imaged using optical microscopy techniques, still sometimes we are interested in imaging of cells that are deep inside the tissue, or it is interesting to investigate what kinds of cells could be detected using RSOM. For instance is it better to have cells labeled with GFP or cells labeled with mCherry for imaging?

6.3.1 Imaging of melanin cells

An example of what kind of cells we are interested in is B16F10 melanin cells (ATCC), which are often injected into mice as a model of melanin cancer development.⁵

After defrosting the cells, the cells were embedded into agar, before embedding them we have made a phantom of agar, where we made a vertical tubular hole, and there we injected the mixture of agar with melanin cells, for comparison purposes we have taken 4T1 breast cancer cells, and embedded them in the same way into another agar phantom.

For this measurement we used the first version of RSOM, where a 78 MHz, spherically

⁵We would like to thank Dr. Angelika Zaremba, and Uwe Klemm for helping us in preparation of the cells. The imaging was done together with Dominik Soliman.

focused transducer was used. We scanned a region of $4 \times 4 \text{ mm}^2$, at step sizes of $2.5 \mu\text{m}$. After the scan reconstruction was performed in the bandwidth 25-125 MHz. Finally after reconstruction maximum intensity projection (MIP) of the reconstructed volume was taken, and this was compared with the measurement of 4T1 cells, see figure 6.5.

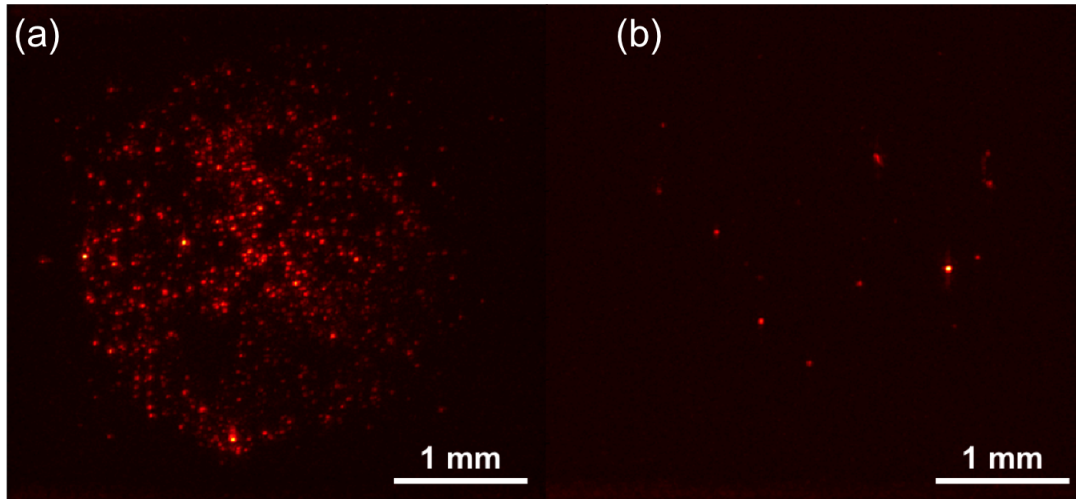


Figure 6.5: Sample with melanin expressing cells (a), control (b).

On the MIP B16F10 cells, which are rich in melanin, give a strong signal, which could be seen from the melanin extinction coefficient, observed in figure 2.2.

6.4 Imaging of tumor development and growth

After demonstrating the capabilities of RSOM in imaging vasculature in the mouse ear, we imaged growth of a melanin tumor using RSOM⁶⁷. The model that we were interested in imaging was a model of melanoma tumor, thus we injected orthotopically B16F10 cells into the mammary fat (0.5×10^6 cells in $25 \mu\text{L}$ PBS solution), of four CD1 nu/nu mice⁸. Subsequently these mice were imaged up to three times, over the course of 8-9 days, to monitor the development of the tumor, and the generation of the vessels around the tumor. Also, melanin tumors are of interest, because of its relation to the different skin diseases.

⁶These imaging sessions were done together with Mathias Schwarz.

⁷This work is currently under review.

⁸Such mice are immune-compromised, which makes them suitable for studying different tumors, and tumor models.

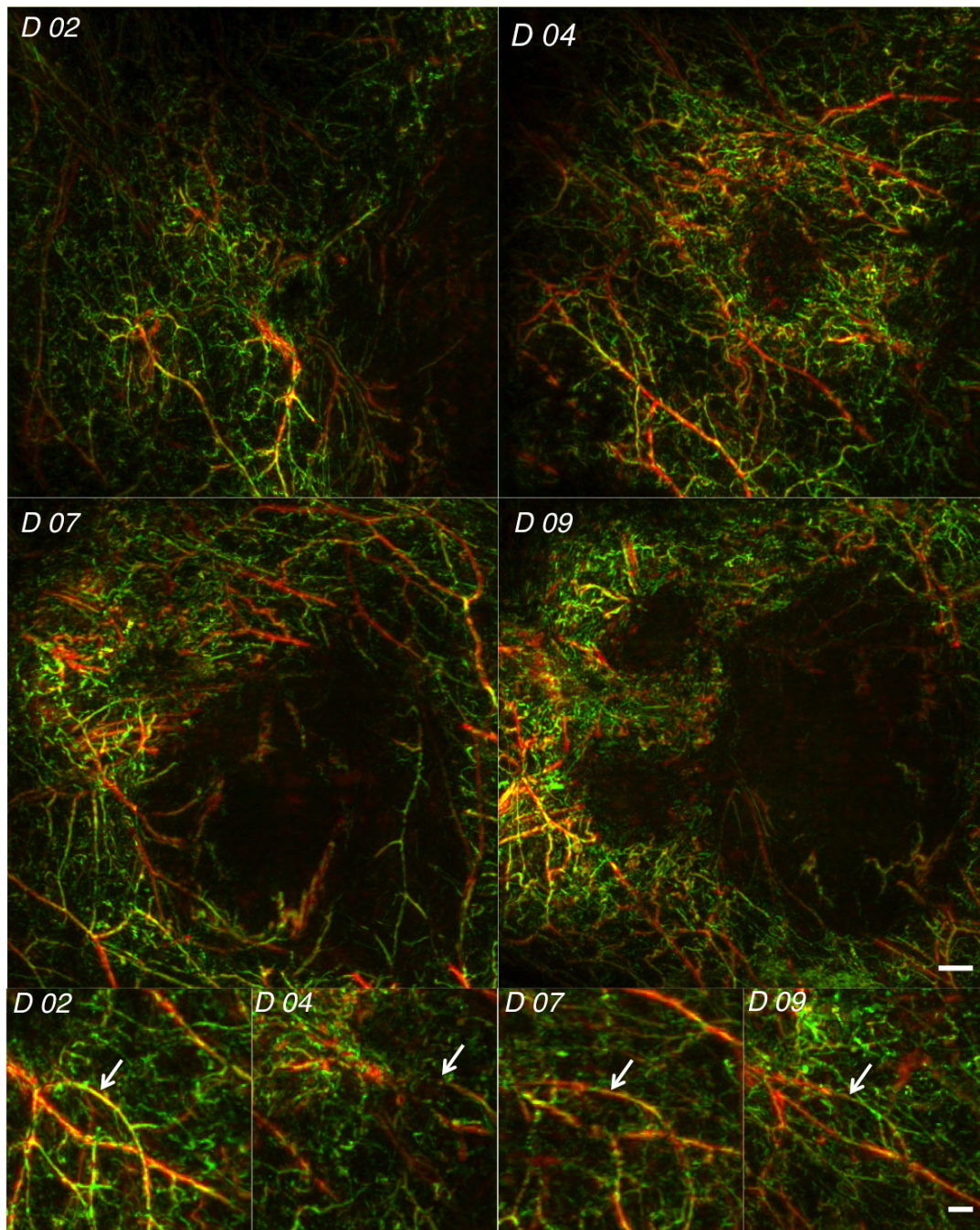


Figure 6.6: Optoacoustic images of tumor growth using RSOM50: The top images show a followup of the tumors growth through days 2, 4, 7, and 9. In these images a MIP from a certain depth. Additionally, the lower row shows a zoom in on the same region, near the tumor, showing an increase in the number of micro-vessels as the tumor grows in size. Green represents the high frequencies, and the red represents the low frequencies. Scalebar: 1 mm for the upper 4 images, and 500 μm for the lowest row.

For imaging we placed the mouse inside a water tank, where the water was regulated at 35°C, this is important in order to keep the temperature of mouse constant. The mice were anesthetized using isoflurane, mixed at around 2-3% with oxygen, and then the mouse was

placed on a special bed, where the head was elevated above water. The mice were placed on their back, and the tumor location was fixed with a handle that has a hole of $20 \times 20 \text{ mm}^2$ inside. On the hole a plastic wrap is placed, both of the holder and the plastic wrap help to keep the tumor stable during the measurement, and decreases the motion artifacts that could be induced from breathing, or heartbeat of the mice. We imaged the mice in two rounds, with two mice in each round [111, 112].

In the first round, RSOM100 was used while in the second round RSOM100 was compared with RSOM50 on the same mice.

An area of $10 \times 10 \text{ mm}^2$ at step sizes of $8 \mu\text{m}$ was scanned using RSOM100, and an area of approximately $15 \times 15 \text{ mm}^2$ at step sizes of $15 \mu\text{m}$ was scanned using RSOM50, resulting in imaging times on the order of a few minutes. Reconstruction was done using three-dimensional beamforming, the detection bandwidth was divided into smaller sub-bands, in such a way that the relative bandwidth is kept constant. The detection bandwidth of RSOM100 was divided into two sub-bands, with each of the sub-bands having a relative bandwidth 100%, the same was done using RSOM50. The different bandwidths were combined into a single image under different color schemes, this way both high frequencies and low frequencies are displayed together. As we have previously seen, if we reconstruct the whole bandwidth at the same time, then the high frequencies are buried under the low frequencies, and small structures smear, see section 2.5.

On the reconstruction, it is possible to observe how the tumor starts developing, starting from small size. Until it becomes a small ball, also it is observed how the vasculature around the tumor starts changing, and how the different vessels go in and out from the tumor [111]. To the best of our knowledge, this is the first time that such images are shown, see figure 6.6.

The images generated from RSOM100 could be co-registered with those generated using RSOM50, this would help in showing high-resolution images of RSOM100 together with larger field-of-view (FOV) images generated from RSOM50. RSOM50 is capable of penetrating deeper inside biological tissues because the lower frequencies are less attenuated than higher-frequencies. For co-registration some hallmarks on both images are located,

on the other side. To make sure that the same region is scanned in both experiments, the detector is changed while the mouse remains inside the same holder. This way fewer motion artifacts are induced, and there is no shift or rotation of the scanned region, see figure 6.7.

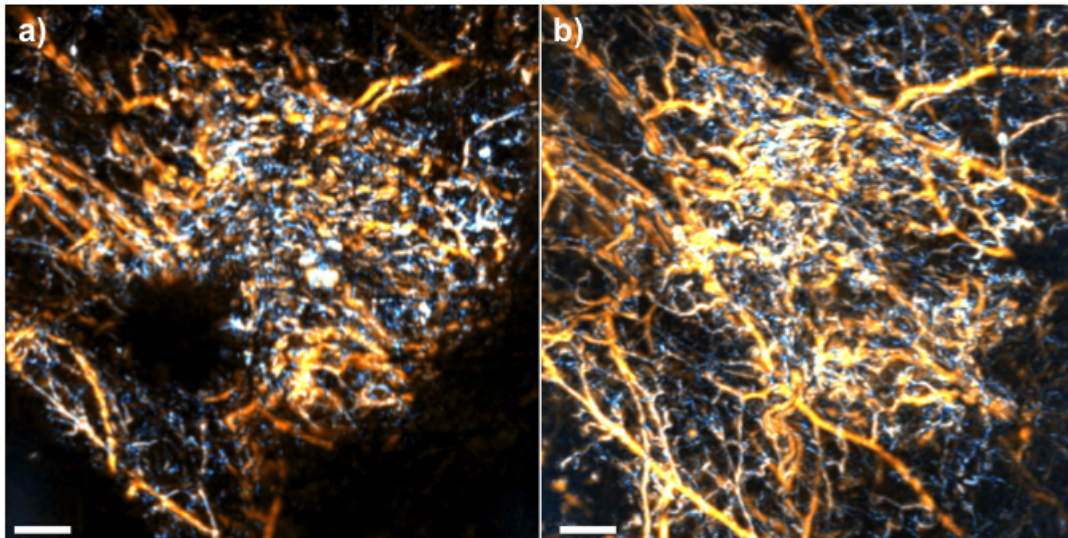


Figure 6.7: Comparison of a tumor image using (a) RSOM100, and (b) RSOM50. Cyan hot represents the high frequencies, and orange hot represents the low frequencies. Scalebar: 1 mm

Improvements on these images could be done by using two wavelengths, 515 nm, and 532 nm. For example, this would allow the generation of oxy/deoxy maps of hemoglobin in the vasculature around the tumor.

6.5 Imaging of skin

In the quest to for imaging skin diseases, such as skin cancer, many systems and methods were developed, such as optical coherence tomography (OCT), multiphoton microscopy, and other systems. In our lab, we are trying to do this with RSOM. The reason being the ability of RSOM in imaging blood vasculature, as well as the ability of RSOM in detecting melanin cells as we have seen in section 6.3 and section 6.4. For imaging a special holder with a hole in the middle, where a plastic foil has been secured was designed, similar to the one used for imaging tumor development in mice, see section 6.4. This procedure

helped in flattening the skin, as well as in keeping the skin part being imaged from moving relatively to the detector. Those images revealed with very high resolution skin layers, such as the dermis, the epidermis, the horizontal plexus, and the dermal papillae [113, 114].

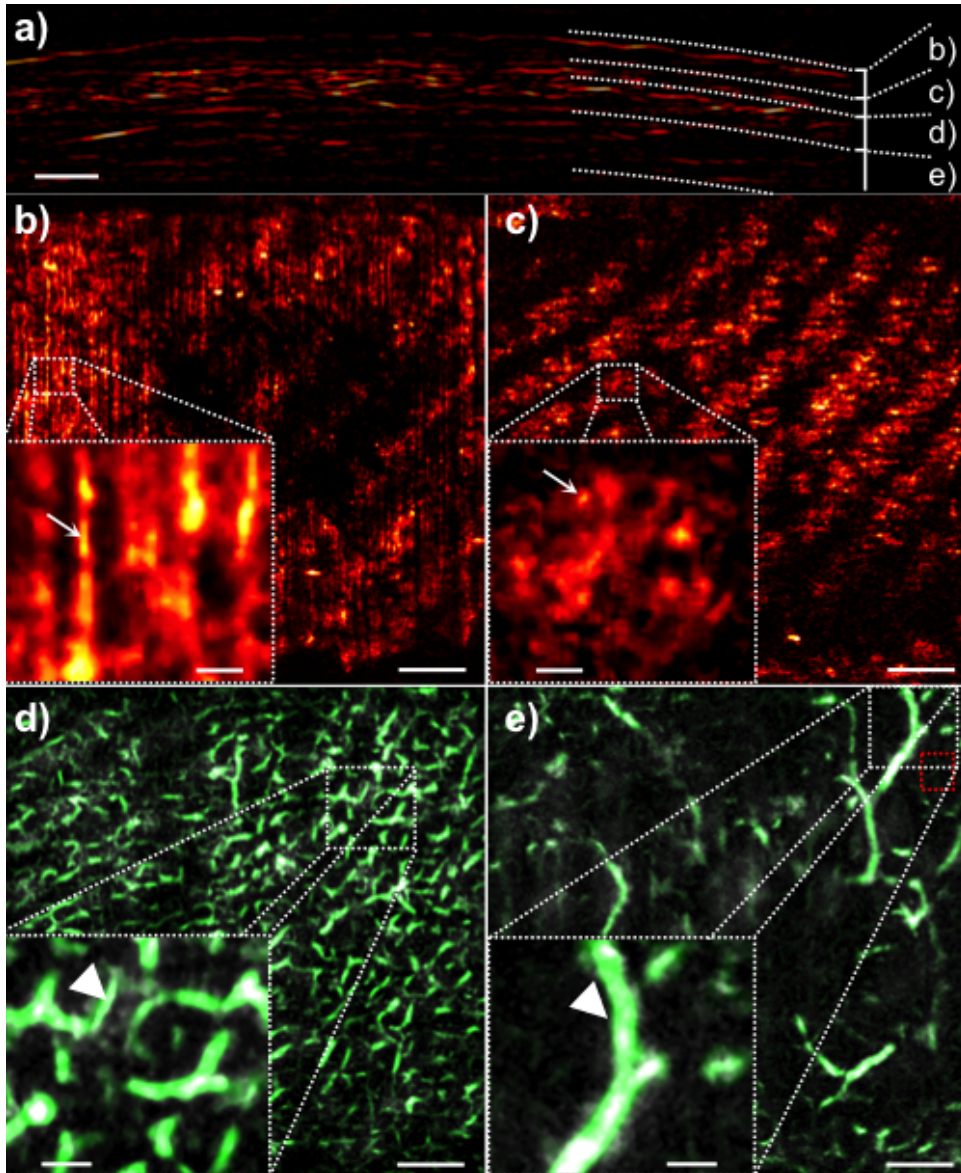


Figure 6.8: Different layers of human skin. a) Cross section through human skin. (b-e) show maximum amplitude projections along the depth direction within the regions marked in (a). b) epidermis (0-150 μm), c) dermal papillae (150-300 μm), d) sub-papillary plexus (300-555 μm), e) deep vessels of the sub-papillary plexus or the intermediate venous plexus of the dermis (555-975 μm). In (b-e) a zoom in into the region marked by the white dashed box is shown. The FWHM of the line-like or point-like structures marked by the white arrows in each sub-figure were calculated to be: 27.5 μm (b), 35 μm (c), 55 μm (d), and 87.5 μm (e). In (d,e) the original image (white) is with an image filtered for vessels in green. The SNR of the vessel marked by the red arrow with respect to the background marked by the red box in (e) in the unfiltered image is 12 dB. The scale bars are a) 500 μm , b,c) 1 mm, and 100 μm in the insets, d,e) 1 mm, and 250 μm in the insets

Looking at the generated images, at several depths reveals the capability of the system in imaging the large vessels in the horizontal plexus, from which small capillaries ascend to the epidermal-dermal junction, this forms the capillary loops which supplies the skin with nutrition and oxygen [113, 114], see figure 6.8.

6.6 Summary, and discussion

In this chapter, we have seen various applications of raster-scan optoacoustic mesoscopy (RSOM); possibility for such applications has been enabled by the technologies behind RSOM, see chapter 3. We have seen how RSOM was capable of generating high resolution images of the distribution of GFP in a *drosophila melanogaster* pupae, in three dimensions, additionally RSOM was capable of imaging other model organisms such as the *Xenopus*, and the zebrafish.

In addition to model organisms, RSOM has shown its potential in imaging tumor development, at high resolutions, where a model of melanin tumor was induced inside a mouse by injecting B16F10 cells orthotopically. As the tumor grew, it was possible to see a black hole, surrounded with a network of micro-vasculature, which works as a feeding network for the tumor. Thus, RSOM was capable of revealing for the first time, at such a high-resolution the vascular network feeding the tumor. This capability could be coupled with other models to study tumor dynamics, as well as tumor treatment.

Finally RSOM has shown big potential in studying skin, and revealed the different skin layers, RSOM didn't only generated high resolution images of these different skin layers, it has shown for the first time the different frequencies that are generated in the different layers of the skin [113, 114].

As RSOM develops we expect it to find its way to more and more applications, and to infiltrate more laboratories, and the clinics, to facilitate this we expect further advancements in terms of technology, such as ultrasonic detection, and laser excitation, add to this the possibility to couple RSOM to other technologies, such as multiphoton microscopy, and op-

toacoustic microscopy [92]. We also expect that the scanning capabilities will improve the imaging capabilities, where either more detectors are used in parallel for increased speed, and increased angular coverage, also tomographic RSOM, or MORSOM should enable us to deliver better images of model organisms.

The major hurdles in terms of applications at the moment are:

1. Finding the right protocols for RSOM to get into the clinics, although some first trials on human volunteers are happening, RSOM can only become a potent method if it is tested in the clinics, and on real patients.
2. Finding the best parameters for imaging and image processing with RSOM, this should not only improve the scanning times, but also generate the best possible images.
3. Finding the right biological questions, and the right biological applications for RSOM, where other methods such as multiphoton microscopy, or optical coherence tomography have no answer, if such an application, or applications, are found then RSOM will be more common in the future.

If these hurdles are solved, then we believe RSOM will be able to help in solving several biological questions.

Chapter 7

Future and outlook

During this work we designed, built, and characterized several systems, both macroscopic, and mesoscopic, all based on the thermoacoustic effect. The main objective was to push the boundaries of spatial resolution, at reasonable depths of penetration. This capability is important for studying biological processes, in experimental animal models.

The RF-thermoacoustics system, presented in chapter 4, has enabled for the first time, high resolution imaging of the electromagnetic energy distribution within biological tissues. This system gives a unique opportunity to image disease biomarkers, with higher resolution, from deep within biological tissues. For example, this could be used to detect breast cancer, where the electrical properties of cancer are different than those of the surrounding healthy tissue.

In the future it is planned to develop a real-time version of the system, which will enable both real-time pre-clinical, and clinical applications. The current system will benefit in the future from better detectors, such as optical detectors which are immune to the electromagnetic interference generated by the pulse generator.

We have also developed several versions of an optoacoustic mesoscopic system, which we call raster scan optoacoustic mesoscopy (RSOM). In the first version we developed a trans-illumination system, which is suitable for imaging of thin samples. To adapt the system for thicker samples, such as monitoring the development of tumors in mice, we devel-

oped an epi-illumination system based on a custom designed ultrasonic detector. Finally, to adapt the system for model organisms used in developmental biology, and experimental genetics, we developed a multi-view (orientation) version of the system, suitable for imaging cylindrically shaped organisms, like zebrafish. This enables us to image the sample from all the directions, effectively eliminating the limited view problem. In all the cases, we achieved higher resolutions than what was previously available, reaching resolutions of 4-20 μm , at depths of field of several millimeters inside of biological tissues.

The system in all its configurations have been successfully used to image model organisms, cells, and tumor's growth and angiogenesis in mice. Additionally, clinical applications such as skin imaging are coming up.

The new capabilities will enable several applications, among the most important ones, would be high resolution imaging of cancer models *in vivo*, imaging of cancer therapy sessions, imaging the development in model organisms, and other applications.

To fuel the rise of high resolution, laser thermoacoustics, or RSOM in biomedical imaging, several technological hurdles needs to be solved; first new laser lines needs to be developed, or additional laser lines needs to be added for multicolor imaging, thus enable imaging of multiple biomarkers simultaneously. These new capabilities will increase the sensitivity, and dynamic properties such such as blood oxygenation could be measured. Additionally, lasers with a higher repetition rate will enable faster imaging of the samples. On the other hand, developments in the detection technology, such as a move to optical detectors, will enable miniaturization of the detectors. This way, detector arrays with high sensitivity will be possible, additionally the detectors will have a relatively flat frequency response. Thus, multi-scale imaging, with the same detector will be possible.

To re-iterate what we mentioned in the last chapter, the major hurdles in terms of applications for RSOM at the moment are:

1. Finding the right biological questions, and the right biological applications for RSOM, where other methods such as multiphoton microscopy, or optical coherence tomography have no answer, if such an application, or applications, are found then RSOM will be more common in the future.

2. Finding the right protocols for RSOM to get into the clinics, although some first trials on human volunteers are happening, RSOM can only become a potent method if it is tested in the clinics, and on real patients.
3. Finding the best parameters for imaging and image processing with RSOM, this should not only improve the scanning times, but also generate the best possible images.

If these hurdles are solved, then we believe RSOM will be able to help in solving several biological questions.

Finally, we expect in the future further advancements, and adaptations of all the systems designed, and built during this dissertation, for RF-thermoacoustics we expect to do the first real-time imaging, as for the laser-thermoacoustics we expect to go for faster, multi-color imaging. Additionally, we expect to improve the reconstruction times, and our image processing capabilities.

Appendix A

List of publications

Journal papers:

Murad Omar*, Johannes Rebling*, Kai Wicker*, Tobias Schmitt-Manderbach, Mathias Schwarz, Jerome Gateau, Hernan Lopez-Schier, Timo Mappes, and Vasilis Ntziachristos, *Imaging of post-embryonic zebrafish using multi-orientation raster scan optoacoustic mesoscopy (MO-RSOM)*, under review

Dominik Soliman*, Antonella Lauri*, **Murad Omar**, Gil Westmeyer, and Vasilis Ntziachristos. *Volumetric detection of melanophore pigment translocation by in vivo optoacoustic imaging and frequency mapping*, in preparation

Dominik Soliman*, George Tserevelakis*, **Murad Omar**, and Vasilis Ntziachristos, *Combining microscopy with mesoscopy using optical and optoacoustic label-free modes*, Scientific Reports 5, 12902 (2015)

Murad Omar*, Mathias Schwarz*, Dominik Soliman, Panagiotis Symvoulidis, and Vasilis Ntziachristos, *Pushing the Optical Imaging Limits of Cancer with Multi-Frequency-Band Raster-Scan Optoacoustic Mesoscopy (RSOM)*, Neoplasia 17(2), 208-214(2015)

Hsiao-Chun Amy Lin*, Andrei Chekkoury*, **Murad Omar***, Tobias Schmitt-Manderbach, Timo Mappes, Hernan Lopez-Schier, Daniel Razansky, and Vasilis Ntziachristos, *Selective plane illumination optical and optoacoustic microscopy for postembryonic imaging*, Laser and Photonics Reviews 9(5), L29-L34(2015)

Mathias Schwarz, **Murad Omar**, Andreas Buehler, Juan Aguirre, and Vasilis Ntziachristos, *Implications of ultrasound frequency in optoacoustic mesoscopy of the skin*, Medical Imaging, IEEE Transactions on 34(2), 672-677(2015)

W Assmann, S Kellnberger, S Reinhardt, S Lehrack, A Edlich, PG Thirolf, M Moser, G Dollinger, **M Omar**, V Ntziachristos, K Parodi, *onoacoustic characterization of the proton Bragg peak with submillimeter accuracy*, Medical Physics 42(2), 567-574(2015)

Juan Aguirre, Mathias Schwarz, Dominik Soliman, Andreas Buehler, **Murad Omar**, and Vasilis Ntziachristos, *Broadband mesoscopic optoacoustic tomography reveals skin layers*, Optics Letters 39(21), 6297-6300(2104)

Murad Omar, Dominik Soliman, Jerome Gateau, and Vasilis Ntziachristos, *Ultrawide-band reflection-mode optoacoustic mesoscopy*, Optics Letters 39(13), 3911-3914(2014)

Amir Rosenthal, Stephan Kellnberger, **Murad Omar**, Daniel Razansky, and Vasilis Ntziachristos, *Wideband Optical Detector of Ultrasound for Medical Imaging Applications*, JoVE e50847 (2014)

Amir Rosenthal, Stephan Kellnberger, Dmitry Bozhko, Andrei Chekkoury, **Murad Omar**, Daniel Razansky, and Vasilis Ntziachristos, *Sensitive interferometric detection of ultrasound for minimally invasive clinical imaging applications*, Laser and Photonics Reviews 8(3), 450-457 (2014)

George J. Tserevelakis*, Dominik Soliman*, **Murad Omar**, and Vasilis Ntziachristos, *Hybrid multiphoton and optoacoustic microscope*, Opt. Lett. 39(7), 1819-1822 (2014)

Amir Rosenthal, **Murad Omar**, Hector Estrada, Stephan Kellnberger, Daniel Razansky, and Vasilis Ntziachristos, *Embedded ultrasound sensor in a silicon-on-insulator photonic platform*, Applied Physics Letters 104(2), 021116 (2014)

Stephan Kellnberger*, **Murad Omar***, George Sergiadis, and Vasilis Ntziachristos, *Second harmonic acoustic responses induced in matter by quasi continuous radiofrequency fields*, Applied Physics Letters 103(15), 153706 (2013)

Murad Omar, Jerome Gateau, and Vasilis Ntziachristos, *Raster-scan optoacoustic mesoscopy in the 25-125 MHz range*, Opt. Lett. 38(14), 2472-2474 (2013)

Murad Omar, Stephan Kellnberger, George Sergiadis, Daniel Razansky, and Vasilis Ntziachristos, *Near-field thermoacoustic imaging with transmission line pulsers*, Med. Phys. 39(7), 4460-4466 (2012)

*equal contribution.

Conference proceedings:

M. Omar, D. Soliman, J. Gateau, and V. Ntziachristos, *High-resolution epi-illumination raster-scan optoacoustic mesoscopy for imaging of model organisms and microvessels*, European Conference on Biomedical Optics, 95390U-95390U-6

D. Soliman, GJ Tserevelakis, **M. Omar** and V. Ntziachristos, *Hybrid label-free multiphoton and optoacoustic microscopy (MPOM)*, European Conference on Biomedical Optics, 953908-953908-6

M. Schwarz, J. Aguirre, A. Buehler, **M. Omar** and V. Ntziachristos, *Visualization of the microcirculatory network in skin by high frequency optoacoustic mesoscopy*, European Conference on Biomedical Optics, 95390J-95390J-6

M. Omar, D. Soliman, J. Gateau, and V. Ntziachristos, *Retrieving small features in reflection-mode raster-scan optoacoustic mesoscopy (RSOM) using multi-frequency reconstruction*, SPIE BiOS, 932326, 932326-6 (2015)

S Reinhardt, W Assmann, S Kellnberger, **M Omar**, A Fink, C Gaebisch, P Thirolf, M Moser, G Dollinger, G Sergiadis, V Ntziachristos, K Parodi, *WE-D-BRF-02: Acoustic signal from the Bragg peak for range verification in proton therapy*, Medical Physics 41(6), 495-495(2015)

M. Omar, J. Gateau, and V. Ntziachristos, *High-resolution raster scan optoacoustic mesoscopy of genetically modified drosophila pupae*, Proc. of SPIE, Vol. 8943, 89431F-7 (2014)

M. Omar, S. Kellnberger, G. Sergiadis, D. Razansky, and V. Ntziachristos, *Transmission line based thermoacoustic imaging of small animals*, European Conference on Biomedical Optics, 88000D-5 (2013)

M. Omar, S. Kellnberger, G. Sergiadis, D. Razansky, and V. Ntziachristos, *Near-field radio-frequency thermo-acoustic imaging based on transmission lines for optimised performance*, Proc. of SPIE, Vol. 8223, 82231O-1 (2012)

Talks:

M. Omar, D. Soliman, J. Gateau, and V. Ntziachristos, *Retrieving small features in reflection-mode raster-scan optoacoustic mesoscopy (RSOM) using multi-frequency reconstruction*, Photons Plus Ultrasound, SPIE Photonics West 2015, San Francisco, California, U.S.A., 10.Feb.2015

M. Omar, J. Gateau, and V. Ntziachristos, *High-resolution raster scan optoacoustic mesoscopy of genetically modified drosophila pupae*, Photons Plus Ultrasound, SPIE Photonics West 2014, San Francisco, California, U.S.A., 03.Feb.2014

M. Omar, J. Gateau, and V. Ntziachristos, *Non-invasive 3-dimensional imaging of drosophila pupae and fly using raster-scan optoacoustic mesoscopy (R-SOM)*, TOPIM 2014, Les Houches, France, 23.Jan.2014

M. Omar, J. Gateau, and V. Ntziachristos, *3-Dimensional high resolution imaging of molecular markers using optoacoustic mesoscopy*, Molekulare Bildgebung, Heidelberg, Germany, 29.Oct.2013

M. Omar, S. Kellnberger, G. Sergiadis, D. Razansky, and V. Ntziachristos, *Near-field radio-frequency thermo-acoustic imaging based on transmission lines for optimised performance*, Photons Plus Ultrasound, SPIE Photonics West 2012, San Francisco, California, U.S.A., 23.Jan.2012

Patents:

Stephan Kellnberger, Vasilis Ntziachristos, George Sergiadis, Nikolaus Deliolanis, **Murad Omar**, *Apparatus and method for frequency-domain thermo-acoustic tomographic imaging*, Patent application, No. WO 2013167147 A1

Bibliography

- [1] S. Gabriel, R. Lau, and C. Gabriel, "The dielectric properties of biological tissues: Iii. parametric models for the dielectric spectrum of tissues," *Physics in medicine and biology*, vol. 41, no. 11, p. 2271, 1996.
- [2] M. Omar, D. Soliman, J. Gateau, and V. Ntziachristos, "Ultrawideband reflection-mode optoacoustic mesoscopy," *Optics letters*, vol. 39, no. 13, pp. 3911–3914, 2014.
- [3] E. C. Fear, X. Li, S. C. Hagness, and M. A. Stuchly, "Confocal microwave imaging for breast cancer detection: Localization of tumors in three dimensions," *Biomedical Engineering, IEEE Transactions on*, vol. 49, no. 8, pp. 812–822, 2002.
- [4] E. J. Bond, X. Li, S. C. Hagness, and B. D. Van Veen, "Microwave imaging via space-time beamforming for early detection of breast cancer," *Antennas and Propagation, IEEE Transactions on*, vol. 51, no. 8, pp. 1690–1705, 2003.
- [5] X. Li, E. J. Bond, B. D. Van Veen, and S. C. Hagness, "An overview of ultra-wideband microwave imaging via space-time beamforming for early-stage breast-cancer detection," *Antennas and Propagation Magazine, IEEE*, vol. 47, no. 1, pp. 19–34, 2005.
- [6] W. Denk, J. H. Strickler, and W. W. Webb, "Two-photon laser scanning fluorescence microscopy," *Science*, vol. 248, no. 4951, pp. 73–76, 1990.
- [7] F. Helmchen and W. Denk, "Deep tissue two-photon microscopy," *Nature methods*, vol. 2, no. 12, pp. 932–940, 2005.

- [8] J. Huisken, J. Swoger, F. Del Bene, J. Wittbrodt, and E. H. Stelzer, "Optical sectioning deep inside live embryos by selective plane illumination microscopy," *Science*, vol. 305, no. 5686, pp. 1007–1009, 2004.
- [9] J. Huisken and D. Y. Stainier, "Selective plane illumination microscopy techniques in developmental biology," *Development*, vol. 136, no. 12, pp. 1963–1975, 2009.
- [10] V. Ntziachristos, A. Yodh, M. Schnall, and B. Chance, "Concurrent mri and diffuse optical tomography of breast after indocyanine green enhancement," *Proceedings of the National Academy of Sciences*, vol. 97, no. 6, pp. 2767–2772, 2000.
- [11] V. Ntziachristos, C.-H. Tung, C. Bremer, and R. Weissleder, "Fluorescence molecular tomography resolves protease activity in vivo," *Nature medicine*, vol. 8, no. 7, pp. 757–761, 2002.
- [12] A. Ale, V. Ermolayev, E. Herzog, C. Cohrs, M. H. de Angelis, and V. Ntziachristos, "Fmt-xct: in vivo animal studies with hybrid fluorescence molecular tomography-x-ray computed tomography," *Nature methods*, vol. 9, no. 6, pp. 615–620, 2012.
- [13] V. Ntziachristos, "Going deeper than microscopy: the optical imaging frontier in biology," *Nature methods*, vol. 7, no. 8, pp. 603–614, 2010.
- [14] T. Bowen, "Radiation-induced thermoacoustic soft tissue imaging," in *1981 Ultrasonics Symposium*, pp. 817–822, IEEE, 1981.
- [15] A. A. Oraevsky, S. L. Jacques, and F. K. Tittel, "Determination of tissue optical properties by piezoelectric detection of laser-induced stress waves," in *OE/LASE'93: Optics, Electro-Optics, & Laser Applications in Science & Engineering*, pp. 86–101, International Society for Optics and Photonics, 1993.
- [16] L. V. Wang, X. Zhao, H. Sun, and G. Ku, "Microwave-induced acoustic imaging of biological tissues," *Review of Scientific Instruments*, vol. 70, no. 9, pp. 3744–3748, 1999.

- [17] R. A. Kruger, P. Liu, C. R. Appledorn, *et al.*, “Photoacoustic ultrasound (paus)?reconstruction tomography,” *Medical physics*, vol. 22, no. 10, pp. 1605–1609, 1995.
- [18] M. Omar, S. Kellnberger, G. Sergiadis, D. Razansky, and V. Ntziachristos, “Near-field thermoacoustic imaging with transmission line pulsers,” *Medical physics*, vol. 39, no. 7, pp. 4460–4466, 2012.
- [19] L. V. Wang, *Photoacoustic imaging and spectroscopy*. CRC press, 2009.
- [20] M. Xu and L. V. Wang, “Photoacoustic imaging in biomedicine,” *Review of scientific instruments*, vol. 77, no. 4, p. 041101, 2006.
- [21] C. Li and L. V. Wang, “Photoacoustic tomography and sensing in biomedicine,” *Physics in medicine and biology*, vol. 54, no. 19, p. R59, 2009.
- [22] P. Mohajerani, S. Kellnberger, and V. Ntziachristos, “Frequency domain optoacoustic tomography using amplitude and phase,” *Photoacoustics*, 2014.
- [23] S. Kellnberger, N. C. Deliolanis, D. Queirós, G. Sergiadis, and V. Ntziachristos, “In vivo frequency domain optoacoustic tomography,” *Optics letters*, vol. 37, no. 16, pp. 3423–3425, 2012.
- [24] P. Mohajerani, S. Kellnberger, and V. Ntziachristos, “Fast fourier backprojection for frequency domain optoacoustic tomography,”
- [25] L. V. Wang and H.-i. Wu, *Biomedical optics: principles and imaging*. John Wiley & Sons, 2012.
- [26] J. D. Jackson, *Classical electrodynamics*. John Wiley & Sons, 3 ed., 1998.
- [27] C. A. Balanis, *Advanced engineering electromagnetics*. Wiley New York, 1 ed., 1989.
- [28] M. H. Sadd, *Elasticity: theory, applications, and numerics*. Academic Press, 2014.

- [29] C. Gabriel, S. Gabriel, and E. Corthout, "The dielectric properties of biological tissues: I. literature survey," *Physics in medicine and biology*, vol. 41, no. 11, p. 2231, 1996.
- [30] S. Gabriel, R. Lau, and C. Gabriel, "The dielectric properties of biological tissues: li. measurements in the frequency range 10 hz to 20 ghz," *Physics in medicine and biology*, vol. 41, no. 11, p. 2251, 1996.
- [31] A. Rosenthal, V. Ntziachristos, and D. Razansky, "Acoustic inversion in optoacoustic tomography: A review," *Current medical imaging reviews*, vol. 9, no. 4, p. 318, 2013.
- [32] M. Xu and L. V. Wang, "Universal back-projection algorithm for photoacoustic computed tomography," *Physical Review E*, vol. 71, no. 1, p. 016706, 2005.
- [33] M. I. Skolnik, *Introduction to RADAR systems*. McGraw Hill, 2001.
- [34] X. L. Dean-Ben, R. Ma, D. Razansky, and V. Ntziachristos, "Statistical approach for optoacoustic image reconstruction in the presence of strong acoustic heterogeneities," *Medical Imaging, IEEE Transactions on*, vol. 30, no. 2, pp. 401–408, 2011.
- [35] M.-L. Li, H. F. Zhang, K. Maslov, G. Stoica, and L. V. Wang, "Improved in vivo photoacoustic microscopy based on a virtual-detector concept," *Optics letters*, vol. 31, no. 4, pp. 474–476, 2006.
- [36] M. Omar, J. Gateau, and V. Ntziachristos, "Raster-scan optoacoustic mesoscopy in the 25-125 mhz range," *Optics Letters*, vol. 38, no. 14, pp. 2472–2474, 2013.
- [37] R. S. Cobbold, *Foundations of biomedical ultrasound*. Oxford University Press, USA, 2007.
- [38] J. Yao, K. I. Maslov, E. R. Puckett, K. J. Rowland, B. W. Warner, and L. V. Wang, "Double-illumination photoacoustic microscopy," *Optics letters*, vol. 37, no. 4, pp. 659–661, 2012.
- [39] C. Zhang, "Submicron-resolution photoacoustic microscopy of endogenous light-absorbing biomolecules," 2014.

- [40] J. Yao and L. V. Wang, "Sensitivity of photoacoustic microscopy," *Photoacoustics*, vol. 2, no. 2, pp. 87–101, 2014.
- [41] X. L. Deán-Ben, D. Razansky, and V. Ntziachristos, "The effects of acoustic attenuation in optoacoustic signals," *Physics in medicine and biology*, vol. 56, no. 18, p. 6129, 2011.
- [42] S. Mallat, *A wavelet tour of signal processing*. Academic press, 1999.
- [43] "Wavelet transform, wikipedia," July 2014.
- [44] "Discrete wavelet transform, wikipedia," July 2014.
- [45] S. P. Ghael, A. M. Sayeed, and R. G. Baraniuk, "Improved wavelet denoising via empirical wiener filtering," in *Optical Science, Engineering and Instrumentation'97*, pp. 389–399, International Society for Optics and Photonics, 1997.
- [46] L. J. Hadjileontiadis, "A novel technique for denoising explosive lung sounds; empirical mode decomposition and fractal dimension filter," *Engineering in Medicine and Biology Magazine, IEEE*, vol. 26, no. 1, pp. 30–39, 2007.
- [47] I. Ladabaum, X. Jin, H. T. Soh, A. Atalar, and B. Khuri-Yakub, "Surface micromachined capacitive ultrasonic transducers," *Ultrasonics, Ferroelectrics and Frequency Control, IEEE Transactions on*, vol. 45, no. 3, pp. 678–690, 1998.
- [48] O. Oralkan, A. S. Ergun, J. A. Johnson, M. Karaman, U. Demirci, K. Kaviani, T. H. Lee, and B. T. Khuri-Yakub, "Capacitive micromachined ultrasonic transducers: Next-generation arrays for acoustic imaging?," *Ultrasonics, Ferroelectrics and Frequency Control, IEEE Transactions on*, vol. 49, no. 11, pp. 1596–1610, 2002.
- [49] X. Jin, I. Ladabaum, and B. T. Khuri-Yakub, "The microfabrication of capacitive ultrasonic transducers," *Microelectromechanical Systems, Journal of*, vol. 7, no. 3, pp. 295–302, 1998.

- [50] E. Zhang, J. Laufer, and P. Beard, "Backward-mode multiwavelength photoacoustic scanner using a planar fabry-perot polymer film ultrasound sensor for high-resolution three-dimensional imaging of biological tissues," *Applied optics*, vol. 47, no. 4, pp. 561–577, 2008.
- [51] E. Z. Zhang, B. Povazay, J. Laufer, A. Alex, B. Hofer, B. Pedley, C. Glittenberg, B. Treeby, B. Cox, P. Beard, *et al.*, "Multimodal photoacoustic and optical coherence tomography scanner using an all optical detection scheme for 3d morphological skin imaging," *Biomedical optics express*, vol. 2, no. 8, pp. 2202–2215, 2011.
- [52] A. Rosenthal, M. Omar, H. Estrada, S. Kellnberger, D. Razansky, and V. Ntziachristos, "Embedded ultrasound sensor in a silicon-on-insulator photonic platform," *Applied Physics Letters*, vol. 104, no. 2, p. 021116, 2014.
- [53] T. Ling, S.-L. Chen, and L. J. Guo, "Fabrication and characterization of high q polymer micro-ring resonator and its application as a sensitive ultrasonic detector," *Optics express*, vol. 19, no. 2, pp. 861–869, 2011.
- [54] A. Maxwell, S.-W. Huang, T. Ling, J.-S. Kim, S. Ashkenazi, and L. Jay Guo, "Polymer microring resonators for high-frequency ultrasound detection and imaging," *Selected Topics in Quantum Electronics, IEEE Journal of*, vol. 14, no. 1, pp. 191–197, 2008.
- [55] H. Li, B. Dong, Z. Zhang, H. F. Zhang, and C. Sun, "A transparent broadband ultrasonic detector based on an optical micro-ring resonator for photoacoustic microscopy," *Scientific reports*, vol. 4, 2014.
- [56] A. Rosenthal, D. Razansky, and V. Ntziachristos, "High-sensitivity compact ultrasonic detector based on a pi-phase-shifted fiber bragg grating," *Optics letters*, vol. 36, no. 10, pp. 1833–1835, 2011.
- [57] A. Rosenthal, S. Kellnberger, D. Bozhko, A. Chekkoury, M. Omar, D. Razansky, and V. Ntziachristos, "Sensitive interferometric detection of ultrasound for minimally invasive clinical imaging applications," *Laser & Photonics Reviews*, vol. 8, no. 3, pp. 450–457, 2014.

- [58] A. Rosenthal, S. Kellnberger, M. Omar, D. Razansky, and V. Ntziachristos, "Wide-band optical detector of ultrasound for medical imaging applications," *JoVE (Journal of Visualized Experiments)*, no. 87, pp. e50847–e50847, 2014.
- [59] E. Khachatryan, S. Maswadi, D. Tsyboulski, E. Barnes, A. Oraevsky, K. Nash, and R. Glickman, "Optoacoustic microscopy using laser beam deflection technique," in *SPIE BiOS*, pp. 89432T–89432T, International Society for Optics and Photonics, 2014.
- [60] Z. Xie, S.-L. Chen, T. Ling, L. J. Guo, P. L. Carson, and X. Wang, "Pure optical photoacoustic microscopy," *Optics express*, vol. 19, no. 10, pp. 9027–9034, 2011.
- [61] A. E. Siegman, "Lasers," 1986.
- [62] M. Khan and G. Diebold, "The photoacoustic effect generated by an isotropic solid sphere," *Ultrasonics*, vol. 33, no. 4, pp. 265–269, 1995.
- [63] R. A. Kruger, D. R. Reinecke, and G. A. Kruger, "Thermoacoustic computed tomography—technical considerations," *Medical Physics*, vol. 26, no. 9, pp. 1832–1837, 1999.
- [64] D. Razansky, S. Kellnberger, and V. Ntziachristos, "Near-field radiofrequency thermoacoustic tomography with impulse excitation," *Medical physics*, vol. 37, no. 9, pp. 4602–4607, 2010.
- [65] S. Kellnberger, A. Hajiaboli, D. Razansky, and V. Ntziachristos, "Near-field thermoacoustic tomography of small animals," *Physics in medicine and biology*, vol. 56, no. 11, p. 3433, 2011.
- [66] C. Lou, S. Yang, Z. Ji, Q. Chen, and D. Xing, "Ultrashort microwave-induced thermoacoustic imaging: a breakthrough in excitation efficiency and spatial resolution," *Physical review letters*, vol. 109, no. 21, p. 218101, 2012.
- [67] C. Lou, S. Yang, Z. Ji, Q. Chen, and D. Xing, "Erratum: Ultrashort microwave-induced thermoacoustic imaging: A breakthrough in excitation efficiency and spatial resolu-

- tion [phys. rev. lett. 109, 218101 (2012)],” *Physical Review Letters*, vol. 112, no. 11, p. 119904, 2014.
- [68] S. Kellnberger, M. Omar, G. Sergiadis, and V. Ntziachristos, “Second harmonic acoustic responses induced in matter by quasi continuous radiofrequency fields,” *Applied Physics Letters*, vol. 103, no. 15, p. 153706, 2013.
- [69] J. Mankowski and M. Kristiansen, “A review of short pulse generator technology,” *Plasma Science, IEEE Transactions on*, vol. 28, no. 1, pp. 102–108, 2000.
- [70] D. Brown and D. Martin, “Subnanosecond high-voltage pulse generator,” *Review of scientific instruments*, vol. 58, no. 8, pp. 1523–1529, 1987.
- [71] X. L. Deán-Ben and D. Razansky, “Adding fifth dimension to optoacoustic imaging: volumetric time-resolved spectrally enriched tomography,” *Light: Science & Applications*, vol. 3, no. 1, p. e137, 2014.
- [72] A. A. Oraevsky, “3d optoacoustic tomography: From molecular targets in mouse models to functional imaging of breast cancer,” in *CLEO: Applications and Technology*, pp. AM1P–4, Optical Society of America, 2014.
- [73] A. Dima and V. Ntziachristos, “Non-invasive carotid imaging using optoacoustic tomography,” *Optics express*, vol. 20, no. 22, pp. 25044–25057, 2012.
- [74] H. Estrada, J. Turner, M. Kneipp, and D. Razansky, “Real-time optoacoustic brain microscopy with hybrid optical and acoustic resolution,” *Laser Physics Letters*, vol. 11, no. 4, p. 045601, 2014.
- [75] C. Vinegoni, C. Pitsouli, D. Razansky, N. Perrimon, and V. Ntziachristos, “In vivo imaging of drosophila melanogaster pupae with mesoscopic fluorescence tomography,” *Nature methods*, vol. 5, no. 1, p. 45, 2008.
- [76] A. Arranz, D. Dong, S. Zhu, M. Rudin, C. Tsatsanis, J. Tian, and J. Ripoll, “Helical optical projection tomography,” *Optics express*, vol. 21, no. 22, pp. 25912–25925, 2013.

- [77] B. J. Vakoc, R. M. Lanning, J. A. Tyrrell, T. P. Padera, L. A. Bartlett, T. Stylianopoulos, L. L. Munn, G. J. Tearney, D. Fukumura, R. K. Jain, *et al.*, “Three-dimensional microscopy of the tumor microenvironment in vivo using optical frequency domain imaging,” *Nature medicine*, vol. 15, no. 10, pp. 1219–1223, 2009.
- [78] J. Yao, C.-H. Huang, L. Wang, J.-M. Yang, L. Gao, K. I. Maslov, J. Zou, and L. V. Wang, “Wide-field fast-scanning photoacoustic microscopy based on a water-immersible mems scanning mirror,” *Journal of biomedical optics*, vol. 17, no. 8, pp. 0805051–0805053, 2012.
- [79] M. Khan and G. Diebold, “The photoacoustic effect generated by laser irradiation of an isotropic solid cylinder,” *Ultrasonics*, vol. 34, no. 1, pp. 19–24, 1996.
- [80] A. Den Dekker, A. Van den Bos, *et al.*, “Resolution: a survey,” *JOSA A*, vol. 14, no. 3, pp. 547–557, 1997.
- [81] L. Vionnet, J. Gateau, M. Schwarz, A. Buehler, V. Ermolayev, and V. Ntziachristos, “24mhz scanner for optoacoustic imaging of skin and burn,” 2013.
- [82] J. Laufer, P. Johnson, E. Zhang, B. Treeby, B. Cox, B. Pedley, and P. Beard, “In vivo preclinical photoacoustic imaging of tumor vasculature development and therapy,” *Journal of biomedical optics*, vol. 17, no. 5, pp. 0560161–0560168, 2012.
- [83] H. F. Zhang, K. Maslov, G. Stoica, and L. V. Wang, “Functional photoacoustic microscopy for high-resolution and noninvasive in vivo imaging,” *Nature biotechnology*, vol. 24, no. 7, pp. 848–851, 2006.
- [84] K. Maslov, G. Stoica, and L. V. Wang, “In vivo dark-field reflection-mode photoacoustic microscopy,” *Optics letters*, vol. 30, no. 6, pp. 625–627, 2005.
- [85] B. R. Masters and P. So, *Biomedical nonlinear optical microscopy*. Oxford University Press New York, 2008.

- [86] E. Tal, D. Oron, and Y. Silberberg, "Improved depth resolution in video-rate line-scanning multiphoton microscopy using temporal focusing," *Optics letters*, vol. 30, no. 13, pp. 1686–1688, 2005.
- [87] E. Papagiakoumou, V. de Sars, D. Oron, and V. Emiliani, "Patterned two-photon illumination by spatiotemporal shaping of ultrashort pulses," *Optics express*, vol. 16, no. 26, pp. 22039–22047, 2008.
- [88] C. R. Rose, Y. Kovalchuk, J. Eilers, and A. Konnerth, "Two-photon na^+ imaging in spines and fine dendrites of central neurons," *Pflügers Archiv*, vol. 439, no. 1-2, pp. 201–207, 1999.
- [89] P. Mahou, M. Zimmerley, K. Loulier, K. S. Matho, G. Labroille, X. Morin, W. Supatto, J. Livet, D. Débarre, and E. Beaupaire, "Multicolor two-photon tissue imaging by wavelength mixing," *Nature methods*, vol. 9, no. 8, pp. 815–818, 2012.
- [90] C. Zeng, S. Vangveravong, J. Xu, K. C. Chang, R. S. Hotchkiss, K. T. Wheeler, D. Shen, Z.-P. Zhuang, H. F. Kung, and R. H. Mach, "Subcellular localization of sigma-2 receptors in breast cancer cells using two-photon and confocal microscopy," *Cancer research*, vol. 67, no. 14, pp. 6708–6716, 2007.
- [91] L. Moreaux, O. Sandre, and J. Mertz, "Membrane imaging by second-harmonic generation microscopy," *JOSA B*, vol. 17, no. 10, pp. 1685–1694, 2000.
- [92] G. J. Tservelakis, D. Soliman, M. Omar, and V. Ntziachristos, "Hybrid multiphoton and optoacoustic microscope," *Optics letters*, vol. 39, no. 7, pp. 1819–1822, 2014.
- [93] G. J. Tservelakis, *Nonlinear optical procedures for the diagnostics and processing of biological samples by using ultra-short laser pulses*. PhD thesis, University of Crete, Heraklion, Greece, 2013.
- [94] J. Squier, M. Muller, G. Brakenhoff, and K. R. Wilson, "Third harmonic generation microscopy," *Optics Express*, vol. 3, no. 9, pp. 315–324, 1998.

- [95] Y. Barad, H. Eisenberg, M. Horowitz, and Y. Silberberg, "Nonlinear scanning laser microscopy by third harmonic generation," *Applied Physics Letters*, vol. 70, no. 8, pp. 922–924, 1997.
- [96] D. Débarre, W. Supatto, A.-M. Pena, A. Fabre, T. Tordjmann, L. Combettes, M.-C. Schanne-Klein, and E. Beaurepaire, "Imaging lipid bodies in cells and tissues using third-harmonic generation microscopy," *Nature methods*, vol. 3, no. 1, pp. 47–53, 2005.
- [97] J. Yao and L. V. Wang, "Photoacoustic microscopy," *Laser & photonics reviews*, vol. 7, no. 5, pp. 758–778, 2013.
- [98] K. Maslov, H. F. Zhang, S. Hu, and L. V. Wang, "Optical-resolution photoacoustic microscopy for *in vivo* imaging of single capillaries," *Optics letters*, vol. 33, no. 9, pp. 929–931, 2008.
- [99] S. Hu, K. Maslov, and L. V. Wang, "Second-generation optical-resolution photoacoustic microscopy with improved sensitivity and speed," *Optics letters*, vol. 36, no. 7, pp. 1134–1136, 2011.
- [100] C. Zhang, K. Maslov, S. Hu, R. Chen, Q. Zhou, K. K. Shung, and L. V. Wang, "Reflection-mode submicron-resolution *in vivo* photoacoustic microscopy," *Journal of biomedical optics*, vol. 17, no. 2, pp. 0205011–0205014, 2012.
- [101] J. Yao, C.-H. Huang, L. Wang, J.-M. Yang, L. Gao, K. I. Maslov, J. Zou, and L. V. Wang, "Wide-field fast-scanning photoacoustic microscopy based on a water-immersible mems scanning mirror," *Journal of biomedical optics*, vol. 17, no. 8, pp. 0805051–0805053, 2012.
- [102] J. Yao, *Multi-contrast Photoacoustic Microscopy*. PhD thesis, WASHINGTON UNIVERSITY IN ST. LOUIS, 2012.
- [103] R. L. Shelton, S. P. Mattison, and B. E. Applegate, "Molecular specificity in photoacoustic microscopy by time-resolved transient absorption," *Optics letters*, vol. 39, no. 11, pp. 3102–3105, 2014.

- [104] R. L. Shelton, S. P. Mattison, and B. E. Applegate, "Volumetric imaging of erythrocytes using label-free multiphoton photoacoustic microscopy," *Journal of biophotonics*, 2013.
- [105] D. Soliman, G. J. Tserevelakis, M. Omar, and V. Ntziachristos, "Combining microscopy with mesoscopy using optical and optoacoustic label-free modes," *Scientific reports*, vol. 5, 2015.
- [106] H.-C. A. Lin, A. Chekkoury, M. Omar, T. Schmitt-Manderbach, B. Koberstein-Schwarz, T. Mappes, H. López-Schier, D. Razansky, and V. Ntziachristos, "Selective plane illumination optical and optoacoustic microscopy for postembryonic imaging," *Laser & Photonics Reviews*, vol. 9, no. 5, pp. L29–L34, 2015.
- [107] P. J. Keller, "Imaging morphogenesis: technological advances and biological insights," *Science*, vol. 340, no. 6137, p. 1234168, 2013.
- [108] T. Schrödel, R. Prevedel, K. Aumayr, M. Zimmer, and A. Vaziri, "Brain-wide 3d imaging of neuronal activity in caenorhabditis elegans with sculpted light," *Nature methods*, vol. 10, no. 10, pp. 1013–1020, 2013.
- [109] D. Razansky, M. Distel, C. Vinegoni, R. Ma, N. Perrimon, R. W. Köster, and V. Ntziachristos, "Multispectral opto-acoustic tomography of deep-seated fluorescent proteins in vivo," *Nature Photonics*, vol. 3, no. 7, pp. 412–417, 2009.
- [110] L. Wolpert and C. Tickle, *Principles of development*. Oxford university press, 2011.
- [111] M. Omar, M. Schwarz, D. Soliman, P. Symvoulidis, and V. Ntziachristos, "Pushing the optical imaging limits of cancer with multi-frequency-band raster-scan optoacoustic mesoscopy (rsom)," *Neoplasia*, vol. 17, no. 2, pp. 208–214, 2015.
- [112] M. Omar, M. Schwarz, D. Soliman, P. Symvoulidis, and V. Ntziachristos, "Pushing the optical imaging limits of cancer with multi-frequency-band raster-scan optoacoustic mesoscopy (rsom)," *Neoplasia*, vol. 17, no. 2, pp. 208–214, 2015.

- [113] J. Aguirre, M. Schwarz, D. Soliman, A. Buehler, M. Omar, and V. Ntziachristos, "Broadband mesoscopic optoacoustic tomography reveals skin layers," *Optics letters*, vol. 39, no. 21, pp. 6297–6300, 2014.
- [114] M. Schwarz, M. Omar, A. Buehler, J. Aguirre, and V. Ntziachristos, "Implications of ultrasound frequency in optoacoustic mesoscopy of the skin," *Medical Imaging, IEEE Transactions on*, vol. 34, no. 2, pp. 672–677, 2015.